Noise assisted transport in artificial channels and neuronal membranes

Dissertation

zur Erlangung des akademischen Grades eines
Doktors der Naturwissenschaften
der Mathematisch–Naturwissenschaftlichen Fakultät
der Universität Augsburg vorgelegt

von
Yunyun Li
Lehrstuhl Für Theoretische Physik I
Universität Augsburg

Augsburg, im Mai 2011

Erstberichterstatter:	Prof. Dr. Peter Hänggi
Zweitberichterstatter:	Dr. Eric Lutz

Tag der mündlichen Prüfung: 1. Juli 2011

Contents

1 Summary

In the present thesis we report on the noise effects on transport: 1) noisy transport in confined geometries and 2) noise-assisted generation and propagation of electrical signals in neurons. Both analytic and computational techniques have been employed.

The first part is dedicated to the entropic transport which is about the movement of Brownian particles confined by geometric boundaries in two- or three-dimensional systems. In order to gain a physical insight, the so-called entropic transport has been studied analytically by means of the Fick-Jacobs equation that bases on the assumption of fast equilibrium in certain directions. The essential feature of the Fick-Jacobs equation is that the high dimensional system can be described by an effective one-dimensional system where the geometric confinement leads to an entropic potential contribution. Within this approach, the diffusion coefficient is spatially modified by the local geometric confinement. In order to get a better understanding of the accuracy as well as the limitations of the Fick-Jacobs equation, exact numerical simulations in higher dimensions have also been performed.

Within two important characteristics, namely the mean particle current $\langle \dot{x} \rangle$ and the effective diffusion coefficient D_{eff}, the entropic transport is quantitatively characterized. In presence of entropic potential barriers, we found that the resulting transport properties exhibit some novel features which are different and sometimes counter-intuitive to the conventional energetic transport. In particular, the mean current $\langle \dot{x} \rangle$ decreases with increasing temperature in the entropic transport, while the thermal activation enhances particle current over energetic potential barriers. Moreover, we found that the mean current $\langle \dot{x} \rangle$ and the effective diffusion coefficient D_{eff} depend very sensitively on the structure of the geometries of the channels, such as the maximum width of the channel and the ratio of the maximum and minimum width of the channel. Two scaling regimes have been intensively investigated: 1) the *constant-width-scaling* regime where the maximum width is fixed and 2) the *constant-ratio-scaling* regime where the ratio of the maximum and minimum width of the channel has been kept as constant. In both geometric scaling regimes, particle transport can be optimized by adjusting the structure parameters. This provides a convenient way to control the transport of Brownian particles by simple modulation of the channel geometries. Furthermore, the interplay between energetic and entropic potentials for the particle transport has been studied where an external energetic potential with the same periodicity as the geometric channel has been added. As the result of the competition between the energetic and entropic potentials, a resonance-like behavior has been found for the particle mobility as function of temperature.

The second part of this dissertation is devoted to the noise-assisted generation and propagation of electrical signals in neurons. One focus is on the role of the autapse phenomena, in which the dendrites form synapses transmitting information to

its own. We found that the stochastic fluctuations stemming from the intrinsic channel noise have to be taken into account. The autapse phenomena can be modeled by a stochastic Hodgkin-Huxley model with a Pyragas-like delayed feedback mechanism. The influence of the delayed stimulus has been systematically analyzed by investigating the Interspike Interval Histograms (ISIH) and the averaged interspike interval $\langle T \rangle$. It was known that the spontaneous spiking activities are maintained by noise and exhibit characteristic time scales. A new time scale is introduced into the system due to the presence of the delayed feedback. As a result, the bursting and multimodal interspike interval distributions are observed attributing to the interplay between the noise-induced intrinsic time scale and the delay-induced new time scale. In particular, synchronization phenomena between the delay- and noise-induced time scales have been detected for small noise levels and strong coupling strengths of the delayed feedback. A special frequency-locking behavior has also been discovered for the average interspike interval $\langle T \rangle$. The delay time scale and the intrinsic time scale determine how many spikes will be created and how many of them become subsequently locked during one delay epoch. It is interesting to notice that this frequency-locking behavior can be qualitatively explained by the well-known Kuramoto phase model with a built-in feedback.

As an extension of an earlier work [A. Ochab-Marcinek, G. Schmid, I. Goychuk, and P. Hänggi, PRE 79, 011904 (2009)], the noise-assisted propagation of electrical signals has been studied in myelinated neurons for the case of stronger channel noise intensities and suprathreshold couplings. We consider a multi-compartmental, stochastic Hodgin-Huxley model. Accordingly, each node of the Ranvier is modeled by a stochastic Hodgin-Huxley model and couples linearly to its nearest neighbors. Constant external current stimulus is applied only on the first node. As a measurement for the signal propagation reliability, we focus on the ratio between the number of the initiated spikes and the transmitted spikes (the transmission coefficient). At strong noise level, the terminal node spikes mostly spontaneously. To give a measurement of the causal relationship between the spiking at the initial and the terminal node, we consider the cross-correlation. It shows that the transmission reliability coefficient decreases with increasing channel noise level until the causal relationship is completely lost. In this limit, the spike propagation fails due to the intrinsic noise.

2 Introduction

For systems on nanoscales, noise stemming from different sources, such as thermal fluctuations and finite size effects, plays a major role and cannot be neglected. As a common feature, noise has been investigated in a large number of different fields, such as physics, chemistry, biology, finance, sociology and politics. Nearly every system is subjected to some kinds of noise.

Brownian dynamics is the archetype in the theoretical study of noise. In 1827, the English botanist R. Brown observed the very irregular motion displayed by a pollen particle immersed in a liquid. The motion of the pollen is the outcome of many unpredictable and sometimes unobservable events like collisions with the particles of the surrounding liquid. These events individually contribute a negligible contribution to the observation, but collectively lead to an observable effect. It is meaningless to look into the details of the individual events, but meaningful to study their statistical properties which determine the macroscopic behavior. Numerous theoretical efforts have been done regarding the dynamics of Brownian particles. Among these theoretical achievements, the most important one is the Fokker-Planck equation, from which the probability distribution function for a single particle can be determined. Since the probability distribution function encodes all the information for the dynamics, the macroscopic quantities, such as velocity and mobility, can be obtained by integration. As the Fokker-Planck equation is not limited to the situation where systems are close to the thermal equilibrium, it is a good tool to deal with the randomly fluctuating microscopic systems far from thermal equilibrium.

Since the 19th century, the study of noise has attracted long-standing attention and different noise effects have been spotted. In 1880s, people started to do research on the reaction-rate theory. It was recognized that the rate processes are characterized by rare events. The occurrence of the reaction took a long time scale to escape from a stable state. In 1889, Svante Arrhenius extensively discussed the various reaction-rate following the Van't Hoff's proposal in 1884 [1]. The reaction-rate k is a function of the inverse temperature T. The so-called Arrhenius equation has the form

$$k = A \exp\left[-E_a/(k_{\mathrm{B}}T)\right] , \tag{2.1}$$

where A is a prefactor, k_{B} is the Boltzmann constant and E_a denotes the threshold energy for activation which is called the activation energy. After a long period, it was realized that the escape from a stable state is actually a noise-assisted thermal activation. A quantitative escape rate was given by Hendrik Antonie Kramers in 1940's [2]. In the realm of noise effects, people have found many interesting phenomena, such as stochastic resonance [3], synchronization [4–6], phase locking [6, 7]. Remarkably, in most of these cases noise is constructive rather than it is destructive in respect to the order.

Since the discovery that noise can be rectified to achieve directed transport, scientists from different fields have shown great interest in noisy transport. In 1959, Richard Feynman challenged his audience to "make a thing very small which does what we want". This lecture which was presented to the American Physical Society at the California Institute of Technology, is considered to be the first lecture on nanotechnology. Since then, scientists from different fields began to look at this small thing, which is referred to as small engine. Normally, this kind of engine is in nanoscale. A series of theoretical works have been done and made a conclusion of the following prescriptions about designing efficient artificial nonodevices and Brownian motors [8]: (a) The system has to be driven away from equilibrium by additional deterministic or stochastic perturbation. (b) The spatial inversion symmetry should be broken, which can be achieved by different ways.

Over the past two decades, this nanoscale problem has attracted a lot of attention in the biophysical community. A typical protein consisting of only a few tens of thousands of atoms is in the size of a couple of nanometers. Therefore, the noise fluctuations play a non-negligible or even dominating role in biological systems. The energy is in the scale of thermal energy $k_{\mathrm{B}}T$. The effects of energy fluctuations in the movement of the protein engines have been demonstrated by Yanagida and co-workers [9]. They experimentally observed kinesin molecules climbing the cytoskeletal track in a juddering motion which is made up of random hesitations, jumps and even backward steps. In biological systems, the synchronization phenomena, such as the flashing of fireflies [10] and the synchronization between the respiratory and cardiac activity in human cardiorespiratory system [11], have been observed. Phase locking behavior has also been observed in paddlefish [12]. In the early 1990s, stochastic resonance was discovered in sensory neurons that were subjected to external noise [13, 14]. After a series of experiments and theoretical studies, Frank Moss's group [15, 16] reported that the mechanoreceptor hair cells located in the tailfans of crayfish, respond best to the stimuli between 1 and 25 Hz. Noise enhances the information transfer in crayfish mechanoreceptors by stochastic resonance. In other experiments, stochastic resonance has been established as well.

It turned out that noise plays a beneficial role in the transmission of signals and biological information processing. Moreover, the work about noise effects has been extended to the fundamental subcellular level: the ion channels. In artificial channels, Bezrukov and Vodyanoy had found that stochastic resonance does exist [17]. This provokes the challenge whether the stochastic resonance effect in biology is a collective behavior of finite assemblies of ion channels.

In our work, we will focus on two aspects of noisy transport which emerged very recently: 1) entropic transport within geometrical confinements and 2) signal generation and propagation in nerve cells.

Transport in artificial channels

Considering the transport within biological ion channels, we note that the geometrical confinements of the structure give a boundary limit which plays an important role in the diffusion process of ions. This diffusion process exhibits peculiar behaviors [18–21]. These particular properties can be used to control the transport of particles by modulating the structures of the geometrical confinement. Based on these, artificial channels can be designed and applied. In recent years, it has been of great interest to reveal the sequence and structure of the human genome by passing the DNA strand through a pore about couple nanometers in diameter [22–25]. Because each DNA base (A, G, C, T) is structurally and chemically different, it creates its own distinct electronic signature as the DNA molecules passes through a nanopore. Previous attempted experiments to sequence DNA using nanopores were not successful because the twisting and turning of DNA strand induced too much noise into the recorded signal [25]. An electric field is applied to drive the translocation of the DNA molecule in an electrolytic solution across the membrane through the nanopore [26]. However, the properties of the confined transport and the effect of the electric field in the confinement were not quantitatively studied. It is highly desirable to efficiently calculate the noisy transport in confined geometries. The geometrical confinement makes the transport problem difficult to solve. The so-called Fick-Jacobs equation based on the fast equilibrium assumption can reduce the complexity of the problem. The essential dynamics is described by a one-dimensional kinetic equation with an effective potential which includes the entropic contribution arising from the geometric confinement. This approximation method makes our aim, i.e. the quantitative study of transport in confined geometries possible to realize.

Transport in neuronal systems

Secondly, we focus on the noise effect in biological systems, in particular signal generation and propagation in nervous systems. Animals including humans learn, think, deliver motion instructions and maintain conscious between themselves and outside world through their nervous systems. The basic unit of the nervous system is the so-called neuron (nerve cell), which is the most important and interesting cell in the body. Neurons regulate all aspects of the bodily functions such as neurons storing, computing, integrating and transmitting information. The human brain as the control center contains about 10^{12} neurons. Each neuron forms as many as thousands of connections with other neurons. These neurons sense features of both external and internal environments and transmit this information to brain.

The structures and functions of individual nerve cell have been studied in great details. The function of a neuron is to communicate and process information, which is conveyed by electric signals and chemical signals. Generally, electric signals process and conduct information within a cell, while chemical signals transmit information between cells [27]. These two types of signals can be converted into each other. A typical neuron is constituted of three principal parts: *dendrites*, *soma* (cell body) and *axon*. Fig. 2.1 depicts the structure of a typical neuron. Dendrites are the input stage of the neuron. They are responsible for receiving signals from other neurons and then convert them into electric impulses and transmit them in the direction of the soma (cell body). The electric impulses which are series of sudden changes in the voltages are the so-called *action potentials* [27]. The soma contains the necessary cellular machinery, for example nucleus and mitochondria. The axon is the

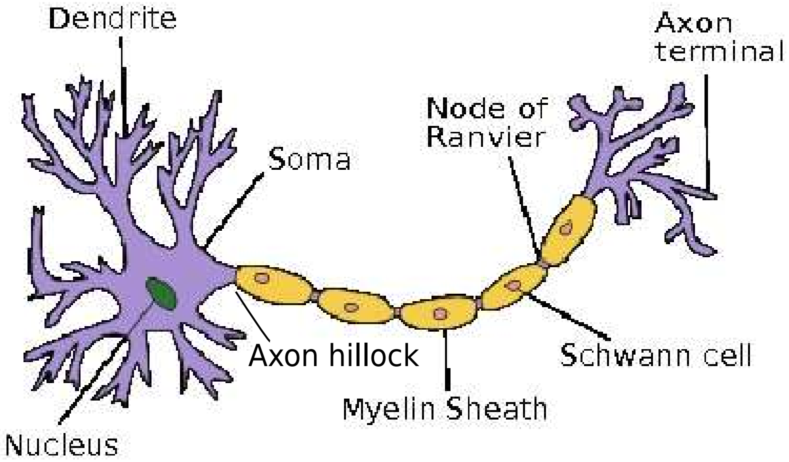

Figure 2.1: Schematic structure of a typical neuron. The important concepts are labeled. [Adapted from http://psychology.wikia.com/wiki/Neurons]

output stage of the neuron. It is specialized for the conduction of action potentials away from the soma towards the axon terminal. At the end of axon, neuronal cell bodies can also form *synapses* that are cellular junctions used for the transmission of electrical signals.

In order to gain a quantitative understanding of nerve excitations, numerous theoretical works have been done. The most successful quantitative model is the one proposed by Hodgkin and Huxley in 1952 [28]. The so-called Hodgkin-Huxley model is described by a four-dimensional deterministic set of ordinary differential equations. Later on, the underlying mechanism of the action potential generation is found to be the opening and closing of individual ion channels. These ion channels which switch stochastically rather than deterministically are embedded in the membranes. The membrane transport refers to the collective mechanisms that regulate the passage of ions and small molecules through biological membranes. Hence, the intrinsic noise stemming from the random opening and closing in each ion channel was taken into account. The noise and fluctuations were firstly theoretically studied by Lecar and Nossal in 1971 [29, 30].

The aim of biological systems is to uncover the fundamental operations of the cell in an effect to predict the response to specific stimuli and genetic variations. In 1972 Van der Loos and Glaser have found an axon that makes a synaptic connection onto its own dendritic tree and called this *autapse* (c.f. Fig. 2.2) [31]. Based on many experimental observations, it has been found that autapses are existing more frequently on two subclasses of cortical inhibitory interneurons and rare on pyramidal cells. Therefore, they are not just as the unfortunate consequence of an imprecise developmental, but also have a functional role [32]. However, what functional role they play and their mechanisms in the neuron systems are still open to debate.

Furthermore, the fast propagation of action potentials along the axons is fundamentally important. Axons come in two flavors: One of them called *myelin* is partially covered by layers of the lipid and the other one is called *unmyelin*. In the myelinated axons, the conduction does not proceed continuously along the axon, but

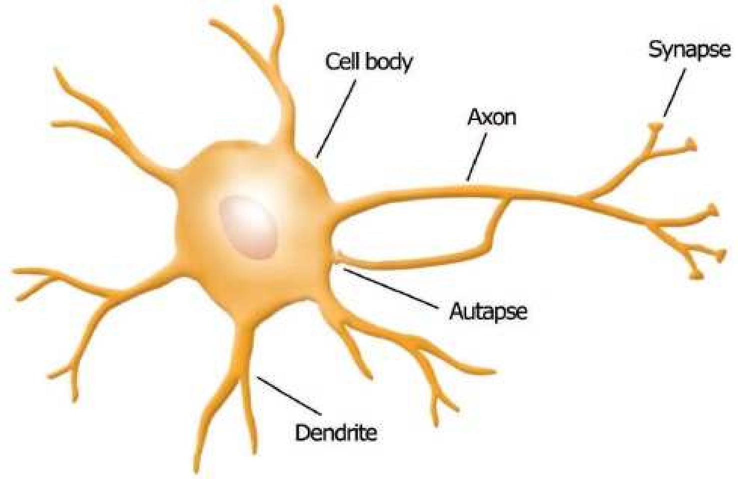

Figure 2.2: Schematic diagram of a basket cell with autapse feedback. [Adapted from C. S. Herrmann et al., Int. J. Bifurcat. Chaos, **14**(2), 623-633 (2004)]

jumps from one node to other, (c.f. Fig. 2.1). This results in a faster propagation speed in myelinated axons than that in unmyelinated axons. Generally, the action potentials move very fast (at speeds up to several hundreds of m/s) with little temporal dispersion [27, 32]. In humans, the axons may be more than one meter long. This takes a few milliseconds for an action potential to move along the axons. The action potential is generated at the *axon hillock* where is the junction of the axon and cell body (c.f. Fig. 2.1). Then it is actively conducted down the axon into the axon terminals. We are interested in the fast propagation mechanisms in the myelinated axons, particularly the influence of intrinsic noise on the propagation of action potentials.

Outline

The present thesis is organized as follows: Chapter 3 is devoted to the noise assisted transport in confined geometries. Before considering the entropic transport (confined geometries), we give a brief introduction of the energetic transport without any geometrical constrains in Section 3.1. The mathematical framework and the main properties of the transport in a purely energetic potential are presented. At the same time, we give a flavor of the concepts and characteristics of transport. In Section 3.2, we investigate the transport characteristics of Brownian particles in geometrically confined systems. After presenting some nanoscaled devices, we present the main results of our work: Diffusive transport of Brownian particle in a narrow channel with periodically varying cross-sections is studied. The numerical findings of the transport characteristics are discussed. Furthermore, we study the entropic transport in the situation that the Brownian particle is subjected to an additional energetic potential exhibiting the same periodicity as the channels. The competition between energetic and entropic contributions to the transport is analyzed. The conclusion is presented in Section 3.3.

In Chapter 4, we study the noise-assisted generation and propagation of signals in neurons. An introduction of the cell signaling on the neurophysiology level is presented in Section 4.1. In particular, the most important landmark, i.e. the Hodgkin-Huxley model in the study of neuron systems is discussed in detail. Additionally, the channel noise is discussed and a stochastic Hodgkin-Huxley model is obtained. In Section 4.2, we present our work on the autapse phenomenon. A stochastic Hodgkin-Huxley model containing a Pyragas-like delayed feedback current is applied to model this phenomenon. With numerical simulations, the main results are addressed. In Section 4.3, we study the propagation of action potentials along myelinated axons which is studied within a stochastic Hodgkin-Huxley model. The nodes of Ranvier in myelinated axon are bi-linearly coupled and constant external current stimulating only on the first node. Based on a multi-compartmental stochastic Hodgkin-Huxley equation, the simulation results are presented. In Section 4.4, we give a conclusion.

Chapter 5 contains the potential directions of our future research. Two appendixes A.1 and A.2 are included at the end.

3 Entropic transport in confined geometries

In many transport phenomena, such as those taking place in biological cells, ion channels, nanoporous, zeolites, and microfluidic devices etched with grooves and chambers, Brownian particles usually undergo geometrically constrained movements instead of the free diffusion in the host of liquid phase [18–21, 33–41]. The confinement arising from the presence of boundaries can in principle be modeled by means of an effective entropic potential [42, 43]. It regulates the transport, promoting or hampering the transfer of mass and energy to certain regions, and generates important consequences with peculiar properties [18–21]. This kind of diffusion processes which is the so-called entropic transport, has widespread implications in the technology development for both natural and artificial microporous media [33, 35, 44].

The purpose of this chapter is to investigate the nontrivial properties of the entropic transport. To make a comparison, we start from a brief introduction for the conventional energetic transport which occurs in the systems without geometrical constraints. In Section 3.1, the main transport properties for energetic transport will be shortly discussed for purely energetic systems. In Section 3.2, we study the interesting problem of entropic transport in confined geometries. To unravel the unconventional properties of the entropic transport in 2D or 3D, we use the method of numerical simulations as well as an analytic approach based on the Fick-Jacobs approximation. The results have been published in Ref. [43] and [45]. In Section 3.3, we give the main conclusions for the energetic and entropic transport.

3.1 Energetic transport: thermal-activated transport over energetic barriers

In order to gain a better understanding of the entropic transport with constrained geometries, we first discuss the case of energetic transport in which the Brownian particle moves in a purely energetic potential. Nearly every system is subjected to some kinds of internal or external fluctuations, which are referred to as noise. Due to these fluctuations, it is meaningless to consider the exact positions of a Brownian particle. Instead, it is more convenient to define a probability distribution function which describes the probability of finding such particles in a given region at some given time. This probability distribution function can be determined by the corresponding Fokker-Planck equation which is well studied and widely used in various areas of natural sciences [46].

An interesting and practical problem involves a dynamic system which possesses in some free energy landscapes separated by energy barriers [46, 47]. The free energy landscapes can be mapped with a function of an order parameter or a reaction coordinate which represents a metastable state. These barriers play a very important role for the dynamics of the system. It turns out that the problem of particles crossing barriers underpins many scientific disciplines. Therefore, the quantitative calculations of the escape rate from metastable states have received many contributions from fields as diverse as chemical kinetics, homogeneous nucleation, and diffusion in solids, to name but a few in the 19th century. Based on earlier studies, Hendrik Antonie Kramers (1894-1952) pictured the escape process as a stochastic force driven Brownian motion and obtained the escape rate from the Fokker-Planck equation [2, 48].

Generally, energetic transport occurred in systems with periodic potentials which is modeled by the corresponding Fokker-Planck equation for Brownian motion in periodic energetic potentials. The time-dependent probability distribution for the relevant degrees of freedom can be obtained from the Fokker-Planck equation and it encodes all the information needed for calculating other transport quantities for a stochastic system. With this knowledge, the transport properties in the purely energetic system can be quantitatively measured and analyzed.

3.1.1 Diffusion processes in energetic systems

The study of particles diffusing freely in the host medium has a long history. As early as 1827, Robert Brown had observed this motion which is known as the Brownian motion nowadays. Later on, the dynamics of Brownian motion and the mathematics behind it were studied [49–52]. For example, in 1905 Albert Einstein proposed his theory of Brownian motion based on the molecular-kinetic theory and brought this problem to the attention of physicists [49, 53]. Around the same time, many other theoretical proposals were made independently by such as William Sutherland (1904), Marian Smoluchowski (1906) and Paul Langevin (1908) who employed different approaches [50–52]. All of them made the same conclusion: Normally the mean square displacement of Brownian particles subjected to random collisions is proportional to the time and the free diffusion coefficient which can be determined by the thermal noise arising from the interaction between the Brownian particles and their environment. In these theoretical descriptions, the particles diffuse freely without any geometrical constrains. The motion of the Brownian particles is subject to the thermal fluctuations.

Free diffusion

In 1905 Albert Einstein had noted that the motion of Brownian particles (c.f. Fig. 3.1) is caused by the random forces, i.e. fluctuations. From this observation, he concluded that the mean square displacement is proportional to the time t and the diffusion constant D_0. It can be written as

$$\langle (x(t) - x_0)^2 \rangle = 2D_0 t, \tag{3.1}$$

where $x(t)$ and x_0 are the positions of the Brownian particle at time t and $t = 0$, respectively. The diffusion constant D_0 which was obtained by statistical mechanics

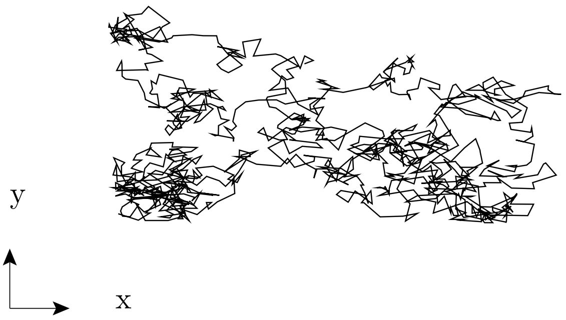

Figure 3.1: An exemplary trajectory of a Brownian particle in 2D. The free diffusion is caused by the thermal fluctuation (noise).

have the following form:

$$D_0 = \frac{k_\mathrm{B}T}{\eta}. \tag{3.2}$$

Here, k_B denotes the Boltzmann constant, T is the temperature, and η is the friction coefficient. Physically, this friction arises from the constantly collisions between the Brownian particle and the molecules of the liquid environment. Eq. (3.2) is known as the Sutherland-Einstein relation that represents a special form of the more general fluctuation-dissipation theorem. This is a general result of statistical thermodynamics.

We start with a simple example: A Brownian particle within a homogeneous temperature T under the influence of a bias. For the Brownian particle, the thermal fluctuations due to the coupling of the particles with the environment can be expressed as a stochastic force $\xi(t)$ which is called Langevin force. The dynamics of this Brownian particle can be governed by Newton's equation of motion [54], written as,

$$m\ddot{x}(t) + \eta\dot{x}(t) = F + \sqrt{\eta k_\mathrm{B}T}\,\xi(t), \tag{3.3}$$

where $\ddot{x}(t)$ and $\dot{x}(t)$ are the second and first order time derivative of the position $x(t)$, respectively, F denotes the bias which is a constant force, and $\xi(t)$ is a Gaussian white noise with zero mean,

$$\langle\xi(t)\rangle = 0, \tag{3.4}$$

and correlation function,

$$\langle\xi(t)\xi(t')\rangle = 2\delta(t - t'). \tag{3.5}$$

When the inertia of the particles, i.e. the first term on the left side in Eq. (3.3), is very small compared to the friction force, it can be neglected [54]. This case is referred to as overdamped Brownian motion which is often encountered in extremely small systems.

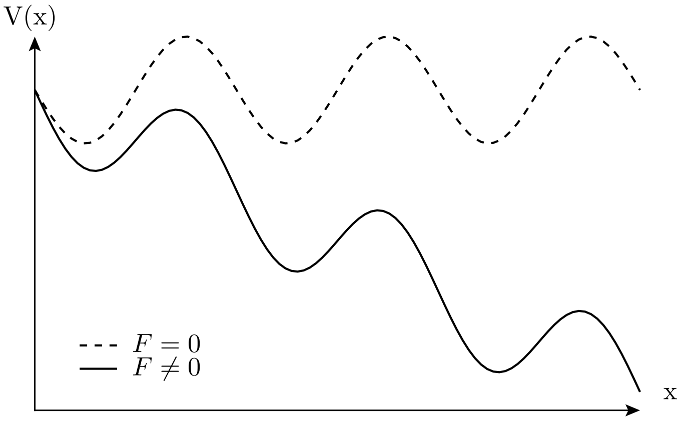

Figure 3.2: Effective potential $V(x) = U(x) - Fx$ in the presence and absence of an applied bias.

Diffusion process in periodic potentials

Thermal diffusion in a periodic potential is subject to several fields of science: physics, chemical physics, communication theory [55–58]. The periodic potential landscape appeared in many processes, such as Josephson tunneling junctions [59–61], rotation of dipoles in a constant electric field [62, 63], pendulum, diffusion of atoms and molecules on crystal surfaces [64], and biophysical process [65]. Here, we study the process of a Brownian particle in periodic potentials. Restricting our considerations to one-dimensional problems, we can describe the dynamics for the 1D overdamped Brownian motion with the following Langevin equation,

$$\eta \dot{x}(t) = -V'(x) + \sqrt{\eta k_{\mathrm{B}} T}\, \xi(t)\,, \tag{3.6}$$

where $V(x) = U(x) - Fx$ is the effective potential, c.f. Fig. 3.2, with the bias F and periodic potential function $U(x)$ with periodicity L, i.e. $U(x+L) = U(x)$. The prime over the effective potential in Eq. (3.6) means the derivation with respect to x. Fig. 3.2 shows a sketch of a one-dimensional effective periodic potential in the presence and absence of an external bias F. The potential is spatially symmetric when $F = 0$, whereas this spatial symmetry breaks down in the presence of F.

The corresponding Fokker-Planck equation for the time evolution of the probability distribution is given by [46]:

$$\frac{\partial P(x,t)}{\partial t} = \frac{1}{\eta} \frac{\partial}{\partial x} \left[V'(x) + k_{\mathrm{B}} T \frac{\partial}{\partial x} \right] P(x,t)\,, \tag{3.7}$$

where $P(x,t)$ is the probability distribution to find the particle in the interval $(x\ ,\ x + \mathrm{d}x)$ at time t . It turns out that the Fokker-Planck equation is a convenient tool to deal with the fluctuations which stem from many tiny disturbances. Each of those fluctuations changes the variables in an unpredictable but small way [46]. From Eq. (3.7) the probability distribution of the Brownian particle can be obtained.

Dimensionless units

For the sake of simplicity quantities, we can express the Langevin equation Eq. (3.6) in a dimensionless form by rescaling lengths in units of the period L, force in units of $F_\mathrm{R} = k_\mathrm{B}T_\mathrm{R}/L$, the energy in units of $k_\mathrm{B}T_\mathrm{R}$, and time in units of the characteristic time scale $\tau = \eta L^2/k_\mathrm{B}T_\mathrm{R}$ which is the corresponding characteristic diffusion time at an arbitrary but irrelevant reference temperature T_R to overcome a distance of L [18, 66]. Then the dimensionless form of the Langevin equation reads,

$$\frac{\mathrm{d}\tilde{x}(\tilde{t})}{\mathrm{d}\tilde{t}} = -\frac{\partial}{\partial \tilde{x}}\tilde{V}(\tilde{x}) + \sqrt{\tilde{D_0}}\,\xi(\tilde{t}), \tag{3.8}$$

where we used the following notations,

$\tilde{x} = x/L$,

$\tilde{t} = t/\tau$,

$\tilde{D_0} = D_0/(k_\mathrm{B}T_\mathrm{R}/\eta) = \frac{\eta D_0}{k_\mathrm{B}T_\mathrm{R}}$,

$\tilde{V}(\tilde{x}) = V(\tilde{x})/k_\mathrm{B}T_\mathrm{R}$, including:

$\tilde{U}(\tilde{x}) = U(\tilde{x})/k_\mathrm{B}T_\mathrm{R}$ and $\tilde{f} = F/F_\mathrm{R} = \frac{FL}{k_\mathrm{B}T_\mathrm{R}}$.

For convenience, we omit the tilde symbols above the coordinates in the following sections. So that, the dimensionless Langevin equation reads,

$$\dot{x}(t) = -\frac{\partial}{\partial x}U(x) + f + \sqrt{D_0}\,\xi(t)\,. \tag{3.9}$$

Kramers' rate

One application of the Fokker-Planck equation is to describe the escape process. This has been firstly studied for chemical reactions in condensed phase by Kramers in 1940s' [2]. He proposed a simple one dimensional model which incorporates the essential physical ideas of activated rate theory into a comprehensive mathematical framework. It turns out that this rate theory plays a central role in both theoretical and numerical groundwork to understand the principles of thermal reaction calculations [48, 67]. The determination of the escape rate is a problem of nonlinear sciences arising in many areas and branches, such as chemical kinetics [2, 68, 69], diffusion in solids [70, 71], homogeneous nucleation [72, 73], electronic transport [74–76]. Here, we give a brief overview of this model and its important results, c.f. the Kramers' rate and the mean first-passage time (MFPT).

Kramers' model is about a Brownian particle escaping out of a potential well over a potential barrier (Fig. 3.3). The model focuses on the escape process when the barrier height ΔU is much larger than the thermal energy which is just D_0 in

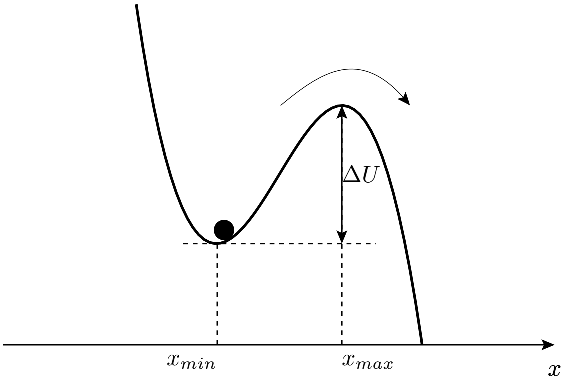

Figure 3.3: A cubic potential function $U(x)$ used for the Kramers' model. Particles are injected at x_{min} and immediately removed when they cross the top point x_{max}. ΔU is the corresponding activation energy.

our scaling, i.e. $\Delta U/D_0 \gg 1$. For a cubic potential $U(x)$ with a large barrier height ΔU plotted in Fig. 3.3, the escape rate r_{K} of an overdamped Brownian particle is given by the Kramers rate [2]:

$$r_{\mathrm{K}}(D_0) = \frac{\sqrt{U''(x_{min})|U''(x_{max})|}}{2\pi}\, e^{-\Delta U/D_0}, \tag{3.10}$$

where $U''(x)$ is second derivative of the potential function at position x. x_{min} and x_{max} indicate the positions of the minimum and maximum of the potential function, respectively, and the barrier height ΔU denotes the activation energy.

Another important characteristic quantity is the mean first-passage time (MFPT) of the escape process. It is defined as the average time elapsed until the process starting from the injection point x_{min} (c.f. Appendix A.1). It was shown that, the mean first-passage time (MFPT) for an escape process from a cubic domain is the inverse of the Kramers' rate [77].

$$T = \frac{1}{r_{\mathrm{K}}(D_0)} = \frac{2\pi}{\sqrt{U''(x_{min})|U''(x_{max})|}}\, e^{\Delta U/D_0}. \tag{3.11}$$

3.1.2 Transport characteristics

To investigate the transport of Brownian particles, we are interested in the quantities as the average current $\langle \dot{x} \rangle$, the mobility $\mu = \langle \dot{x} \rangle / f$, and the effective diffusion coefficient D_{eff}. We will discuss them in details, basing on a 1D model described by Eq. (3.9).

For one-dimensional periodic potential, an analytical expression for the average current $\langle \dot{x} \rangle$ can be determined by generalizing the mean first passage time approach [78–80]. Accordingly, the average current $\langle \dot{x} \rangle$ is given by [42, 79, 80]

$$\langle \dot{x} \rangle = \frac{1}{\langle T \rangle} = \frac{1 - e^{-\beta f}}{\displaystyle\int_{x_0}^{x_0+1} \mathrm{d}x I_{\pm}(x)}, \tag{3.12}$$

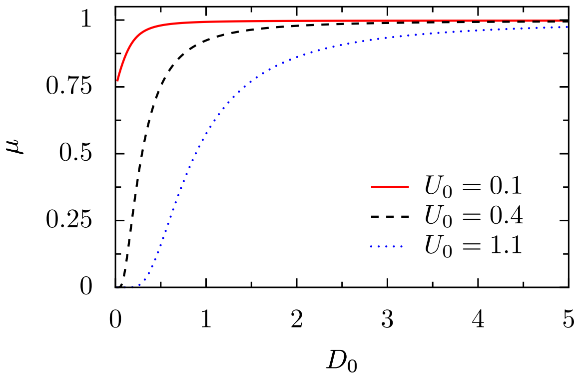

Figure 3.4: The dependence of the mobility μ on the noise strength D_0 for different amplitudes U_0 of a periodic potential with $U(x) = U_0 \sin(2\pi x)$ while the force is fixed at 1.

here $\langle T \rangle$ denotes the average first passage time T of the particle crossing a unit cell of the potential energy function in x direction. $\beta = 1/D_0$, and $I_\pm(x)$ is the abbreviation of $I_+(x)$ and $I_-(x)$. They are given by,

$$I_+(x) = \frac{1}{D_0} e^{\beta V(x)} \int_{x-1}^{x} \mathrm{d}y \, e^{-\beta V(y)} \,, \tag{3.13}$$

$$I_-(x) = \frac{1}{D_0} e^{-\beta V(x)} \int_{x}^{x+1} \mathrm{d}y \, e^{\beta V(y)} \,. \tag{3.14}$$

The thermal fluctuation results in a spatial dispersion of the particle around its average position $\langle x(t) \rangle$. The corresponding normal diffusion coefficient is given by [79, 80]

$$D_{\text{eff}} = \lim_{t \to \infty} \frac{\langle x^2(t) \rangle - \langle x(t) \rangle^2}{2t} \,. \tag{3.15}$$

It can be computed analytically as [42]

$$D_{\text{eff}} = \frac{\langle T^2 \rangle - \langle T \rangle^2}{2 \langle T \rangle^3} \,. \tag{3.16}$$

Thus, the explicit expression for the effective diffusion coefficient can be obtained [42, 79, 80]

$$D_{\text{eff}} = D_0 \frac{\displaystyle\int_{x_0}^{x_0+1} \mathrm{d}x I_\pm(x) I_+(x) I_-(x)}{\left[\displaystyle\int_{x_0}^{x_0+1} \mathrm{d}x I_\pm(x) \right]^3} \,. \tag{3.17}$$

For free diffusion, the average current $\langle \dot{x} \rangle$ can easily be obtained from the Langevin equation Eq. (3.6) and Eq. (3.4), i.e. $\langle \dot{x} \rangle = 0$. The effective diffusion coefficient tends to the Einstein relation Eq. (3.2).

Other characteristics, such as the nonlinear mobility μ, can be derived from these two quantities: the average current $\langle \dot{x} \rangle$ and the effective diffusion coefficient D_{eff}. For example, the mobility which is defined by $\mu = \langle \dot{x} \rangle / f$.

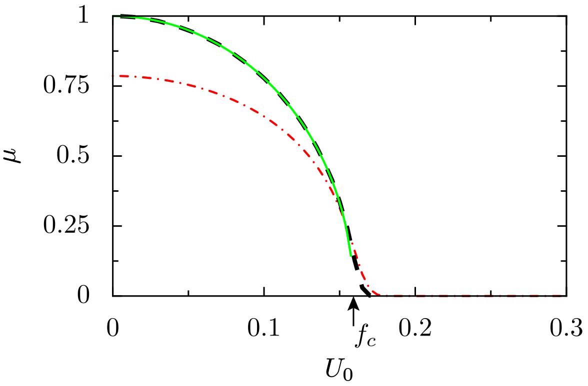

Figure 3.5: The dependence of the mobility on the amplitude U_0 of a periodic potential at fixed force 1 in the deterministic limit. The solid green line is the result from Eq. (3.18). The dotted red line is generated by Eq. (3.12), and dashed black line is obtained from the original Langevin equation Eq. (3.9) at very low noise strength $D_0 = 0.002$. The critical force $f_c = 0.159$ is marked in the figure.

Now, we consider a particle diffusing in periodic potential system, i.e. $U(x) = U_0 \sin(2\pi x)$. Based on Eq. (3.12), the mobility is plotted as a function of the strength of the thermal noise at different amplitudes U_0 with fixed force $f = 1$ in Fig. 3.4. As introduced for the Kramers' escape rate, temperature facilitates the particle to overcome the barrier, thus enhancing the average current. Therefore, the mobility increases monotonically as the noise strength increases, shown in Fig. 3.4.

The mobility μ for the deterministic limit, i.e. $D_0 \to 0$, is given as [46]

$$\lim_{D_0 \to 0} \mu = \begin{cases} \sqrt{1 - \left(\frac{2\pi U_0}{f}\right)^2} & U_0 < \frac{f}{2\pi} = f_c \\ 0 & U_0 \geq f_c. \end{cases} \tag{3.18}$$

Here, f_c is referred to as critical force. When the amplitude U_0 is larger than the critical value, the particle can not escape from the bottom of the potential well, and there is no average current, c.f. $\mu = 0$. We compare the mobility obtained from different methods in the deterministic limit in Fig. 3.5. The simulation methods are presented in Appendix A.1 and Appendix A.2.

3.2 Entropic transport: Particle transports in nano-scaled channels or pores

Instead of diffusing freely, Brownian particles frequently undergo some geometrical restrictions. This constrained motion is ubiquitous in ion channels, biological cells, nanopores, zeolites and processes occurring at sub-cellular [18–21,33–41]. This confined diffusion process exhibits peculiar properties, which are different from what is known for energetic systems, c.f. Section 3.1. Since the properties sensitively

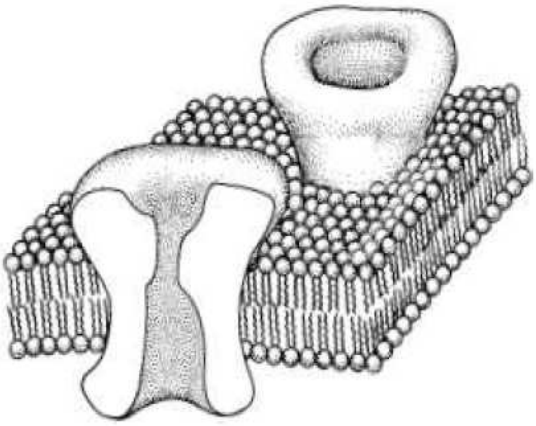

Figure 3.6: Schematic diagram of the cell membrane containing biological nanopores (ion channels). [Adapted from B. Hille, Ion Channels of Excitable Membranes (Sinauer, Sunderland, 2001).]

depend on the shape of the confined structure, the geometrical confinement plays a fundamental role in many transport phenomena. Therefore, it can be used to regulate or control the diffusion processes such as catalysis, osmosis and particle separation [33–36,39,40], noise-induced transport in periodic potential landscapes that lack of reflection symmetry (ratchet systems) or ratchet transport mechanisms that are based on asymmetric geometries, and termed 'entropic' ratchet devices [8,43,81–83].

In the following, we give a brief overview over a few of these processes and nano-scaled devices which are widely used as the geometrical confinements.

Nanopores

A nanopore is a small hole in an electrically insulating membrane. Normally with the internal diameter in order of several nanometers, it is a highly confined structure. Charged molecules or ions passing through it, exhibits different ionic current. The current changes due to the electrostatic interaction between the ions through the nanopore and the surface charge at the small opening (bottleneck) of the pore [23, 24, 35, 41, 84–86]. The bottleneck which plays an important role in the transport of charged molecules and ions induces the ionic current exhibiting peculiar behavior. Nanopores exist in nature and can be fabricated artificially too. Natural nanopores are called biological nanopores (ion channels), shown in Fig. 3.6, and the artificial ones are called synthetic nanopores [23, 24, 84].

In living cells, there are certain transmembranal proteins acting as biological nanopores (ion channels). They help establish and control the voltage gradient across the plasma membrane of cells by allowing the flow of ions due to their electrochemical gradient. The structure and basic functions will be discussed in Chapter 4. Note that, here the geometrical confinement of the channels can not be neglected in the transport processes of ions, such as macromolecules and polymers cross membranes [87–89]. The uneven shape of the channels regulates the transport of ions

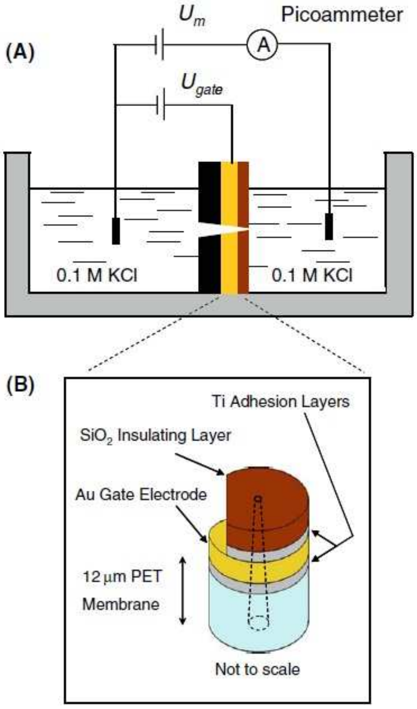

Figure 3.7: (A) Schematic diagram of the experimental setup to study single conical nanopores with a gate. (B) Scheme of a conical nanopore with metal and silicon dioxide layers. [Adapted from E. B. Kalman et al., Anal Bioanal. Chem. **394**, 413-419 (2009).]

which exhibits peculiar properties. This results have implications in processes, such as protein binding kinetics [90], drug release [91], protein folding [92], the motion of polymers subjected to rigid constrains [93], and polymer crystallization [94].

As the nanopores are important, artificial nanopores are fabricated. Since it is firstly created in 1995, there is a great interest to design and develop artificial nanopores (synthetic nanopores) because of their potential applications as biomimetic systems. With newest technology, these synthetic nanopores can be made upon choice, allowing to controlling the diameter and the shape of the nanoporous structure [35, 85, 95]. Therefore, the characteristic behavior of ionic currents and the flow of the macromolecules can be controlled. The nanopores are available to characterize the transport properties of ionic species, such as K^+, Na^+, Cl^- [35, 41] and of macro molecules, like DNA or RNA [23, 24, 26, 86, 95].

Diffusing through nanopores, molecules of intermediate size can get temporarily trapped which can extend to maximize their conformational entropy [96]. Asher and his co-workers have found experimental evidence to verify that this *entropic trapping* can increase the dependence of the diffusion rate on molecular size [34]. Their approach may lead to the design of improved separation media based on entropic trapping. Recently, experiments have been done to control the ionic transport through nanopores by Zuzanna Siwy's group [97]. A schematic diagram of their experimental setup to measure the ionic current is depicted in Fig. 3.7. It shows that the ionic transport can be controlled by the potential of the gating conical

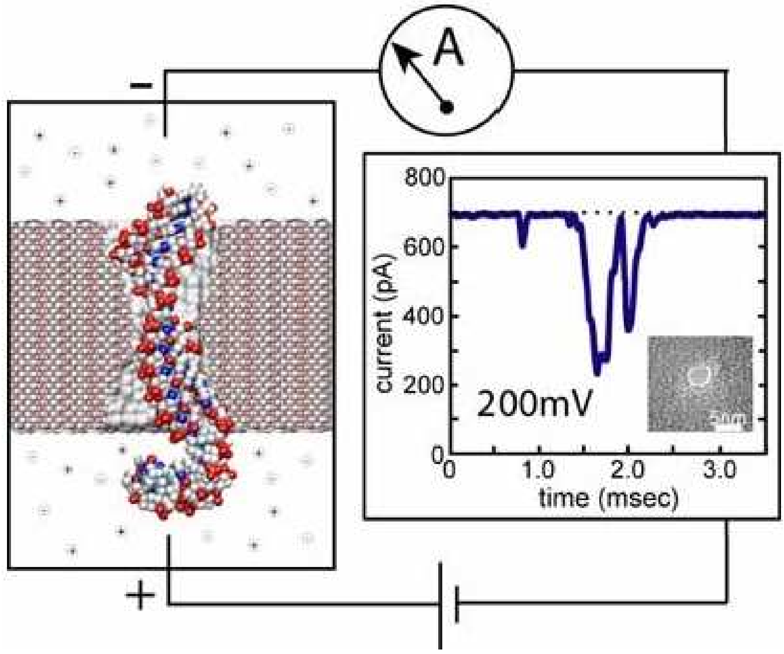

Figure 3.8: Experimental setup for electric detection of individual DNA molecules passing through a synthetic nanopore (left) and the corresponding current (right). The transition of DNA through the nanopore is driven by the electric field between two electrodes. A transient blockade of the ionic current is measured by the amplifier. [Adapted from Aksimentiev et al., Biophys. J. **87**, 2086-2097 (2004).]

nanopores. This offers a possibility to design ionic logic devices and ionic amplifiers. It can be applied for pumping ions across the membrane.

The artificial nanopores offer many potential applications. The development of new devices on the basis of nanopores gives challenges both experimentally and theoretically. It has been of great interest to reveal the sequence and structure of DNA and RNA molecules by passing them through nanopores [22, 43]. The nanopore is made from silicon nitride, a material that is easy to work with and commonly used in nanostructures surrounded by two pairs of tiny gold electrodes. The electrodes would record the electrical current perpendicular to the DNA strand as it passed through the nanopore [25]. Because each DNA base has different structure and chemical properties, it exhibits its own distinct electronic signal when the DNA strand passes through the charged nanopore. The schematic experimental setup is shown in Fig. 3.8 [23, 24]. The electric field can drive single-stranded DNA or RNA molecules through the nanopore in a thin, synthetic membrane. As the diameter of the nanopore can accommodate only a single strand of DNA or RNA, each polymer transverses the membrane as an extended chain. This chain blocks the nanopore partially. The so-called ionic current blockade is recorded by the amplifier. The blockade currents of single-stranded DNA and RNA electro-phoretically driven through a transmembrane nanopore were firstly measured by Kasianowicz etc [98]. They used the method to measure the polynucleotide length. As the developments of this technique, it has demonstrated that single-nucleotide resolution for DNA

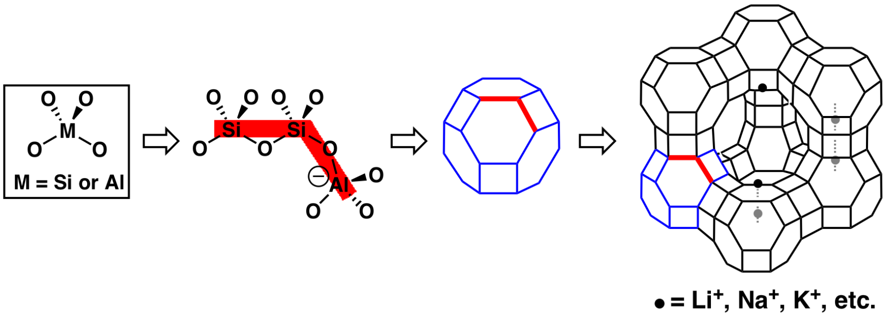

Figure 3.9: The formation and framework structure of zeolite. [Adapted from http://ochem.jsd.claremont.edu/tp_research.htm]

hairpins [22]. Meanwhile, theoretical works have been done for the translocation of RNA/DNA molecules through nanopores to distinguish each of the four different bases (A, G, C, T) that constitute a stand of DNA [22]. Both experimental and theoretical works show that the transport process of DNA is sensitively influenced by the shape of the nanopore. This method could allow to find the sequence of a human genome only within a couple of hours at a potentially low cost. The sequencing a person's genome with current DNA sequencing technology takes several months and costs millions of dollars. Therefore, further investigations on the transport in confined geometrical structures are needed.

Zeolites

Zeolites are three-dimensional nanoporous crystals with a highly regular framework structures of pores (or cavities) that allow some molecules to pass through, and cause others to be either excluded or broken down [37,44,99,100]. It was originally discovered in the 18th century by a Swedish mineralogist Cronstedt. He observed that upon rapidly heating a natural zeolite, the stones began to dance as the water evaporated. Nowadays, more than 170 unique zeolite frameworks have been identified, and over 40 natural zeolite frameworks were found [99]. In general, zeolites consist of silicon, aluminum and oxygen in their regular framework. The silocon or aluminum atoms are tetrahedrally connected to each other by sharing oxygen atoms, shown in Fig. 3.9. These small subunits form a cavity (cage), and then in a bulk. All these cavities connect to form long structures with small openings (vacant spaces). The vacant spaces are interconnected and form long channels with discrete sizes depending on the mineral.

The dimensions of the channels can control the maximum size of the molecular or ionic species that can enter the pores of a zeolite and the tiny openings can trap these ions and molecules. The properties, such as the uniform cross section of the pores, the ion exchange properties, the ability to develop internal acidity, make zeolites unique among inorganic oxides and also lead to activity and selectivity. Therefore, zeolites can separate molecules based on size, shape, polarity and degree of unsaturation [44,101]. They act like filters, size selective molecular sieve

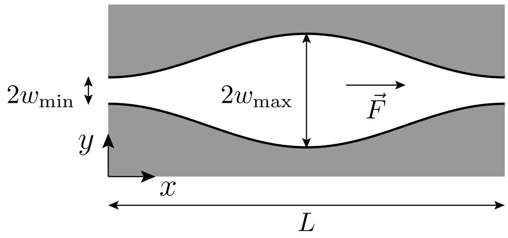

Figure 3.10: Schematic diagram of a single channel with the periodicity L, bottleneck half-width w_{min} and maximal half-width w_{max} [43]. The shape of the structure is described by $\omega(x) = \sin(2\pi x/L) + 1.02$ The constant applied bias $\vec{F}$ acts only along the axial direction of the channel.

separations [102,103]. Besides these, zeolites have been applied as catalysts and ion-exchange materials since 1960, because they have following properties: (1) they have exchangeable cations allowed with various catalytic properties; (2) if these cationic sites are exchanged with H^+, they can have a strong acid sites; (3) the diameters of the pore are less than 1 nm; (4) the pores can have one or more sizes. Because of their porous structure, their applications can be extended to other fields, such as biology [36], industry and nuclear processing [100,104,105].

3.2.1 Modeling of diffusion with confined geometries

In this subsection, we introduce the theoretical model which describes the dynamics of Brownian particle moving in an energetic potential with additional geometrically confined cross-sections (Fig. 3.10). We mainly focus on the 2D-channel, while a very similar line of reasoning could be applied for pore structure in 3D. In particular, we consider a channel with a periodic boundary function $\omega(x)$, which is mirror symmetric with respect to a $2D$ reflection on the channel axis. The diffusive motion of the Brownian particle is then confined by the upper boundary $\omega(x)$ and lower boundary $-\omega(x)$. The channel well $\omega(x)$ with periodicity L, i.e. $\omega(x+L) = \omega(x)$,was assumed to have the sinusoidal profile given by:

$$\omega(x) = A\sin(2\pi\frac{x}{L}) + B\,, \tag{3.19}$$

with two channel parameters A and B. The function $\omega(x)$ is thought to display the first terms of the Fourier series of a more complex boundary function. The motion of the particles through the confined geometry may be caused by different particle concentrations maintained at the ends of the channels, or by the application of external forces acting on the particle. Here, we consider a constant longitudinal external force $\vec{F} = F\vec{e_x}$ pointing into the direction of the channel axis. Then for the overdamped case, the dynamics of a Brownian particle through a channel (or pore) (like the one depicted in Fig. 3.10) in the overdamped limit, is described by the Langevin equation:

$$\eta\,\frac{\mathrm{d}\vec{r}}{\mathrm{d}t} = \vec{F} + \sqrt{\eta\,k_{\mathrm{B}}\,T}\,\vec{\xi}(t)\,, \tag{3.20}$$

where $\vec{r}$ is the position vector of the particle, η, k_B and T have the same meaning as in Section 3.1. The fluctuating force is modeled by zero-mean Gaussian white noise $\vec{\xi}(t)$, obeying the relation $\langle \xi_i(t)\, \xi_j(t')\rangle = 2\, \delta_{ij}\, \delta(t-t')$ for $i, j = x, y$.

In addition to Eq. (3.20), the full problem is set up by imposing reflecting boundary conditions at the channel walls. To simplify the treatment of this model, we introduce dimensionless variables as in Section 3.1. We rescale the length $\vec{r}$, time t, force $\vec{F}$ and energy in the units of L, $\tau = L^2\eta/(k_\mathrm{B}T_\mathrm{R})$, $F_\mathrm{R} = k_\mathrm{B}T_\mathrm{R}/L$ and $k_\mathrm{B}T_\mathrm{R}$, respectively. With these characteristic variables the dimensionless Langevin equation is obtained

$$\frac{\mathrm{d}\vec{r}}{\mathrm{d}t} = -\vec{\nabla}V(x) + \vec{f} + \sqrt{D}\,\vec{\xi}(t)\,, \tag{3.21}$$

where $D = T/T_\mathrm{R}$ denotes the dimensionless temperature, $f = F/F_\mathrm{R}$ is the dimensionless force and $V(x) = U(x)/(k_\mathrm{B}T_\mathrm{R})$ denotes an additional dimensionless energetic substrate potential. Similarly, the dimensionless half-width function defining the upper boundary of the symmetric channel reads

$$\omega(x) = a\sin(2\pi x) + b\,, \tag{3.22}$$

where the boundary function $\omega(x)$ is scaled with the periodicity L. This implies $\omega(x+1) = \omega(x)$ in dimensionless units. Due to the symmetry with respect to the x-axis, it could be given in terms of the maximum half-width of the channel $w_\mathrm{max} = (a+b)$ and the aspect ratio of minimum and maximum width $\epsilon = (b-a)/(a+b)$. Then, the boundary function has the form,

$$\omega(x) = \frac{w_\mathrm{max}}{2}\,(1-\epsilon)\left\{\sin(2\pi x) + \frac{1+\epsilon}{1-\epsilon}\right\}\,. \tag{3.23}$$

The corresponding Fokker-Planck equation for the time evolution of the probability distribution $P(\vec{r}, t)$ of a particle to be found at the position $\vec{r}$ at time t takes the form:

$$\frac{\partial P(\vec{r}, t)}{\partial t} = -\vec{\nabla}\cdot\vec{J}(\vec{r}, t)\,, \tag{3.24a}$$

where $\vec{J}(\vec{r}, t)$ is the probability current:

$$\vec{J}(\vec{r}, t) = -\left(D\vec{\nabla} - \vec{f} + \vec{\nabla}V(x)\right) P(\vec{r}, t)\,. \tag{3.24b}$$

Due to the impenetrability of the channel walls, the normal component of the probability current $\vec{J}(\vec{r}, t)$ vanishes at the boundaries. Therefore, to prevent the particles leaving the channel or being absorbed at the wall, the reflecting boundary condition at the channel walls is:

$$\vec{J}(\vec{r}, t)\cdot\vec{n}(\vec{r}) = 0 \quad \vec{r} \in \text{channel wall}, \tag{3.25}$$

where $\vec{n}(\vec{r})$ denotes the normal vector perpendicular to the channel wall at point $\vec{r}$.

The present situation is considered in high dimensional space with irregular and impenetrable boundaries. Except for a straight channel with ω = constant, the exact analytical solution of the Fokker-Planck equation (3.24) with boundary conditions Eq. (3.25) has not been solved analytically (even for $V(x) = 0$). However, approximate solutions can be obtained by introducing an effective potential to describe the geometric constraints and bottlenecks that act as entropic barriers in a one-dimensional description. For this so-called Fick-Jacobs approximation, there are some limits that will be investigated in more details in the next subsection.

3.2.2 Equilibration assumption: the Fick-Jacobs approximation

The diffusion in a two-dimensional channel or three-dimensional pore of a varying cross- section has been studied by Jacobs [106]. He gave an essential one dimensional treatment of such two or three dimensional problems by introducing an effective potential exhibiting entropic contributions. In his book *Diffusion Processes* [106], written by Jacobs, he gave a heuristic derivation of an effective one-dimensional diffusion equation named as Fick-Jacobs (or F-J) equation [1]. The key point of the derivation is the assumption of fast equilibration in the orthogonal channel direction. Under this assumption, the so-called Fick-Jacobs equation in presence of an applied forcing reads [18],

$$\frac{\partial P(x,t)}{\partial t} = \frac{\partial}{\partial x}\left(D(x)\frac{\partial P(x,t)}{\partial x} + \frac{D(x)}{D}\frac{\partial A(x)}{\partial x}\, P(x,t)\right) , \tag{3.26}$$

where $P(x,t)$ is the probability distribution function along the length of the 2D channel or 3D tube, $A(x)$ is the effective potential function. As the structure changes as the position along the x, the diffusion coefficient $D(x)$ is possibly not a constant, but rather a function of position x, as appeared in Eq. (3.26). To improve the accuracy of the kinetic equation, spatial dependent diffusion coefficient $D(x)$ should be taken into account. Here, we take the form proposed by Regura and Rubi who obtained a scaling law for the diffusion coefficient by simple geometric arguments [108]. It reads

$$D(x) = \frac{D}{(1+\omega'(x)^2)^{\alpha}}\,, \tag{3.27}$$

where $\alpha = 1/3$, $1/2$ for the considered two and three dimensions, respectively [108, 109]. In Eq. (3.26) the free energy $A(x)$ is made up of an energy term, $E = -f\,x$ and an entropic term, $-D\ln s(x)$:

$$A(x) := -f\,x - D\ln s(x)\,, \tag{3.28}$$

where $s(x)$ is the dimensionless width $s(x) := 2\omega(x)$ in two-dimension or the dimensionless transverse cross-section $s(x) := \pi\omega^2(x)$ in three dimension. $\omega(x)$ corresponds to the half-width of the symmetric $2D$ channel or the radius of the pore in

---

[1] Jacobs attributed his treatment to Fick [107].

$3D$. Interestingly, bottlenecks in the channel structure account for entropic contributions in the effective potential function $A(x)$. The height of the effective potential barrier is $\Delta A = -D \ln \epsilon$, which depends on the temperature and the structure of channels.

It was shown that the F-J equation provides a very accurate description of the entropic transport in $2D$ channels and $3D$ tubes with varying cross-section [18, 66, 108–111]. However, we point out that the derivation of the F-J equation entails an approximation that the particle distribution in the transverse direction equilibrates much faster than in the direction of transport [109]. An estimate of this condition can be analyzed by comparing the different time scales involved in the problem.

For the particle moving in a confined geometry, c.f. Fig. 3.10, the time scale of the diffusion in the transverse direction over a distance Δy is $\tau_y = \Delta y^2/2D$. Similarly, the time scale in the axial direction is $\tau_x = \Delta x^2/2D$.

In the absence of an external force, the fast equilibration in the transverse direction requires $\tau_y/\tau_x \ll 1$, resulting in:

$$\frac{\Delta y^2}{\Delta x^2} \sim \omega'(x)^2 \ll 1\,. \tag{3.29}$$

It means $|\mathrm{d}\omega(x)/\mathrm{d}x| \ll 1$ which constitutes the validity criterion for the F-J approximation.

In presence of an external force acting in the axis x-direction, there is a third time scale related to the drift associated to the force: $\tau_{drift} = \frac{L\Delta x}{Df}$. Fast equilibration in the transverse direction occurs if $\tau_y/\tau_{drift} \ll 1$. Consequently,

$$\frac{f\Delta y^2}{2L\Delta x} \sim \frac{2f\omega(x)^2}{L^2} \ll 1\,. \tag{3.30}$$

In general, an estimate of the criteria that has to be satisfied can be put forward by considering the sum of these two ratios, cf. Eqs. (3.29) and (3.30):

$$\omega'(x)^2 + \frac{2f\omega(x)^2}{L^2} \ll 1\,. \tag{3.31}$$

Now, we get a global criteria by averaging the local criteria over the period L of the channel and defining a critical force value f_c. Then, the critical force reads [109]:

$$f_c = \frac{L^2(1 - \langle \omega'(x)^2 \rangle)}{2\langle \omega(x)^2 \rangle}\,. \tag{3.32}$$

Eq. (3.32) provides an estimate of the minimum force guaranteeing the accurate description of the dynamics by the F-J description. Accordingly, the critical force scales asymptotically with L^2 (for a fixed overall shape channel) [109].

3.2.3 Characteristics of entropic transport

Under the validity condition, the Fick-Jacobs approximation provides an accurate description of the biased diffusion of Brownian particles in confined structures. The dynamics include an entropic term arising from the geometrical confinement. The entropic transport exhibits striking and sometimes counterintuitive features, which are different from what is observed in energetic systems and for the purely energetic case. For particle transport, the most interested quantities are: the average particle current $\langle \dot{x} \rangle$ and the effective diffusion coefficient D_{eff}. In the following we study theoretically and numerically these characteristics of the entropic transport for different confinement parameters.

Firstly, we calculate the average particle current $\langle \dot{x} \rangle$ and the effective diffusion coefficient D_{eff} through approximate analysis. Based on the Fick-Jacobs equation Eq. (3.26), an analytical expression for the approximate transport characteristics can be obtained. In particular, the average particle current $\langle \dot{x} \rangle$ has the form [21,66,109]:

$$\langle \dot{x} \rangle = \frac{1 - e^{-f/D}}{\displaystyle\int_0^1 I(z)\,\mathrm{d}z}\,, \tag{3.33}$$

where the integral function $I(z)$ is given by,

$$I(z) = \frac{e^{A(z)/D}}{D(z)} \int_{z-1}^{z} \mathrm{d}y\, e^{-A(y)/D}. \tag{3.34}$$

The effective diffusion coefficient reads [21,66,109,112]

$$D_{\mathrm{eff}} = D\, \frac{\displaystyle\int_0^1 \int_{x-1}^{x} \frac{D(z)\, e^{A(x)/D}}{D(x)\, e^{A(z)/D}} \left[I(z)\right]^2 \mathrm{d}x\,\mathrm{d}z}{\left[\displaystyle\int_0^1 I(z)\,\mathrm{d}z\right]^3}\,. \tag{3.35}$$

Secondly, these two approximate transport quantities can also be obtained by precise numerical simulations. We perform Brownian dynamic simulations by integrating the Langevin equation Eq. (3.21) with the stochastic Euler-algorithm. Then, the average particle current $\langle \dot{x} \rangle$ in x-direction and the corresponding effective diffusion coefficient can be obtained (c.p. Appendix A.2).

Comparing the numerical simulations and the analytical results for different channel structures in Fig. 3.11, we can have a better understanding of the validity limit of the Fick-Jacobs equation. When the temperature or equivalently the noise D decreases, the time scale in the transverse direction over a distance Δy in the form as $\tau_y = \frac{\Delta y^2}{2D}$ increases. So the fast assumption is not valid, and the analytical prediction for low temperature fails. On the other hand, the analytical description matches better with the simulations for small values of $\omega_{\max}$, i.e. smooth geometries [42, 66, 109]. Due to the assumption of fast equilibration in the transverse direction fails, the accuracy of the Fick-Jacobs approximation becomes worse for larger width of the channel $\omega_{\max}$ or smaller noise D. Note that, the applicability of the analytical description depends on the parameter we focus on, i.e. the average particle current $\langle \dot{x} \rangle$ or the effective diffusion coefficient D_{eff}.

Fig. 3.11 depicts the average particle current $\langle \dot{x} \rangle$ and the effective diffusion coefficient D_{eff} for different maximum width $\omega_{\max}$ of the channel, while we fix the ratio

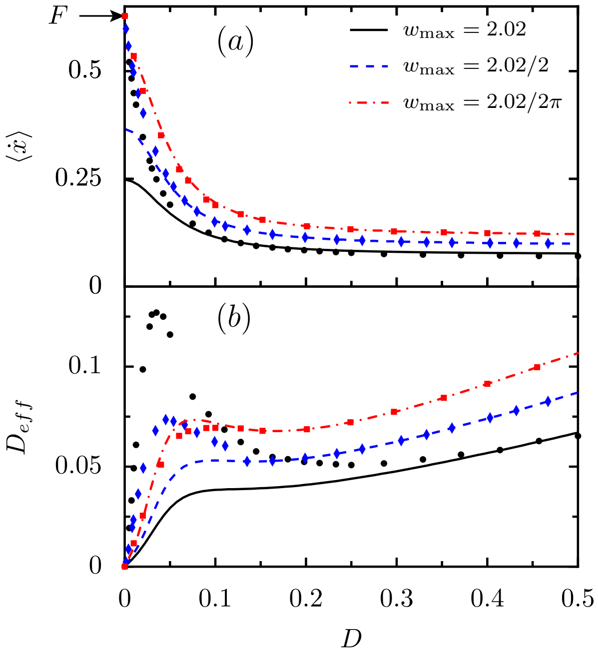

Figure 3.11: Noise (temperature) dependence of: (a) the average particle current (b) the effective diffusion coefficient for a symmetric two-dimensional channel with a constant aspect ratio $\epsilon = 0.01$ at an external force value $f = 0.628$ [43]. The shape of the channel structure is defined by Eq. (3.23). The arrow indicates the particle current in the deterministic limit for which the particle current equals f. The different lines correspond to approximate solutions given by Eqs. (3.33) and (3.35). The different symbols correspond to the precise numerical simulations.

of the minimum and maximum width ϵ. Consequently, the minimum width $\omega_{\min}$, i.e. the width at the bottlenecks, has been changed by modifying the maximum width $\omega_{\max}$. The advantage of this scaling is related to the specific consideration that it keeps a fixed height of the entropic barriers which is determined by the ratio ϵ of minimum and maximum width, i.e. $\Delta A = -D \ln \epsilon$. In this setup, only the curvature of the effective potential at the minima and maxima are allowed to be changed. Obviously, the average particle current $\langle \dot{x} \rangle$ decreases with increasing effective temperature D. This is in contrast to the transport over purely energetic potential barriers, in which case the particle current increases when the temperature is increased [113] (c.f. Fig. 3.4). The transport is dictated by the height of the potential barriers, i.e. $\Delta A = -D \ln \epsilon$ for the entropic transport. As $\ln \epsilon < 0$, the height of the barriers increases as the temperature increases, which leads to the suppression of particle current, c.f. Fig. 3.11(a). In the deterministic limit, i.e. $D \to 0$ the average particle current tends to the same value as the applied bias F irrespective of the maximum channel width (see the symbols in Fig. 3.11 (a)). In this limit, the particles do not diffuse to the side bags of the channel structure and move within a region defined by the width $2\omega_{\min}$ at the bottleneck. Therefore, the particles should have the same velocity as the free particles diffusion under bias. As the fast equilibrium assumption fails for low temperature regime, this observation is not captured by the analytics. Some further details can be found in Ref. [66].

As the maximum width increases, the area of the side bags increases, which

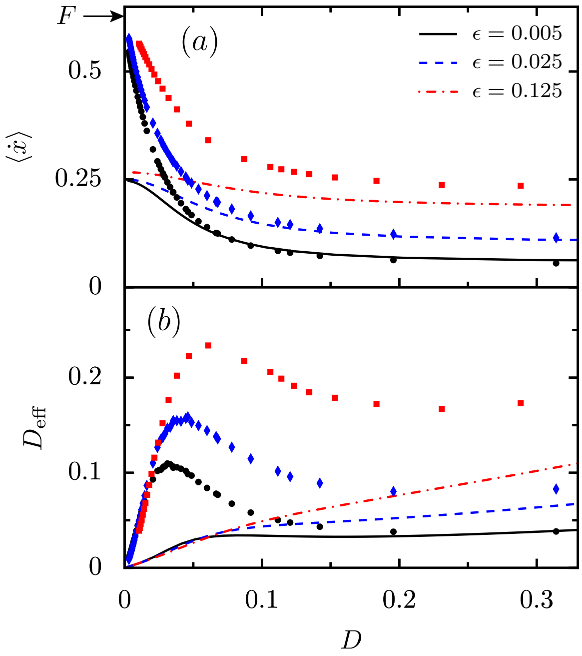

Figure 3.12: Noise (temperature) dependence of: (a) the average particle current (b) the effective diffusion coefficient for a symmetric two-dimensional channel for various values of aspect ratio ϵ with a constant maximum half-width $\omega_{\rm max} = 1$ and an external force value $f = 0.628$ which is labeled by the arrow [43]. The shape of the channel structure is defined by Eq. (3.23). As in Fig. 3.11, the different lines correspond to approximative analytic results and the different symbols correspond to the precise numerical simulations.

means there is more space available along the orthogonal direction. Consequently, the particle spends more time diffusing in this direction. Therefore, larger maximum width can suppress the particle current in the channel direction and enhance the effective diffusion, c.f. Fig. 3.11 (a) and (b). The effective diffusion coefficient exhibits a non-monotonic behavior which corresponds to the giant enhancement of diffusion found for the energetic transport. Moreover, for small values of $w_{\rm max}$ i.e. smooth geometries, the analytical description (average particle current from Eq. (3.33) and the effective diffusion coefficient Eq. (3.35) leads to better results whereas it fails for large $w_{\rm max}$ in small D range [42, 109].

If we keep the maximum width $w_{\rm max}$ constant and increase the ϵ-value, the height of the entropic barrier in our system is reduced. The same transport characteristics: average particle current $\langle \dot{x} \rangle$ and effective diffusion coefficient $D_{\rm eff}$ as the functions of noise are plotted in Fig. 3.12. Since the larger ϵ-value represents lower height of the entropic barrier, the enhancement of $\langle \dot{x} \rangle$ has been found.

From Fig. 3.11 and 3.12, we can see that the average particle current $\langle \dot{x} \rangle$ sensitively depends on the geometric parameters of the channel, so it can be controlled effectively by manipulation of the half-width $\omega_{\rm max}$ and ϵ. This provides great possibility to design stylized channel geometries for which the quality of the particle transport can be efficiently optimized.

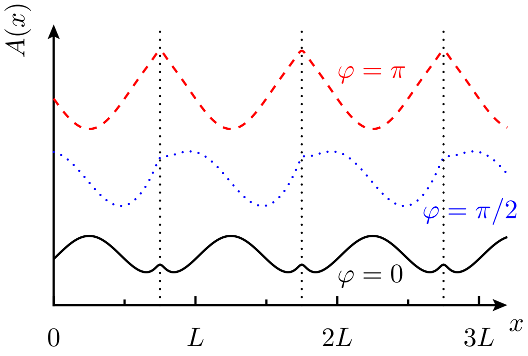

Figure 3.13: The free energy function $A(x)$, c.f. Eq. (3.36), is depicted for different values of the phase shift φ labeled in the figure [45]. All the other parameters are $V_0 = 1$, $f = 0$, $D = 0.2$ and the boundary function has the shape $\omega(x) = \sin(2\pi x)/(2\pi) + 1.02/(2\pi)$. In order to make the lines not overlapping each other, we added constants to the free energy function. The vertical dotted lines correspond to the positions of the bottlenecks of the channel.

Entropic transport in presence of substrate potentials

Now, we add an energetic potential $U(x)$ which exhibits the same periodicity as the channel to the system studied in the forward subsection. The additional energetic potential leads to an energetic contribution to the free energy $A(x)$ which has the form:

$$A(x) = V(x) - fx - D \ln s(x)\,, \tag{3.36}$$

where, $V(x) = V_0 \sin(2\pi x + \varphi)$ is the dimensionless energetic potential of $U(x)$, with amplitude V_0 and additional phase shift φ. Note that, all the parameters in Eq. (3.36) are dimensionless, and retain the same meaning as introduced in Section 3.2.1. This energetic potential function is independent on the transversal coordinate. The free energy function is depicted in Fig. 3.13 at three different values of the phase shift for a fixed channel geometry.

To investigate the interplay between energetic and entropic contributions to the effective free energy, we first study the nonlinear mobility $\mu = \langle \dot{x} \rangle / f$. The average particle current $\langle \dot{x} \rangle$ has an analytical expression as in Eq. (3.33) with the free energy $A(x)$ given by Eq. (3.36). Accordingly, the nonlinear mobility reads [114],

$$\mu = \frac{1 - e^{-f/D}}{f \displaystyle\int_0^1 \frac{e^{A(z)/D}}{D(z)} \int_{z-1}^{z} e^{-A(y)/D}\, \mathrm{d}y\, \mathrm{d}z}\,. \tag{3.37}$$

In the asymptotic high-noise limit, i.e. $D \to \infty$, the nonlinear mobility reduces to

$$\lim_{D\to\infty} \mu = \frac{1}{\displaystyle\int_0^1 \omega(x)\mathrm{d}x \times \int_0^1 \mathrm{d}x \frac{(1 + \omega'(x)^2)^\alpha}{\omega(x)}}\,. \tag{3.38}$$

Note that, here the nonlinear mobility μ for high-noise limit depends only on the channel geometry $\omega(x)$. It has no relation with the energetic potential $V(x)$ or the force f any more.

In the deterministic limit i.e. $D \to 0$, there is no entropic contribution. The nonlinear mobility tends to the value for the energetic transport, i.e. Eq. (3.18). The free energy function reduces to $A(x) = V_0 \sin(2\pi\, x + \varphi) - f\, x$. The critical value ${V_0}^c$ below which the potential profile does not exhibit any minima is

$$ {V_0}^c = \frac{f}{2\pi} \, . \tag{3.39} $$

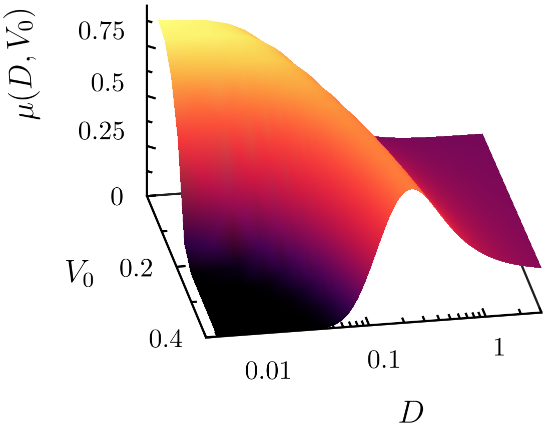

Figure 3.14: Dependence of nonlinear mobility μ Eq. (3.37) on the noise level D and the amplitude V_0 of the external energetic potential [45]. Other parameters are $\omega(x) = \sin(2\pi x)/(2\pi) + 1.02/(2\pi)$, $\varphi \;=\; 0$ and $f = 1$ which makes the critical amplitude keep the value as ${V_0}^c = 0.159$.

For medium noise strengths, some peculiar behaviors are found. Fig. 3.14 depicts the behavior of the nonlinear mobility μ as a function of the amplitude V_0 of the periodic potential and the noise strength D for fixed phase shift $\varphi = 0$. Interestingly, μ exhibits different behaviors for the sub and suprathreshold energetic force. For suprathreshold energetic forcing, i.e. $V_0 < {V_0}^c$ ($f > 2\pi V_0$), the nonlinear mobility μ decreases monotonically with D as observed in the case of $V_0 = 0$ (the absence of an energetic substrate potential). This matches with the behavior of the average particle current $\langle \dot{x} \rangle$ in Fig. 3.11 (a) and Fig. 3.12 (a) for the purely entropic situation. For subthreshold energetic forcing $f < 2\pi V_0$ ($V_0 > V_0^c$), we found a resonance-like behavior with noise strength D: The mobility μ initially increases until it reaches a maximum and then decreases again. This behavior has never appeared in either purely energetic transport (c.f. Fig. 3.4 the mobility monotonically increases with noise strength D) or purely entropic transport (c.f. Fig. 3.11 (a) and Fig. 3.12 (a), the mobility monotonically decreases with noise D). The resonance-like behavior is induced by the competition between energetic and entropic contributing to the free energy. For small noise, the energetic contribution dominates the free energy function and noise-assisted transport is observed. Consequently, the nonlinear mobility μ initially increases with rising D. A further increasing of the noise level D raises the entropic contribution to the free energy function and induces the decreasing of the nonlinear mobility μ.

However, this resonance-like behavior is not observed for all subthreshold energetic forcing. It appears only if there are two potential barriers in one period of

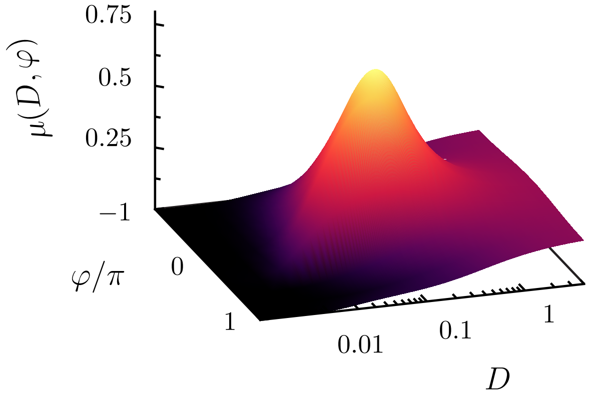

Figure 3.15: Nonlinear mobility μ, c.f. Eq. (3.37), versus the noise level D and the phase shift φ [45]. All the other parameters used here are $f = 1$, $V_0 = 0.2 > V_o^c$ and $\omega(x) = \sin(2\pi x)/(2\pi) + 1.02/(2\pi)$.

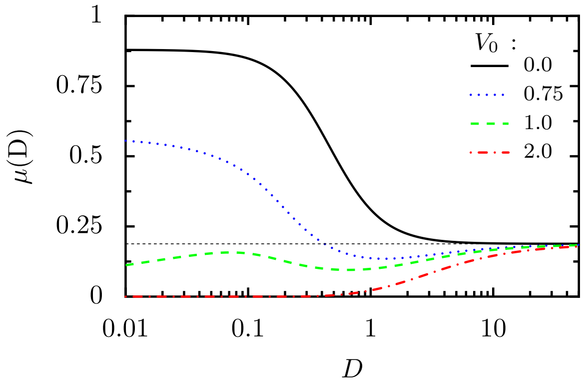

Figure 3.16: Nonlinear mobility μ as a function of the noise level D for various amplitudes V_0 of the energetic potential while fixing $f = 2\pi$ ($V_0{}^c = 1$), $\varphi = \pi$ and $\omega(x) = \sin(2\pi x)/(2\pi) + 1.02/(2\pi)$ [45]. The dashed horizontal line is 0.188 predicted by Eq. (3.38) in the limit of $D \to \infty$.

the free energy function $A(x)$ shown in Fig. 3.13. These two potential barriers arising from the energetic substrate potential and the geometric restrictions should be treated separately, for example in the case $\varphi = 0$. On another sides, if the energetic and entropic barriers coincide at the same locations, i.e. for $\varphi = \pi$, the nonlinear mobility μ monotonically increases with increasing noise level D for subthreshold forcing, c.f. Fig. 3.15. In this case, c.f. $\varphi = \pi$, a peculiar scenario can be observed for amplitude values V_0 of the energetic potentials smaller than the critical one, i.e. for the case of suprathreshold driving, c.f. Fig. 3.16 [114]. Especially, for the critical amplitude $V_0^c = 1$, the competition between energetic and entropic contributions sensitively depends on the noise level D.

For $V_0 = 0$, the nonlinear mobility μ decreases monotonically with D, due to the dominant entropic contribution, while for $V_0 \ll V_0^c$ in the subthreshold case $f > 2\pi V_0$, it increases due to the dominant energetic contribution. For some intermediate values of V_0, μ exhibits a small peak at optimum values of the noise level D. This is due to the complex interplay between energetic and entropic contributions to the free energy profile. However for the limit $D \to \infty$, the nonlinear mobility tends to the limiting value predicted by Eq. (3.38), c.f. Fig. 3.14, Fig. 3.15 and Fig. 3.16.

3.3 Conclusions

We have given a brief introduction to the transport properties of the energetic and entropic transport (confined geometries). Based on a simplified mathematical framework, the dynamic properties of Brownian particles in both energetic and entropic transport can be tackled. In particular, the particle diffusion under the influence of noise which acts as a stochastic force can be well modeled by Langevin and Fokker-Planck equations. Within this framework, the two most interesting transport quantities such as the average current $\langle \dot{x} \rangle$ and the effective diffusion coefficient D_{eff} can be conveniently analyzed. For the nano-scaled transport, the geometrical confinement must be taken into account and we need to deal with the novel entropic transport. The intrinsic confinement has been found to play a very important role on the system's dynamics. Starting from the Fokker-Planck equation, we can obtain the Fick-Jacobs equation based on the fast equilibrium assumption along the cross sections. Specifically, the motion of Brownian particles with geometrical confinement can be modeled by this approximation where an additional entropic term due to the confinement appears. The additional entropic barrier arising from the intrinsic geometrical confinement is responsible for numerous new and nontrivial dynamic behaviors. The average current $\langle \dot{x} \rangle$ is suppressed by the increase of effective temperature, which is totally in contrast to the energetic transport where the thermal activation actually induces the particle current. Furthermore, we have found that the average current $\langle \dot{x} \rangle$ and the effective diffusion coefficient D_{eff} depend sensitively on the structures of the channels. This effect offers a convenient way to control the motion of Brownian particles as desired and makes the analysis of the properties of the particles more feasible. Furthermore, we have considered the system subjected to an periodic energetic potential with the same periodicity as the channels and investigated the intrinsic interplay between the energetic and entropic contributions to the transport. In presence of this periodic energetic potential, a resonance-like behavior was found for the mobility. This bell-shaped behavior of the mobility μ can be easily controlled by modulating the amplitude or phase shift of the periodic energetic potential.

4 Neuronal signaling

In the last 50 years, there were lots of theoretical and experimental studies on the problem of generation and propagation of neuronal signals. A milestone was done in the 1950's by Hodgkin and Huxley who successfully introduced a theoretical model for the squid giant axon [28]. Since then, a large number of excellent papers and books addressing in great details of various aspects of the Hodgkin-Huxley model have been published. In Section 4.1, we give a brief introduction of this model in order to explain the biophysical mechanisms of the generation of action potentials. Moreover, some important results for this model will be presented. In Section 4.2, the effect of intrinsic channel noise will be investigated for the dynamics of a neuronal cell with a delayed feedback loop. This kind of loop is based on the so-called autapse phenomenon, in which dendrites are able to establish connections to its own axon. For small noise, the synchronization phenomena can be found between the delay time and the intrinsic characteristic time scale determined by noise. The results have been published in Ref. [115]. In addition, we will study the noise-assisted propagation of action potentials in myelinated axons in Section 4.3. For the spike propagation in terms of transmission reliability which is the ratio of the number of spikes observed in the terminal node to the number of spikes initiated in the first node, we found a breakdown of the propagation induced by the intrinsic noise. The findings have been published in Ref. [116]. Conclusions will be made in Section 4.4.

4.1 Ions transport across neuronal membranes

In nervous systems, electrical signals are carried primarily by transmembrane ion currents. The currents consist of different ions: potassium (K^+), sodium ($\mathrm{N}a^+$), calcium ($\mathrm{C}a^{2+}$) and chloride ($\mathrm{C}l^-$). The first three types of ions carry positive charges (cations) whereas the fourth one carries negative charge (anion). These ions are not uniformly distributed in nervous systems. There is a concentration difference of these kinds of ions between intracellular and extracellular space. Such difference of ions results in the concentration gradients or chemical potentials which induce the ions diffusion. The ionic concentration gradient is maintained by ion pumps, whose energy is derived from hydrolysis of ATP molecules. Normally, the negative charges gather together with an excess concentration on the inside surface of the cell membrane. At the same time, equal density of positive ions from the intercellular medium to the outside surface forming an electrochemical potential across the membrane, which drives the flow of ions. As the ions are charged, the movement of them depends not only on their concentration gradients but also on the electric fields.

The movement of ions can be described by physical laws. However, the mechanism for the ionic transport across the membrane is quite complicated. Ions move across the membrane through aqueous pores (the ion channels) formed by transmembrane proteins. These channel proteins act like gates to control the passage of ions. The principles of ion movement and channel gating have been extensively studied by physiologists for at least 100 years. The first quantitative model describing the spike generation and propagation was proposed by Alan Hodgkin and Andrew Huxley [28]. Their model known as the Hodgkin-Huxley model is the most important landmark in the study of the generation and propagation of electric signals for nervous systems. In this section, we will give an overview of these concepts and model to study the ion transport across neuronal membranes.

4.1.1 Excitable membrane dynamics

To study the electrical signals in cells, it is useful to divide the cell types into two classes: excitable cells and nonexcitable cells. Most cells maintain a stable equilibrium potential. The nonexcitable cells are those, for which if a current stimulus applied to the cell for a short time, the potential returns directly to the equilibrium potential after the applied current is removed. The excitable cells are those, for which the membrane potential can go through a large excursion, c.f. action potential, and then return to the equilibrium potential, if the applied current is strong enough. In the following sections, we focus on the processes in excitable cells.

Structure and function of the cell membrane

The cell membrane is built up with a lipid bilayer of phospholipids, which makes it impervious for most water-soluble molecules. Phospholipid is a long molecule, with polar head group and two hydrophobic hydrocarbon tails. The phospholipid molecules stick to each other with their hydrophobic tails forming a bilayer, and the polar heads facing intracellular cytoplasm and the extracellular space. Therefore, the membrane separates the internal and external conducing solutions by a layer around 3-4 *nm* thick (shown in Fig. 3.6).

The cell membrane is selectively permeable and defines whether the certain type of ions is allowed to penetrate a cell or not. The permitting free passage of some ions and restricting passage of others regulate the flow of these ions and maintain a concentration difference. The membrane also contains water-filled pores which are called *channels*. More details will be presented later.

On both sides of the membrane, there are aqueous solution of dissolved salts, primarily NaCl and KCl which can be dissociated into Na^+, K^+ and Cl^-. The molecules are transported across the membrane by passive or active processes. The active processes require energy from hydrolysis of adenosine triphosphate (ATP) to build up the concentration gradient or electrical potential, while the passive process results from the inherent, random movement of molecules. The active mechanisms need energy to pump ions to form and maintain the concentration differences. The concentration gradient creates a potential difference across the membrane that drives the ionic current.

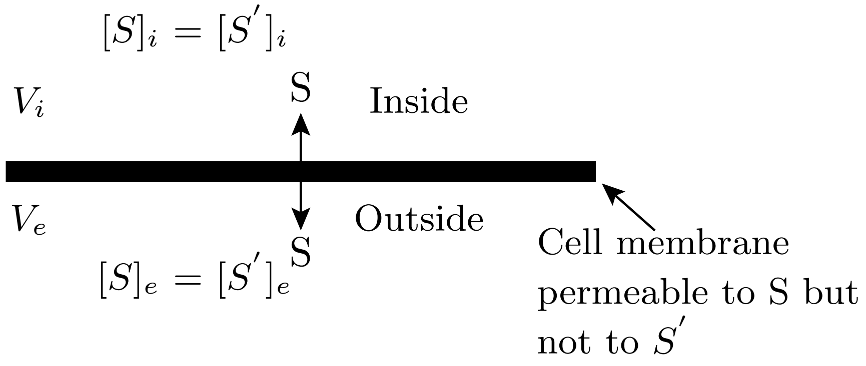

Figure 4.1: Schematic diagram of a semipermeable membrane separating two solutions with different concentrations.

Membrane potential

Ions are not uniformly distributed in cells, such as the concentration of K^+ inside the cells is much higher than the value in extracellular space, while the concentration of Na^+ is distributed in the opposite way. Such concentration differences result in the diffusion of ions across the cell membrane. Typically, Na^+ and Ca^{2+} move into the neuron as they have higher concentrations outside the cell, while K^+ flows in the opposite direction. As the ions are charged, the movement is determined not only by the concentration gradients, but also by electric fields. Since most membranes are permeable only to some special ions, the charged ions are separated across the membranes. Therefore, an electric field is built up, and influences the movement of ions. In summary, the ionic transport creates a potential difference across the membrane, and these potential changes are the primary signals carrying biological information.

To understand the principal function of the transport process in a simplified way, we consider two reservoirs containing the same type of ion S, but with different concentrations, as shown in Fig. 4.1. The reservoirs are separated by a semipermeable membrane which is permeable to ion S but not to others. As the solutions on both sides of the membrane are assumed to be electrically neutral (at least initially), there must be another ion S' with the opposite sign to keep balance. For example, S could be a negative ion Cl^-, while S' could be positive ion, such as Na^+ or K^+. As shown in Fig. 4.1, the upper part of the membrane represents the inside of the membrane, while the under part denotes the outside.

Due to the ion transporters (pumps) and selective permeability of ions across the membrane, the concentration is different for ions S and S'. This allows ion S to diffuse from inside to outside of the cell. The diffusion of S induces a separation of charges across the membrane. Consequently, an electric field is set up to oppose the further diffusion of S across the membrane. An equilibrium state is achieved when the electric field balances the concentration driven diffusion of S. The equilibrium potential of the ion species in terms of their concentrations inside and outside of the membrane can be explicitly expressed by the Nernst equation,

$$V_S = \frac{RT}{zF} \ln\left(\frac{[S]_e}{[S]_i}\right) = \frac{k_{\mathrm{B}}T}{zq} \ln\left(\frac{[S]_e}{[S]_i}\right) . \tag{4.1}$$

Here, $[S]_i$ and $[S]_e$ denote internal and external concentration, respectively, R is the universal gas constant, T is the absolute temperature, z is the charge value of ion S, k_{B} is Boltzmann's constant, and q is a proton's charge. At fixed temperature, the value of RT/F can be assumed to be constant. Sometimes, the equilibrium potential is also referred to as the Nernst potential. For nerve cells, it is also named as reversal potential. Note that, the membrane potential V is defined as the difference of intracellular V_i and extracellular V_e potentials,

$$V = V_i - V_e . \tag{4.2}$$

For convenience, the potential of the outside solution (extracellular fluid) is set to zero. Typically, the concentrations of the four major ions in most cells follow the same rules: $[\mathrm{K}^+]_{in} > [\mathrm{K}^+]_{out}$, $[\mathrm{Na}^+]_{in} < [\mathrm{Na}^+]_{out}$, $[\mathrm{Cl}^-]_{in} < [\mathrm{Cl}^-]_{out}$, $[\mathrm{Ca}^{2+}]_{in} < [\mathrm{Ca}^{2+}]_{out}$. According to the Nernst equation Eq. (4.1), the Nernst potential of Na^+ and Ca^{2+}, which are denoted by E_{Na} and E_{Ca} respectively, are positive, E_{K} and E_{Cl} are negative. Typically, the neuronal membrane potentials vary in the range between -90 and 50 mV [117].

At the reversal potential V_{rev}, the ionic current is zero, i.e. $V_S = V$. Thus, the diffusion of S is exactly balanced with the electric forcing at V_{rev}. Note that the reversal potential can be used as synaptic potential to define excitatory or inhibitory responses: Synapses with reversal potentials above the action potential threshold are called excitatory, while those with reversal potentials below the threshold are named inhibitory.

It is notable that the Nernst equation does not depend on the way how the ions move across the membrane, and is only related to the concentration difference. However, this equation Eq. 4.1 is true when there is only one type of ions moving across the membrane. The situation is more complicated in the case of more than one type of ions that can cross the membrane. For the multiple ion types, the vanishing total current does not imply that there is no net current for each individual ion. Therefore, in the situation with multiple ion types, the equilibrium potential can not be described by Nernst equation any more. The relative permeability of the membrane to individual ion should be taken into account. A model has been proposed by Goldman [118], Hodgkin and Katz [119] based on the assumptions that, (1) the movement of ions obeys the Nernst equation; (2) ions cross the membrane independently (without interaction with each other); and (3) the electric field in the membrane is constant. They obtained the expression:

$$E_S = \frac{k_{\mathrm{B}}T}{q} \ln\left(\frac{P_{\mathrm{Na}}[\mathrm{Na}^+]_e + P_{\mathrm{K}}[\mathrm{K}^+]_e + P_{\mathrm{Cl}}[\mathrm{Cl}^-]_i}{P_{\mathrm{Na}}[\mathrm{Na}^+]_i + P_{\mathrm{K}}[\mathrm{K}^+]_i + P_{\mathrm{Cl}}[\mathrm{Cl}^-]_e}\right) , \tag{4.3}$$

where P is the membrane permeability for the specific ions. This is the so-called Goldman-Hodgkin-Katz (GHK) equation. It describes the steady state membrane

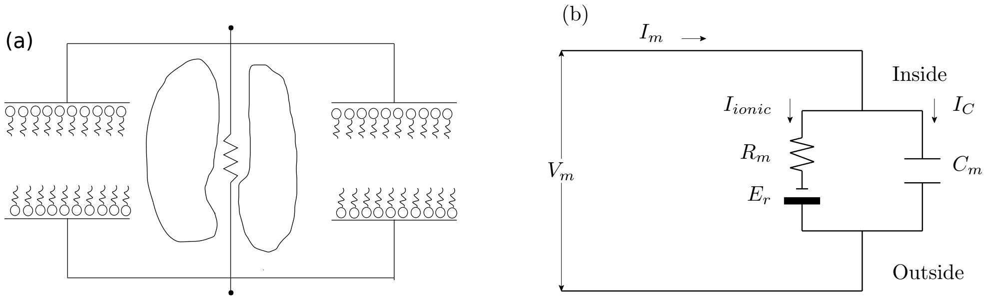

Figure 4.2: Equivalent circuit (b) models the biological membrane (a). Parameters are given in the figure (b).

potential which is referred to as the *rest potential.* In most cells, the permeability to potassium ions is almost 10 times higher than that to sodium ions at the rest state. Consequently, the rest potential is usually close to the potassium reversal potential which is around -65 mV.

Electrical properties of the cell membrane

Since the cell membrane separates the charged ions, it can be viewed as a capacitor. The movement of ions exhibits properties which are similar to those in electric circuits. Therefore, it is natural to describe the dynamical behavior of the membrane in terms of electric circuits. A typical membrane structure and an equivalent electric circuit are depicted in Fig. 4.2. It is assumed that the membrane acts like a capacitor in parallel with a resistor.

The capacitance of the circuit which denotes the membrane dielectric properties is determined by the properties of the liquid bilayer. In membrane biophysics, it is normally specified in terms of the specific membrane capacitance C_m which is the capacitance per square centimeter. The value of the specific membrane capacitance C_m is determined by the thickness and dielectric constant of the bilipid layer. Generally, it is between 0.7 and 1 μF/cm^2, and we adopt 1 μF/cm^2 for convenience.

Based on the equivalent circuit shown in Fig. 4.2 and the Kirchhoff's laws, the total current I_m flowing across the membrane can be written as the sum of capacitive current I_C, and ionic current I_{ionic}:

$$I_m = I_C + I_{ionic} = C_m \frac{dV_m}{dt} + I_{ionic}, \tag{4.4}$$

where V_m is the membrane potential, in the unit of mV, the time measured in ms. Since in absence of external driving, there is no current built up of charges on either side of the membrane, the total current is zero. Normally the ionic current I_{ionic} is the sum of all currents from different types of ion species, i.e. $I_{ionic} = I_{\mathrm{Na}} + I_{\mathrm{K}} + ... + I_{\mathrm{Cl}}$. Each ion species corresponds a current which represents a significant challenge to describe. Different ion species may have different current expressions. In theoretical models, it is commonly assumed that the current across the membrane is a linear function of the membrane potential.

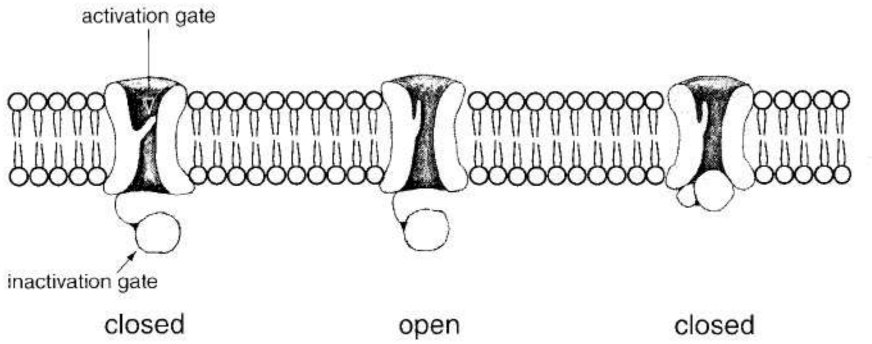

Figure 4.3: Schematic diagram of the channels in different states: close (inactivation gate is closed), open and closed (inactivation gate is closed). [Adapted from K. Bogdanov, Biology in Physics, Academic press (2000)]

Ion channels

A pure liquid bilayer has a very low permeability to any type of ions. However, ion-conducting channels reduce an effective membrane resistance for ionic current to a value of about 10^4 times smaller than that without channels. Therefore, the membrane conductance is determined by the density and types of ion channels. The density of ionic channels is in the range from a few to several thousands units per μm^2 of the membrane.

The ion channel embedded in the cell membrane (shown in Fig. 3.6 in Chapter 3) is a large protein. It forms a protein-lined passageway for specific molecules and ions, such as sodium, potassium, calcium and chlorine. A typical neuron may have a dozen or even more different types of ion channels. Many but not all channels are highly selective, allowing only one type of ion to pass through. Normally, the potassium -specific channels are generally open to generate the rest potential across the membrane. Other Types of channels are usually closed, and open in response to specific membrane potentials, shown in Fig. 4.3 [27]. All these remarkable properties of channels result in the characteristic electrical activities of neurons, such as their ability to conduct, transmit and receive electric signals. The voltage-gated ion channels, such as K^+, Na^+, or Ca^{2+} channels play a fundamental role in the functioning of neurons.

The capacity of channels for conducting ions over the cell membrane is influenced by many factors, such as the membrane potential, the internal concentration of various intra-cellular messagers (such as Ca^{2+} dependent channels) and extra-cellular concentration of neurotransmitters or neuromodulators (like synaptic receptor channels).

To study the contribution of the ion channels to the ionic current, the voltage-gated channels are simplified by a two-state model. Here, we introduce the K^+ channels as an example. A single K^+ channel has four identical subunits, each of which can be in either a closed state C or an open state O, c.f. Fig. 4.4. The rate

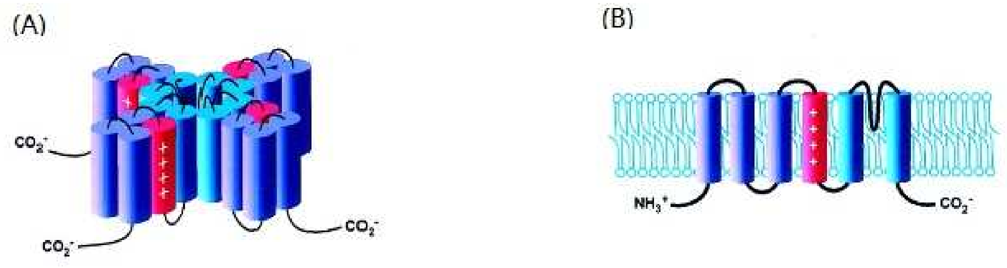

Figure 4.4: (A) Sketch of the four identical subunits in the voltage-gated K$^+$ channel. (B) A proposed structural model of the subunits composing the K$^+$ channel. Each subunit is thought to contain six transmembrane domains: A positively charged S4 region that is the voltage-sensing α helix; C-terminus and N- terminus that contains a globular domain essential for inactivation of the open channel. [Adapted from J. Nerbonne, J. Physiol., **525**, 285-298 (2000).]

of conversion from one state to another is voltage-dependent. Thus,

$$C \; \underset{\beta(V)}{\overset{\alpha(V)}{\rightleftarrows}} \; O\,. \tag{4.5}$$

Here, $\alpha(V)$ and $\beta(V)$ are the transition rate coefficients, with dimension $[\,\mathrm{ms}^{-1}]$, $\alpha(V)\Delta t$ gives the probability that a closed channel opens within a time Δt. The transition between open and closed states is governed by a first-order kinetics equation. With p^{open} denoting the probability of channels in the open state, we can describe the transmission by a first-order differential equation,

$$\frac{\mathrm{d}p^{open}}{\mathrm{d}t} = \alpha(V)(1 - p^{open}) - \beta(V)p^{open}\,. \tag{4.6}$$

We have taken into account the fact that the total number of channels is conserved, c.f. the proportion of closed state is $1 - p^{open}$. The probability for channels being in open state p^{open} is between 0 and 1. The great interest is to determine the probability of channels switching between open and close states in response to the voltage, which has been done by Hodgkin and Huxley. The expressions for $\alpha(V)$ and $\beta(V)$ will be presented in the following sub-section.

4.1.2 Hodgkin-Huxley model

After describing how the cell membrane can be modeled as a capacitor in parallel with an ionic current, and having the knowledge about channels, we will discuss the Hodgkin-Huxley model in this sub-section.

In order to analyze the action potentials generated in nerve cells and axons, Hodgkin and Huxley performed a series of *voltage-clamp* experiments on the squid giant axons [120]. The potential across the cell membrane is measured by patch clamp technique. A microelectrode inserts inside the cell and a reference electrode places in the extracellular space. More details will be presented later. This technique

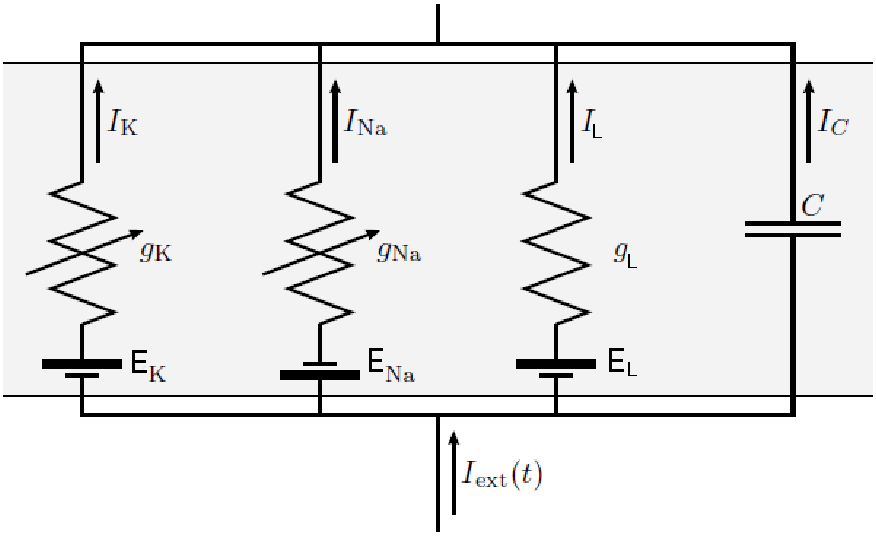

Figure 4.5: Parallel conductance model for the squid axon. Hodgkin and Huxley modeled the membrane of the squid axon with four parallel branches. The conductances g_{K} and g_{Na} depend on both voltage and time, and g_L is constant.

provides a method to measure the transient transmembrane currents which response to the changes of the ionic currents flowing across the membrane [117, 121]. Based on the experimental records of the current as a function of time, Hodgkin and Huxley proposed a model, which quantitatively describes the generation and propagation of action potentials.

The parallel conductance model, which describes the major ionic conductance in the squid axon, is shown in Fig. 4.5. As introduced in Section 4.1.1, the total membrane current is the sum of the capacitive current I_C and the ionic current I_{ionic}, i.e. Eq. (4.4). It equals to the external current I_{ext}. The principal ionic currents are the sodium current I_{Na} which is the initial inward current, and the potassium current I_{K} which is the outward current. I_{Cl} and all the other ionic currents are lumped together into the so-called *leakage current* I_L [120]. Thus, the total ionic current is,

$$I_{ionic} = I_{\mathrm{Na}} + I_{\mathrm{K}} + I_L \, . \tag{4.7}$$

The individual ionic current (I_{Na} and I_{K}) can be measured independently under the voltage clamp condition. Linear current-voltage ($I - V$) curves of sodium and potassium are found from experimental data,

$$I_{\mathrm{Na}}(t) = g_{\mathrm{Na}}(V,t)\,(V(t) - E_{\mathrm{Na}}) \ , \tag{4.8a}$$

$$I_{\mathrm{K}}(t) = g_{\mathrm{K}}(V,t)\,(V(t) - E_{\mathrm{K}}) \ . \tag{4.8b}$$

Here, E_{Na} and E_{K} are the Nernst potential for ion species Na and K, respectively. g_{Na} and g_{K} are the membrane conductance for Na and K which represents the ions permeation across the membrane (mainly through channels), in the unit of S/cm^2. It is notable that, we define a positive current as positive ions moving from inside to outside.

The most important challenge is to determine the membrane conductance g_{Na} and g_{K}. From the experimental data of the conductance of K^+ and Na^+, Hodgkin and Huxley found that: (1) The potassium conductance g_{K} sigmoidally increases and then exponentially decreases. (2) The behavior of g_{Na} is more complicated. They realized that the conductance of potassium g_{K} can be written as some power of a single variable n which satisfies a first-order differential equation. Thus, they proposed,

$$g_{\mathrm{K}} = g_{\mathrm{K}}^{\max} n^4, \tag{4.9}$$

with

$$\frac{\mathrm{d}n}{\mathrm{d}t} = \alpha_n(V)(1-n) - \beta_n(V)n\,, \tag{4.10}$$

where the maximal conductance $g_{\mathrm{K}}^{\max}$ is constant and n is the fraction of the open gates. The fourth power was chosen as the smallest exponent that gave acceptable agreement with the experimental data. Later, experimental observations have shown that the potassium channel should be assumed to consist of multiple identical subunits [122, 123], each of which can switch between closed and open states, see Fig. 4.4. The conductance excites only when all these gates open simultaneously.

The sodium conductance g_{Na} is more difficult to unravel. There are two processes involved: One turns the sodium current on and the other turns it off. This is because the Na^+ channel has two different types of subunits: activation subunits and a inactivation subunit. The mean fraction of activation open gates and inactivation open gates which are devoted by m and h respectively, can be described by first-order differential equations. Hodgkin and Huxley proposed that the sodium conductance has the following form,

$$g_{\mathrm{Na}} = g_{\mathrm{Na}}^{\max} m^3 h, \tag{4.11}$$

with

$$\frac{\mathrm{d}m}{\mathrm{d}t} = \alpha_m(V)(1-m) - \beta_m(V)m, \tag{4.12a}$$

$$\frac{\mathrm{d}h}{\mathrm{d}t} = \alpha_h(V)(1-h) - \beta_h(V)h\,, \tag{4.12b}$$

where $g_{\mathrm{Na}}^{\max}$ is the maximal sodium conductance. Here, m and h are the so-called gating variables. Since the subunits are independent, the probability for the three m and one h gates to active is given by m^3h. Note that the sodium current is completely inactivate when $h = 0$.

The opening and closing rates $\alpha_i(V)$ and $\beta_i(V)$ $(i = m, n, h)$ of the gating variables $m(t)$, $n(t)$ and $h(t)$ were derived by Hodgkin and Huxley [28]. They have the form as,

$$\alpha_m(V) = \frac{0.1(V+40)}{1-\exp\{-(V+40)/10\}}\,, \tag{4.13a}$$

$$\beta_m(V) = 4\exp\{-(V+65)/18\}\,, \tag{4.13b}$$

$$\alpha_h(V) = 0.07\exp\{-(V+65)/20\}\,, \tag{4.13c}$$

$$\beta_h(V) = \frac{1}{1+\exp\{-(V+35)/10\}}\,, \tag{4.13d}$$

$$\alpha_n(V) = \frac{0.01(V+55)}{1-\exp\{-(V+55)/10\}}\,, \tag{4.13e}$$

$$\beta_n(V) = 0.125\exp\{-(V+65)/80\}\,. \tag{4.13f}$$

In summary, the equation Eq. (4.4) has the form as,

$$\begin{aligned} C_m\frac{\mathrm{d}V(t)}{\mathrm{d}t} &+ n^4(t)g_{\mathrm{K}}^{\max}\left(V(t)-E_{\mathrm{K}}\right) \\ &+ m^3(t)h(t)g_{\mathrm{Na}}^{\max}\left(V(t)-E_{\mathrm{Na}}\right) + g_{\mathrm{L}}\left(V(t)-E_{\mathrm{L}}\right) = 0\,. \end{aligned} \tag{4.14}$$

This nonlinear differential equation, in addition to the equations Eqs. (4.10), (4.12) for the conductances and Eq. (4.13) for the related gating variables establish the famous Hodgkin-Huxley model for the potential generation of the space-clamped axon. Now, we present some numerical results which provide quantitative understanding of the dynamics of Hodgkin-Huxley model.

First of all, the rest potential E_S can be obtained when the total membrane current vanishes. That is,

$$n^4 g_{\mathrm{K}}^{\max}\left(V-E_{\mathrm{K}}\right) + m^3 h g_{\mathrm{Na}}^{\max}\left(V-E_{\mathrm{Na}}\right) + g_{\mathrm{L}}\left(V-E_{\mathrm{L}}\right) = 0\,. \tag{4.15}$$

The steady states for n, m and h which are obtained from Eqs. (4.10) and (4.12) have the following form,

$$n = \frac{\alpha_n(V)}{\alpha_n(V)+\beta_n(V)}\,, \tag{4.16a}$$

$$m = \frac{\alpha_m(V)}{\alpha_m(V)+\beta_m(V)}\,, \tag{4.16b}$$

$$h = \frac{\alpha_h(V)}{\alpha_h(V)+\beta_h(V)}\,. \tag{4.16c}$$

The steady state solution E_S of Eq. (4.15) approaches a unique, asymptotically stable equilibrium point. For the squid giant axon, the rest potential is $E_S \simeq 65\,\mathrm{mV}$. Note that, the Hodgkin-Huxley model stays at the rest state without external stimulus. Nevertheless, the action potential can be produced by an external current. Fig. 4.6 shows a typical action potential and the corresponding n, m and h in response to an initial external stimulus $I_i = 12\,\mu\mathrm{A/cm}^2$.

Under the initial stimulus condition, there is a competition among the three major ionic currents, i.e. I_{Na}, I_{K} and I_L. All of them try to drive the potential to

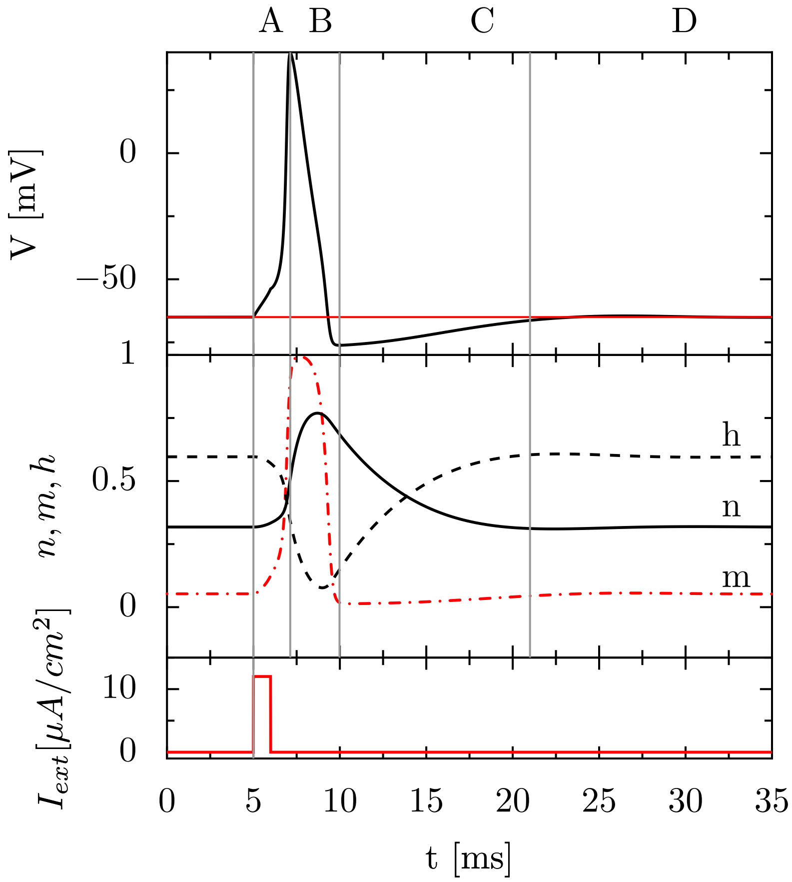

Figure 4.6: Schematic diagram of a typical action potential generated by an external current stimulus. The important points are labeled as: A - depolarizing; B - repolarizing; C - recovery; and D - rest state.

the corresponding rest potential. However, m responds much faster to the changes of potential $V(t)$ than either n or h. Therefore, with the initial stimulus current, the potential is elevated, and m is tracking to a bigger value. If the stimulus is big enough, m will increase sufficiently to change the sign of the net current, which results in an autocatalytic inward sodium current. It means that, the raise of potential makes m continue to rise, and the inward sodium current is increased, which further drives the potential increasing. However, the increasing of potential induces a closing of the h-gate and h decrease toward zero. As h approaches zero, which induces g_{Na} toward zero, so the sodium current vanishes. As m responds much faster to the stimulus, the sodium current firstly turns on and then turns off. Correspondingly, the potential increases at first and then decreases (see Fig. 4.6). As h and n have the similar responce time [120], at about the same time that the sodium current is inactivate, the outward potassium current is activated. Activation of the potassium current drives the potential below the rest potential toward its rest potential E_{K}. When V is negative and n decreases, the potential eventually returns to the rest potential. The whole process which expresses as a spike is completed and can start again.

The whole process of a typical action potential can be divided into four phases: the *depolarizing*, *repolarizing*, *recovery* and *rest state* phases. Each phase is represented by a capital letter in Fig. 4.6. It is notable that, during an action potential a second stimulus can not cause new action potential, even the second stimulus is very big. The period that marked as A in Fig. 4.6, is referred to as *absolute refractory period*. Generally, this time interval is about 2 ms [124, 125]. Within the repolarizing and recovery phases (B and C in in Fig. 4.6), a second action potential can be produced but only if the stimulus is considerably greater than the threshold. This period is called *relative refractory period*.

The Hodgkin-Huxley model is able to give a quantitative account of the generation of electrical signal along a squid giant axon. As this experimentally testable model embodies the major properties of membrane, it has been extended and applied to a wide variety of excitable systems. This is why the Hodgkin-Huxley model has been thought to be the milestone in the classical biophysics.

4.1.3 Stochastic Hodgkin-Huxley model

In the previous sub-section, we have introduced the Hodgkin-Huxley model which describes the dynamics of the generation of action potentials. This model is a triumph of the classical biophysical model being able to answer a fundamental biological questions [126]. However, this macroscopic and deterministic model cannot exactly capture the kinetics of the channels, which are obtained from the new experiments like single-channel recording. The influence of conductance fluctuations arising from the random opening of ion channels should be considered as well. This section is dedicated to extend the original (deterministic) Hodgkin-Huxley model to a stochastic model.

It turns out that the individual ion channels are stochastic devices from the single channel recordings by Neher and Sakmann [127, 128]. The populations of the

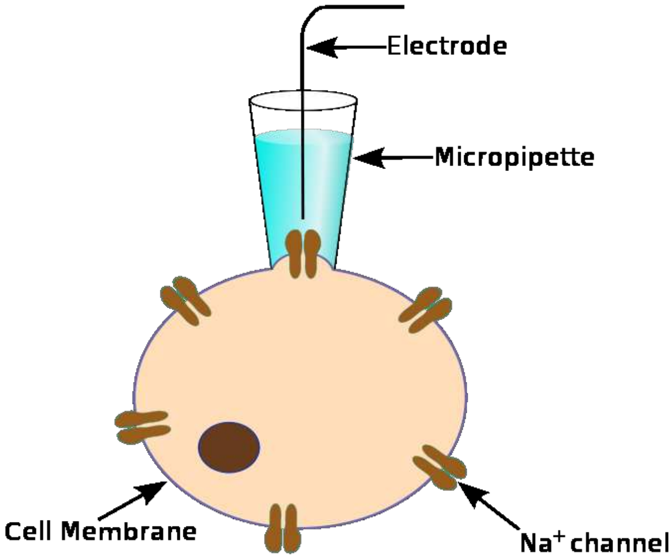

Figure 4.7: Diagram of patch-clamp setup which is a typical measurement of the electric potential across an axonal membrane. [Adapted from http://upload.wikimedia.org/wikipedia/en/2/20/Patch_clamp.svg]

open ion channels in the whole cells change statistically. Therefore, the fluctuations arising from the number of open gates of the potassium and sodium channels should be taken into account. The fluctuations which are the so-called channel noises play an important role in the dynamics of action potential generation. Usually, the noisy gating of ion channels is modeled by Markovian chemical reaction schemes with a certain number of states and voltage-dependent transition rates. Other modeling approaches with non-Markovian schemes allow the transition rates depend on both voltage and the amount of time that each channel spent in a given state [129]. It is notable that, the traditional description of channel noise is quantifiable under voltage-clamp conditions [33, 128, 130].

Channel noise is not the only source that affects the neuronal dynamics and influences the signal transmission in neurons. There are other sources, such as synaptic noise, which is a major source of neuronal variability. Noise from synaptic process is more complex than channel noise, as it arises from multiple sources. The precise impact of synaptic noise can be evaluated only when the channel noise can be understood and quantified. Therefore, we first study the channel noise without involving other sources of noise [130].

Patch clamp

In recent years, the patch clamp technique has greatly enhanced the speed of research on the single ion channels in cells. It offers a method to record the current flowing through the single ion channels. In 1976, Erwin Neher and Bert Sakmann developed the patch-clamp technique which can measure the current flowing through an individual ion channel [127, 128]. The principle of their technique is to isolate a patch of membrane electrically from the external solution, and then record the current through this patch. This is achieved by pressing a polished glass pipette, which is filled with a suitable electrolyte solution, to against the surface of a cell (Fig. 4.7). Applying light suction, a seal is formed. If the sealed area is small enough and the channel density is low enough, only one active ion channel is contained in the sealed membrane patch. Therefore, the opening and closing of this single ion channel can be observed directly by recording the current. For this big contribution to the development of the technique, Neher and Sakmann received the *Noble Prize in Physiology or Medicine.*

From the experiment recordings, they found that all the ion channels open and close abruptly and randomly. In other words, the opening (or closing) probability is controlled by the transmembrane voltage. The sum of all the channels of the same type gives rise to the macroscopic current, such as sodium current I_{Na} or potassium current I_{K}. The experimental recordings of these current exhibit the similar waveforms as those from the Hodgkin-Huxley model [117] with a large number of ion channels.

Quantifying channel noise

The essence of the voltage-gated channels is the fact that their probabilistic gating allow the ions transport through the cell membrane. For a clamped cell membrane patch with a total number N of ion channels, the electrical current I based on the flux of ions, can be described by

$$I = \gamma N^{open} \left(V - E_S\right) . \tag{4.17}$$

Here γ is the open-channel conductance, N^{open} is the number of open ion channels, V and E_S keep the same meaning as defined in Section 4.1: membrane potential and reversal potential, respectively. The mean $\overline{N^{open}}$ and variance σ^2 of the number of the open ion channels read,

$$\overline{N^{open}} = Np(V), \tag{4.18a}$$

$$\sigma^2 = Np(V)\left(1 - p(V)\right). \tag{4.18b}$$

Here $p(V)$ is the voltage dependent probability for a single channel to be open. A useful parameter to quantity the noisiness is the coefficient of variation (CV), which measures the relative deviation from the mean value. It has the form

$$CV := \frac{\sigma}{\overline{N^{open}}} = \sqrt{\frac{1}{N}\frac{1-p(V)}{p(V)}} . \tag{4.19}$$

The influence of the fluctuations around the mean value declines as the number of ion channels increasing. CV is proportional to the square root of the number of channels $N^{-1/2}$, which implies that the noise influence can be neglected in the case of very large numbers of ion channels. The noise strength is determined by the total number of ion channels in a membrane patch (Fig. 4.8). The total number of channels can be calculated via the densities of the channels:

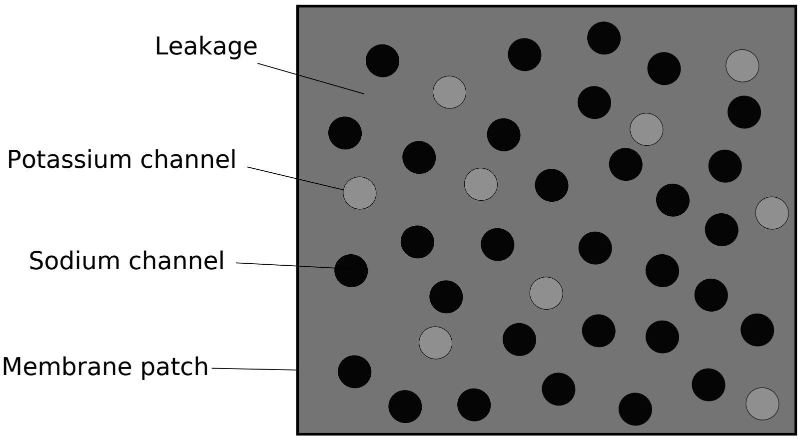

Figure 4.8: Sketch of a cell membrane patch of a squid giant axon with finite size. The circles denote the potassium and sodium channels. The leakage current appeared in the Hodgkin-Huxley model is plotted as the grey background.

$$N_{\mathrm{K}} = \rho_{\mathrm{K}}\mathcal{A}, \tag{4.20a}$$

$$N_{\mathrm{Na}} = \rho_{\mathrm{Na}}\mathcal{A}\,. \tag{4.20b}$$

$\mathcal{A}$ is the area of the membrane patch, ρ_{K} and ρ_{Na} are the densities which are assumed to be constant. However, this is not guaranteed for all biological membranes, e.g. in nodes of Ranvier where ion channels are accumulated while nearly none channel exists in the inter space.

It is worth mentioning, that the experiments done by Hodgkin and Huxley were carried out under the condition of huge numbers of ion channels. Therefore, the noise was neglected in the original Hodgkin-Huxley model.

Langevin-type description of channel noise

According to the experimental data, Hodgkin and Huxley proposed the gate modeling to study the generation of action potentials (c.p. Section 4.1.2). The potassium ion channel is built up with four identical gates with indistinguishable kinetics. The gates switch independently between "closed" and "open" to form different configurations. Since the potassium channel includes four identical gates, there are five configurations. It turns out that only in the configuration that all the four gates open, the ion channel contributes to the conductance. For this reason, the exponent four appearers in Eq. (4.9). Therefore, the potassium conductance can be described as,

$$g_{\mathrm{K}} = n^4 g_{\mathrm{K}}^{\max} = n_1 n_2 n_3 n_4 g_{\mathrm{K}}^{\max}, \tag{4.21a}$$

$$\frac{\mathrm{d}n_j}{\mathrm{d}t} = \alpha_n(V)(1-n_j) - \beta_n(V)n_j\,, \quad \text{for } j = 1, ..., 4. \tag{4.21b}$$

Here, $\alpha_n(V)$ and $\beta_n(V)$ are the transition rates for potassium channels from one configuration to another.

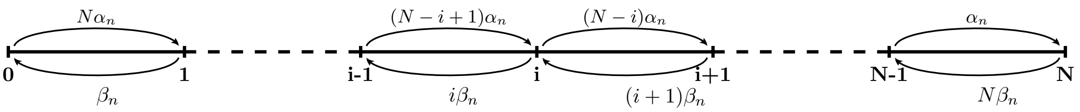

Figure 4.9: Evolution of the number of conducting channels. It is a one-step process for N channels.

Since the single potassium channel is built up with four gate-elements, 4 two-state elements (gates) are considered. The channel is considered conducting only in the configuration that all the four gates are open, otherwise it is nonconducting. The total conductance is the sum of all the conducting channels [131]. Instead of considering the details of gates variables, we are more interested in the probability to find a certain configuration that all the four gates are open to form a conducting channel. Here, we use $P(\mathcal{N}, t)$ to denote the probability with $\mathcal{N}$ conducting channels at time t. Naturally, the probability transition is given by the transition rates $(\alpha_n(V), \beta_n(V))$ times the number $\mathcal{N}$ of the conducting channels. For a total number N_{K} of the potassium ion channels, which means there are $(N_{\mathrm{K}}+1)$ states (c.p. Fig. 4.9). The probability $P(\mathcal{N}, t)$ satisfies a linear one-step process with a master equation

$$\begin{aligned}\frac{\mathrm{d}P(\mathcal{N},t)}{\mathrm{d}t} = \alpha_n(N_{\mathrm{K}}-\mathcal{N}+1)P(\mathcal{N}-1,t) &+ \beta_n(\mathcal{N}+1)P(\mathcal{N}+1,t) \\ &- [\alpha_n(N_{\mathrm{K}}-\mathcal{N})+\beta_n\mathcal{N}]P(\mathcal{N},t)\,, \quad (4.22a)\end{aligned}$$

with $\mathcal{N} = 1, ..., N_{\mathrm{K}}-1$, and the boundary conditions ($\mathcal{N}=0$ and $\mathcal{N}=N_{\mathrm{K}}$) read,

$$\frac{\mathrm{d}P(0,t)}{\mathrm{d}t} = \beta_n P(1,t) - \alpha_n N_{\mathrm{K}} P(0,t), \tag{4.22b}$$

$$\frac{\mathrm{d}P(N_{\mathrm{K}},t)}{\mathrm{d}t} = \alpha_n P(N_{\mathrm{K}}-1,t) - \beta_n N_{\mathrm{K}} P(N_{\mathrm{K}},t). \tag{4.22c}$$

For sufficiently large numbers of potassium ion channels N_{K}, a Fokker-Planck equation can be derived approximately from the master equation Eq. (4.22). With $n = \mathcal{N}/N_{\mathrm{K}}$ and $P(n,t) = P(\mathcal{N},t)/N_{\mathrm{K}}$, the Fokker-Planck equation can be written as

$$\frac{\partial P(n,t)}{\partial t} = -\frac{\partial}{\partial n}[\alpha_n(1-n)-\beta_n n]P(n,t) + \frac{\partial^2}{\partial n^2}[\frac{(1-n)\alpha_n + n\beta_n}{2N_{\mathrm{k}}}]P(n,t)\,. \tag{4.23}$$

The probability flow vanishes at $n=0$ and $n=1$ as the reflecting boundaries conditions. It means

$$[\alpha_n(1-n)-\beta_n n]P(n,t) - \frac{\partial}{\partial n}[\frac{(1-n)\alpha_n+n\beta_n}{2N_{\mathrm{K}}}] = 0\,. \tag{4.24}$$

The associated Langevin description which is an ordinary differential equation including stochastic term, is much easier to be realized by numerical simulations [131]. The corresponding Langevin description interpreted in Itô-sense is [132],

$$\frac{\mathrm{d}n(t)}{\mathrm{d}t} = \alpha_n(V)(1-n) - \beta_n(V)n + \sqrt{\frac{(1-n)\alpha_n+n\beta_n}{N_{\mathrm{K}}}}\xi_n(t). \tag{4.25}$$

Here, $\xi_n(t)$ denotes Gaussian white noise sources with vanishing mean and delta-auto-correlations.

As described in Section 4.1.2, the situation for sodium channel is more complicated. It involves two processes (activation and inactivation), and two different types of gates. Experimental recordings show that the sodium channel is built up with three identical activation gates and a single inactivation gate. By a similar derivation, the following Langevin equations for gating variables m and h are obtained:

$$\frac{\mathrm{d}m(t)}{\mathrm{d}t} = \alpha_m(V)(1-m) - \beta_m(V)m + \sqrt{\frac{(1-m)\alpha_m + m\beta_m}{N_{\mathrm{Na}}}}\xi_m(t), \tag{4.26a}$$

$$\frac{\mathrm{d}h(t)}{\mathrm{d}t} = \alpha_h(V)(1-h) - \beta_h(V)h + \sqrt{\frac{(1-h)\alpha_h + h\beta_h}{N_{\mathrm{Na}}}}\xi_h(t), \tag{4.26b}$$

where $\xi_m(t)$ and $\xi_h(t)$ are still Gaussian white noise variables. All these three channel noise sources $\xi_n(t)$, $\xi_m(t)$ and $\xi_h(t)$ are statistically independent and with the auto-correlation function as,

$$\langle \xi_i(t)\xi_j(t')\rangle = \delta_{ij}\delta(t-t')\,, \tag{4.27}$$

where $i, j = m$, h and n.

In the limit of infinite numbers of ion channels, the above set of Langevin equations for the gating variables, i.e. Eq. (4.25) and (4.26) can be simplified to the deterministic set, Eq. (4.6) proposed originally by Hodgkin and Huxley. Thus, the Langevin description serves as an extension of the original Hodgkin-Huxley model which takes the channel noise into account. The strengths of the channel noise are thereby given as,

$$D_n := \frac{(1-n)\alpha_n + n\beta_n}{2N_{\mathrm{K}}}\,, \tag{4.28a}$$

$$D_m := \frac{(1-m)\alpha_m + m\beta_m}{2N_{\mathrm{Na}}}\,, \tag{4.28b}$$

$$D_h := \frac{(1-h)\alpha_h + h\beta_h}{2N_{\mathrm{Na}}}. \tag{4.28c}$$

The strength of the channel noise is indirectly proportional to the total numbers of potassium and sodium ion channels, which are determined by the area of the membrane patch and the channel densities. Throughout our work, all the ion channel densities are kept to 18 for potassium and 60 for the sodium channels per $\mu\mathrm{m}^2$, following the original Hodgkin-Huxley model [28].

All the parameters in our numerical simulations are listed in Table 4.1. They are typical values consistent with the original Hodgkin-Huxley model [28].

Characteristics

To study the significant effect of channel noise, we integrate Eq. (4.14) numerically with the stochastic gating variables Eqs. (4.25) and (4.26). The Box-Muller algo-

Table 4.1: Hodgkin-Huxley parameters

Membrane capacitance per unit area	C_m	=	1	μF/cm^2
Reversal potential for Na current	E_{Na}	=	50	mV
Reversal potential for K current	E_{K}	=	-77	mV
Reversal potential for leakage current	E_{L}	=	-54.4	mV
Leakage conductance per unit area	G_L	=	0.3	mS/cm^2
Maximum Na conductance per unit area	$g_{\mathrm{Na}}^{\mathrm{max}}$	=	120	mS/cm^2
Maximum K conductance per unit area	$g_{\mathrm{K}}^{\mathrm{max}}$	=	36	mS/cm^2
Node area	$\mathcal{A}$	varying		[μm^2]
Na channel density	ρ_{Na}	=	60	μm^{-2}
K channel density	ρ_{K}	=	18	μm^{-2}
Number of Na channels	N_{Na}	=	$\rho_{\mathrm{Na}}\,\mathcal{A}$	
Number of K channels	N_{K}	=	$\rho_{\mathrm{K}}\,\mathcal{A}$	
Rest Voltage	E_S	=	-65	mV
Inactivation probability for the Na gate at rest	h_i	=	0.596	
Activation probability for the Na gate at rest	m_i	=	0.053	
Activation probability for the K gate at rest	n_i	=	0.318	

rithm is used to generate the Gaussian distributed noise [133]. More details can be found in Appendix A.2.

As we have mentioned before, the electric signals which carry the information process of the nerve cell, are series of action potentials. We can study the stochastic signals by means of occurrences of action potentials. To detect the occurrences of action potentials from the simulation of the membrane potential dynamics, we define a specific threshold barrier. In particular, whenever the membrane potential $V(t)$ exceeds the value of 0 mV, the occurrence of an action potential is assigned. It turns out that such determined spike occurrences depend only weakly on the actual choice of the threshold value $V_0 = 0\,\mathrm{mV}$ [134]. The action potentials can be recorded as point process (c.p. Appendix A.2).

For the deterministic Hodgkin-Huxley neuron system, which is the limit condition as the membrane patch increases to infinite i.e. $N_{\mathrm{Na}} \to \infty$ and $N_{\mathrm{K}} \to \infty$, action potential occurs only under an external current stimulus. Periodic spikes are observed unless the stimulus is big enough, see Fig. 4.10 (a).

Much richer behaviors of the spike trains begin to appear when the channel noise is considered. As the noise strength increases, which means decreasing the size of membrane patch, the production of spikes would increase without any additional stimulus. Fig. 4.10 gives an example for a typical voltage signal with different patch sizes. They are obtained from simulations of the stochastic Hodgkin-Huxley equation Eq. (4.14) with stochastic gating variables Eq. (4.25) and (4.26). As the size of membrane patch increases, c.f. the noise strength decreases, fewer spontaneous spikes are pronounced.

From the definition of the occurrences of spikes, we can record the spike occurrences at t_i, and define the interspike interval T_i (see the middle panel in Fig. 4.10) as,

$$T_i = t_{i+1} - t_i\,, \tag{4.29}$$

with $i = 1, 2, ..., N$, and N denotes the total number of spikes obtained from the

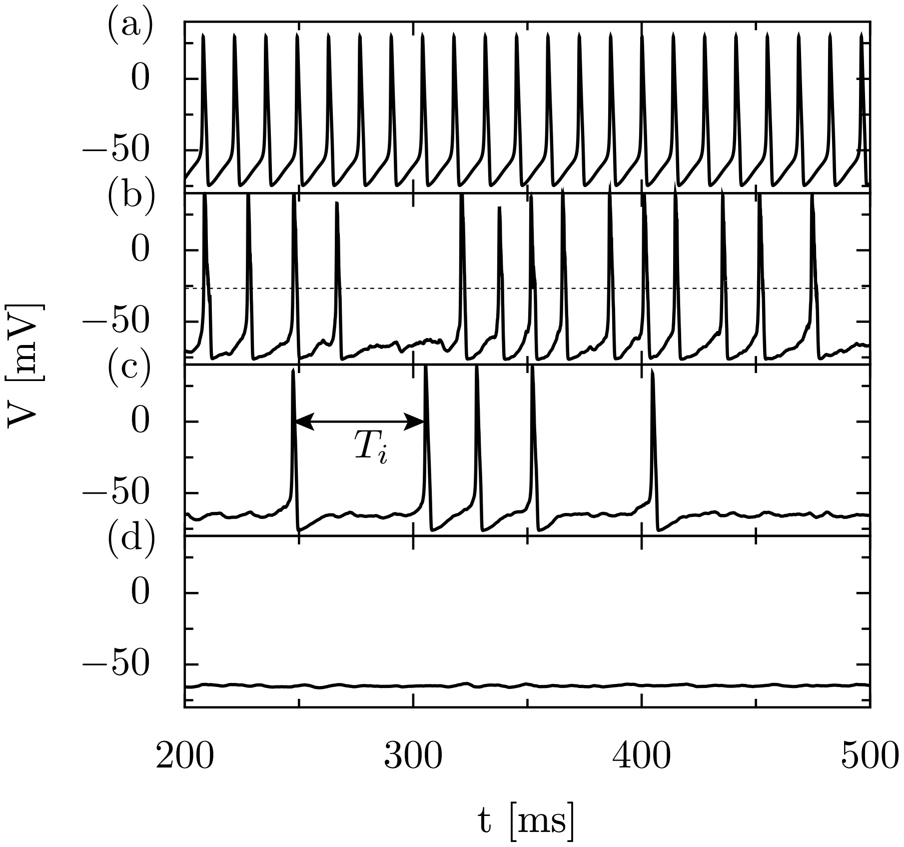

Figure 4.10: Spiking trains versus time. (a) In the deterministic condition with external current $I_{ext} = 12\,\mu\mathrm{A/cm}^2$ (b)- (d) Typical spiking trains for different channel numbers, with $N_{\mathrm{K}} = 30, 300, 3000$ for (b), (c) and (d), respectively. When the noise strength increases as the channel numbers decreases, more spontaneous spikes are produced. In the panel (b), a certain detection barrier $V_0 = 0\,\mathrm{mV}$ which determines the occurrences of spikes is labeled as dash line. The interspike interval T_i is marked in the panel (c).

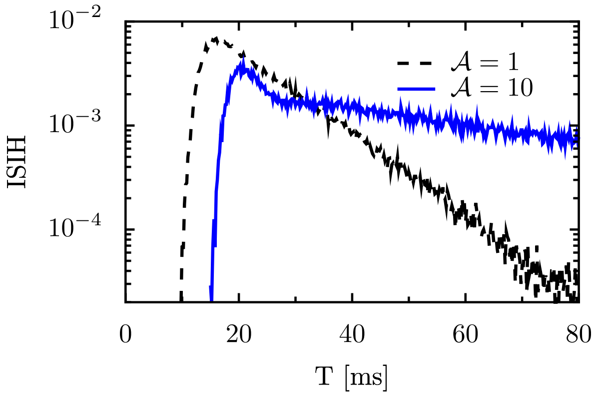

Figure 4.11: Interspike interval histograms (ISIH) versus the interspike interval T of the stochastic Hodgkin-Huxley model at different noise level, as indicated in the figure in units of μm^2. The membrane sizes are 1 and 10 μm^2, respectively.

individual numerical simulation. Based on the interspike interval T_i, two important characteristics, i.e. (normalized) interspike interval histograms (ISIH) and the mean interspike interval $\langle T \rangle$ can be obtained.

The (normalized) interspike interval histograms (ISIH), which describes the distribution of the interspike intervals, are obtained with a bin width of 0.2 ms, and normalized with the total number of spikes. The interspike interval histograms (ISIH) are plotted in Fig. 4.11 for different noise strengths. The most attractive feature is that there exists a peak. The interspike interval at the position of this peak is the most concentrate interval. The interspike interval which stays at the position of the peak, is referred to as internal time scale $\mathcal{T}_{\text{int}}$. It depends on the noise level. Remarkably, not only the value of the internal time scale $\mathcal{T}_{\text{int}}$, but also the height of the histograms, change with noise. There is no spike within the refractory time which also depends on the noise. Moreover, for the large time intervals, the interspike interval histograms (ISIH) decay exponentially.

The mean interspike interval $\langle T \rangle$ is calculated by

$$\langle T \rangle = \frac{1}{N} \sum_{i=1}^{N} T_i \,. \tag{4.30}$$

As found in Fig. 4.10, more action potentials are produced by increasing channel noise, which helps to overcome the barrier. Therefore, the mean interspike interval $\langle T \rangle$ decreases as noise increases, Fig. 4.12. Some approximate theoretical analysis of the stochastic Hodgkin-Huxley model have been done by Chow and White [135]. They assumed that the spontaneous action potentials are analogous to the escape process that the particle crosses a potential barrier. With Kramers' escape rate, they estimate the probability density function of the interspike intervals, and obtained an analytical result of the escape rate, reading [135],

$$R \sim 45 \exp\left[-N_{\text{K}}/1332\right] \text{s}^{-1} \,. \tag{4.31}$$

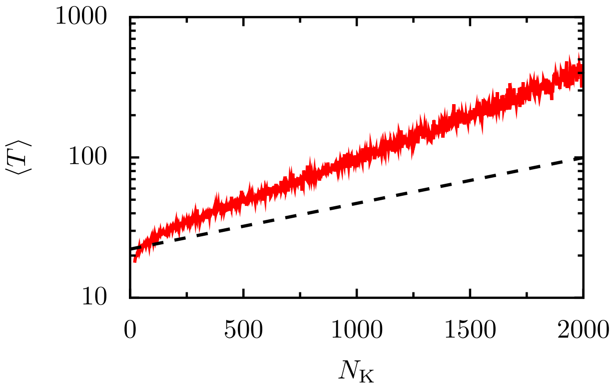

Figure 4.12: The dependence of mean interspike interval $\langle T\rangle$ versus the number of potassium $N_{\rm K}$. The red solid line is from the numerical simulation. The black dash line is analytical result from Eq. (4.31).

It implies that the mean interspike interval decays exponentially with increasing the number of ion channels. The mean interspike interval as the function of the number of ion channels is plotted in Fig. 4.12.

There are other measurements, such as Fano factor to measure the variability of the counting process, spectrum, serial correlation coefficient (SCC) to characterize correlations between ISIs, coefficient of variation (CV) which is the ratio of the standard deviation to the mean value of the ISIs [136, 137].

4.2 Spontaneous spiking in presence of delayed feedback

In Section 4.1, we have introduced the Hodgkin-Huxley model to describe the generation of action potentials. The main properties of the dynamics are presented. This section is dedicated to the extension to a stochastic Hodgkin-Huxley model with delayed feedback based on the so-called autapse phenomenon that a single neuron with a synapse onto its own dendrites. This extension combines both the effect of intrinsic channel noise and the delayed feedback of the dynamic response of autapse. This biophysical phenomenon can be modeled by a stochastic Hodgkin-Huxley model with a delayed stimulus. The influence of the delayed stimulus can be systematically investigated by introducing a Pyragas-like delayed term exhibiting a coupling parameter and a delay time. Similar to last sub-section, the behavior is analyzed in terms of the interspike interval histograms (ISIH) and the average interspike interval $\langle T\rangle$. It is found that the delayed feedback manifests itself in the occurrence of bursting and a rich multimodal interspike interval distribution. The delayed feedback brings a new time scale into the system, and induces reduction of the spontaneous spiking activity at characteristic frequencies. A specific frequency-locking mechanism is observed for the mean interspike interval. The further understanding of our work is studied by comparing with the well-known Kuramoto dynamics.

4.2.1 Model setup

Time-delayed feedback is a common mechanism relevant in many biological systems including excitable gene regulatory circuits [138] and human balance [139]. It has been investigated not only in biological systems, but also in a wider area: This includes but is not limited to semiconductor superlattices [140], chemical oscillators (CO oxidation on platinum) [141] and photosensitive Oregonator models [142]. It has been found that the delayed feedback loops may dramatically change the dynamical behavior of the system. It is shown that delayed feedback presents to be an efficient method to control chaos or turbulence by stabilizing the unstable periodic orbits (UPOs) embedded in the chaotic attractor [143], stabilize periodic orbits [141], or to control the coherence resonance [140, 144, 145].

During the early studies of the propagation of neuron's electrical signals along the axons, neurobiologists have found that the dendrites are connected not only to their neighbors', but also to the same neuron's dendrites [146–149]. These auto-synapses are referred to as autapses, which were first proposed by Van der Loos and Glaser in 1972 [31]. In their experiment of pyramidal neurons in the adult rabbit visual cortex, they found such synaptic arrangements between axon collaterals and branches of basal dendrites, stained by the Golgi method [31]. Since then, the existence of autapses has been well established in numerous types of cells for different species, such as human, rabbit, dog, rat cerebral cortex, cat spinal cord, substantia nigra, and monkey neostriatum [146, 150–152]. Moreover, the autapses were found in about 80% of all neurons being analyzed so far, including neurons of the human brain [153]. They are not so many existing on pyramidal cells, but more frequently found in two subclasses of cortical inhibitory interneurons. For this reason, they must play a functional one. Experimental evidence has been found that it plays an important role in the process of coding and processing of information in the brain for a variety of neural systems. It was established that delayed feedback can induce bursting [145]. However, what functional significance they can offer and the mechanisms of the new phenomenon in the neural systems are still not fully understood.

Most autapses are located within $100\,\mu$m from the soma, but a few are located almost $500\,\mu$m away [153]. Their location on the dendritic tree is also variable. Most of them tend to form at specific dendritic locations, in particular second- or third-order dendrites. The mean length of the autaptic loop is around 272 μm (range 120-477 μm) [31]. The delay time of the autapses exhibits a broad range, ranging from a few milliseconds to tenths of milliseconds [31, 154]. Since the refractory time of the neuron dynamics is around 15 ms, the effect of the delay time which comes from the propagation of action potentials along the axons, can no longer be neglected, and their chemical transmission through synapses should also be taken into account.

This time-delayed feedback mechanism in autapse (sketched in Fig. 4.13) can be formulated mathematically as a delayed stimulus with a Pyragas type [155]. Within this formulation, the autaptic delayed stimulus $I_\tau(t)$ should be proportional to the difference of the membrane potential at time t and that at an earlier time $t-\tau$,

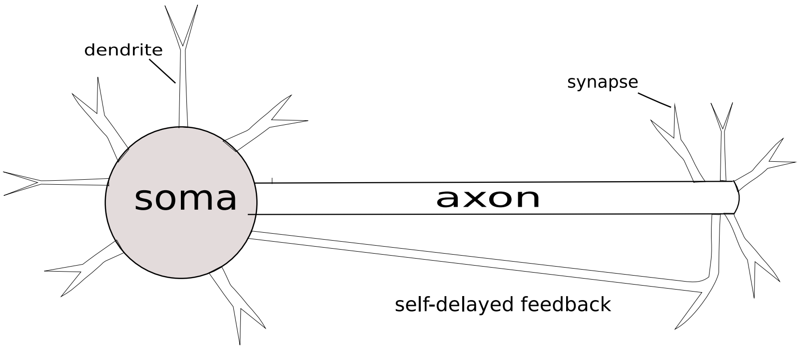

Figure 4.13: Sketch of a neuronal cell exhibiting a self delayed feedback mechanism, i.e. autapse [115].

reading,

$$I_\tau(t) = \epsilon \left[V(t-\tau) - V(t)\right] . \tag{4.32}$$

Here, ϵ corresponds to the coupling strength of the autapse mechanism and τ is referred to as the specific finite delay time. The delay time arising from the autaptic loop is due to a finite signal propagation distance and speed. $V(t-\tau)$ is the membrane potential at the earlier time $t-\tau$.

The autaptic delayed stimulus expressed by Eq. (4.32) represents an excitatory coupling mechanism, in which a presynaptic stimulus generated by a spike at an earlier time $t-\tau$ evokes a postsynaptic event at time t. We note that the ansatz for the delayed self-stimulus corresponds to the electrotonic interaction. We consider an idealized situation wherein the autaptic delayed stimulus is proportional to the difference of the pre- and post-synaptic membrane potentials. Although autapses are typically formed by chemical synapses, our idealized modeling simplifies the complex biophysical temporal evolution of the synaptic conductance with a constant coupling strength ϵ.

Based on the Hodgkin-Huxley model with intrinsic noise and synaptic stimulus, the autapse model can be mathematically described as follows,

$$\begin{aligned} C_m \frac{\mathrm{d}V(t)}{\mathrm{d}t} = &- n^4(t) g_{\mathrm{K}}^{\max} \left(V(t) - E_{\mathrm{K}}\right) - g_{\mathrm{L}} \left(V(t) - E_{\mathrm{L}}\right) \\ &- m^3(t) h(t) g_{\mathrm{Na}}^{\max} \left(V(t) - E_{\mathrm{Na}}\right) + I_\tau(t) . \end{aligned} \tag{4.33}$$

Note that, the dynamics of the gating variables $n(t)$, $m(t)$ and $h(t)$ are described by stochastic equations, i.e. Eq. (4.25) and Eq. (4.26). All the parameters retain the same meaning and expressions as in the previous sections. The typical values of the parameters are listed in Table 4.1 in Section 4.1.3. In our numerical simulation of this modified Hodgkin-Huxley equation Eq. (4.33), an integration step $\Delta t = 0.002\,\mathrm{ms}$ is kept, and Box-Muller algorithm is used to generate Gaussian distributed random numbers, which influence the gating variables m, n, h (c.p. Appendix. A.2).

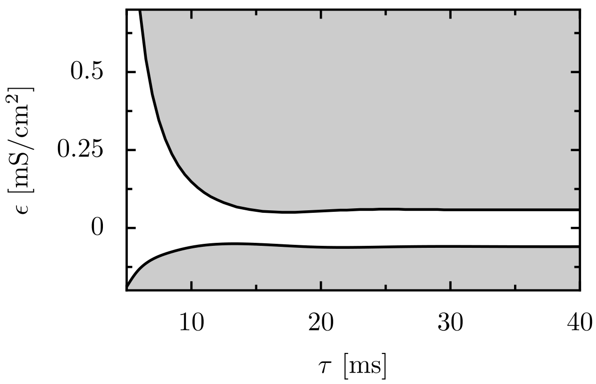

Figure 4.14: The phase diagram of repetitive firing in the $\epsilon - \tau$ phase space for the Hodgkin-Huxley model with a delayed coupling term where ϵ denotes the coupling strength and τ denotes the delayed time [115]. The gray areas give the parameter regime for which repetitive firing is observed. The two black solid lines indicate the boundaries of critical coupling strength ϵ_c versus the delay time τ at which the behavior changes from the rest state to a repetitive firing.

4.2.2 Deterministic dynamics

In Section 4.1.2, we have introduced the original Hodgkin-Huxley model which is described by the Eq. (4.14) in absence of both delayed feedback ($\epsilon = 0$) and noise ($N_{\mathrm{Na}} \to \infty$ and $N_{\mathrm{K}} \to \infty$). There is a single stable fixed point which is the rest state with the rest potential $E_S \approx -65\,\mathrm{mV}$. Any temporary disturbance can make the system to overcome the threshold for excitation and then relax back to the rest state. It results in the generation of spikes. Note that with a proper choice of the initial condition which is above the threshold potential, a single action potential may occur before the system relaxes to the rest state [120].

In presence of the autaptic delayed coupling, the stable fixed point solution still exists while a stable oscillatory solution emerges as the delay time τ increases. It means that, repetitive (tonic) spiking occurs. We systematically study the deterministic dynamics of Autapse. For an initial potential larger than the rest potential, we record the parameters (coupling strength ϵ and delay time τ) when the first occurrence of repetitive firing can be observed. In doing so, the resulting phase diagram with positive and negative critical coupling strength $\epsilon_c^+(\tau)$ and $\epsilon_c^-(\tau)$ are obtained, see Fig. 4.14. The black solid lines represent the critical coupling for positive and negative strength $\epsilon_c^+(\tau)$ and $\epsilon_c^-(\tau)$, respectively.

The coupling strength ϵ in the range $\epsilon_c^-(\tau) < \epsilon < \epsilon_c^+(\tau)$ (the white region in Fig. 4.14) is called subthreshold coupling strength, while others ($\epsilon > \epsilon_c^+(\tau)$ or $\epsilon < \epsilon_c^-(\tau)$, i.e. the gray regions in Fig. 4.14) are referred to as suprathreshold coupling strength. For the subthreshold case, any excitation simply decays and the system relaxes to the rest state. For suprathreshold coupling, periodic spikes representing repetitive firing can be observed. From the phase diagram, it is clear to see that the modulus of the critical coupling strength decreases drastically as the delayed time τ increases for short delay times, and remains constant for large delay times. That is because the system needs time for spiking and returning to the rest state, which is related to the so-called *relative refractory period* mentioned in Section 4.1.2. We call it refractory time for short. Usually, it is around 12 ms. For the delay time shorter than the refractory time interval, the neuron is rather insensitive to any stimulus. Therefore, a stronger coupling strength is needed in order to excite the system to obtain repetitive firing. Due to this fact, it is called *undershoot phase* where the neuron is rather insensitive to any stimuli. In case of delay times larger than the refractory time, the value of the critical coupling strength saturates. For longer delay times, more than one spike may fit into time interval given by τ. Consequently, doublets, triplets and multiplets may appear. We should point out here that the positive and negative coupling strengths $\epsilon_c^+(\tau)$ and $\epsilon_c^-(\tau)$ are not symmetrical.

Below, we study the delayed dynamics in the regime of large delay times, in which the critical coupling strength is $0.059\,\mathrm{mS/cm^2}$. Some examples are shown for the stochastic Hodgkin-Huxley model with delayed feedback where we have chosen $\tau = 30\,\mathrm{ms}$.

4.2.3 Stochastic dynamics of the Hodgkin-Huxley model with delayed feedback

In Section 4.1.3, we have found that channel noise can induce spontaneous spikes. Here, we will discuss the influence of the channel noise on this observed repetitive firing dynamics. In principle, the influence of channel noise could be sought to be twofold: (i) One of the main differences to the deterministic delayed feedback coupling scheme is the occurrence of the so-called bursting which is the spikes repeating themselves via the delayed coupling mechanism, (see Fig. 4.15). (ii) Channel noise can also lead to skipping of spikes, which are generated in the deterministic dynamics [156].

In Fig. 4.15 the simulated membrane potential $V(t)$ is depicted with an exemplarily chosen noise level for the two cases, namely in panel (a) without delay coupling ($\epsilon = 0$) and in panel (b) with a finite delay coupling ($\epsilon = 0.08\mathrm{mS/cm^2}$). In absence of delayed coupling (Fig. 4.15 (a)), spontaneous spiking is observed, i.e. noise induced action potentials occur irregularly. Meanwhile, in presence of finite delay-coupling ϵ (Fig. 4.15 (b)), a regular spike pattern which is referred to as bursting is observed.

In order to illustrate the behavior more quantitatively, we integrate the equations of the stochastic Hodgkin-Huxley model with delayed feedback coupling, i.e. Eq. (4.33), and study the (normalized) interspike interval histograms (ISIH) and the mean interspike interval $\langle T \rangle$.

First of all, we study the distribution of the interspike intervals (ISIH) at fixed channel noise strengths, which is depicted in Fig. 4.16. For large time intervals, the distribution decays exponentially for all coupling strengths. Small time intervals are suppressed because of the neuron's refractory time. For the situation $\epsilon = 0$ (c.f. Section 4.1.3), the ISIH exhibits one broad maximum located around the internal time scale $\mathcal{T}_{\mathrm{int}}$, which systematically diminishes with increasing noise level [134, 157]. The minimal time scale for undistorted spikes is around the refractory time ($\approx 12\,\mathrm{ms}$). In presence of noise or finite feedback coupling, the neuron returns to its fixed-point with nonvanishing probability. Therefore, some behaviors are still kept, i.e. the peak at the intrinsic time scale $\mathcal{T}_{\mathrm{int}}$ and exponential decaying are still

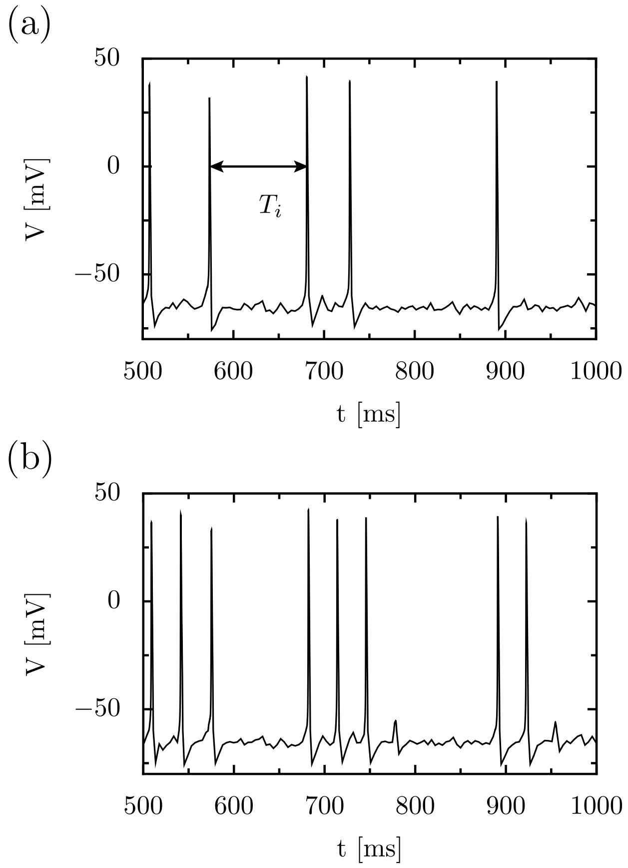

Figure 4.15: Simulated spike-trains: (a) Membrane potential $V(t)$ for the stochastic Hodgkin-Huxley model in absence of feedback, i.e. with $\epsilon = 0$ versus time t; (b) $V(t)$ versus time t in presence of finite feedback with strength $\epsilon = 0.08 \text{mS/cm}^2$ exhibiting repetitive spiking for a chosen delay time $\tau = 30\,\text{ms}$. For both simulations, the number of potassium ion channels is set to $N_\text{K} = 150$ and that of the sodium ion channels is $N_\text{Na} = 500$. The spontaneous, i.e. noise induced, action potentials exhibit a bursting-like behavior in case of the delayed coupling (b).

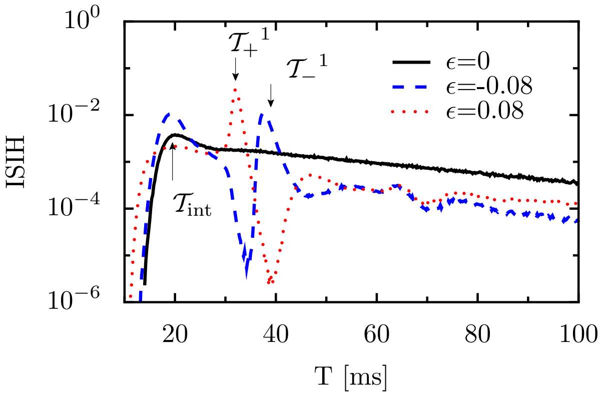

Figure 4.16: Interspike interval histograms (ISIH) versus the interspike interval T of the stochastic Hodgkin-Huxley model with a delay coupling mechanism at different coupling strengths ϵ, as indicated in the figure in units of mS/cm^2. The bin width for T has been chosen throughout this work at 0.2 ms. The chosen number of potassium ion channels is $N_\text{K} = 150$, while the number of sodium ion channels is set at $N_\text{Na} = 500$. The delay time τ is fixed at 30 ms.

detected for different noise strengths in the ISIH in Fig. 4.16.

However, the ISIHs become multimodal in presence of delayed feedback, i.e. for $\epsilon \neq 0$. Several maxima occur at larger time intervals and a number of deep dips are observed in between. We use ${\mathcal{T}_+}^1$ and ${\mathcal{T}_-}^1$ to denote the positions of the first peaks induced by delayed feedback for positive and negative coupling strength, respectively. As far as the system is excited, an activation time $\mathcal{T}_{\text{act}}$ is necessarily needed to response to the delayed stimulus and create the next spike. Therefore, the ${\mathcal{T}_+}^1$ and ${\mathcal{T}_-}^1$ do not equal to the delay time τ, but equal to the sum of delay time and the activation time $\mathcal{T}_{\text{act}}$. In fact, ${\mathcal{T}_+}^1 \simeq \tau + 2$ ms and ${\mathcal{T}_-}^1 \simeq \tau + 9$ ms which are practically not changing with coupling strengths ϵ. In principle, other maxima occurring at $\mathcal{T}^i$ are linear combinations of these two time scales $\mathcal{T}_{\text{int}}$ and ${\mathcal{T}_\pm}^1$. They are written as

$$\mathcal{T}^i = N_0 \mathcal{T}_{\text{int}} + N_1 \mathcal{T}_\pm^1 \,, \tag{4.34}$$

where, N_0 and N_1 are natural numbers. Such forms of the distributions of the ISIH are indicators of an enhanced coherence [157, 158].

The comparison of the distribution for $\epsilon = 0.08\,\text{mS/cm}^2$ and $\epsilon = -0.08\,\text{mS/cm}^2$ highlights another remarkable phenomena. When delayed coupling is applied to the neuronal dynamics, surely, the delay time gives support to those time scales which are related to the delay time. But in addition, there is suppression of certain time scales, c.f. the deep dips in Fig. 4.16. For example, for positive ϵ the system favors frequencies associated to the time ${\mathcal{T}_+}^1$ and suppresses frequencies slightly smaller than those. The concentrated distribution of the ISIH is an indication of enhanced coherence [158] and synchronization [144, 159]. Similarly, in case of a negative coupling parameter ϵ, a preferential time ${\mathcal{T}_-}^1$ is observed. However, due to the complex dynamics in the Hodgkin-Huxley system, the suppressed time scale is in this case smaller than ${\mathcal{T}_-}^1$ and incidentally coincidences with the time ${\mathcal{T}_+}^1$. It means the position of the maximum for positive coupling strength is the minimum position for negative coupling strength, c.f. Fig. 4.16. This provides a good method for adjusting the concentrated distribution, which is important for the memory storage [160] and stimulus-locked short-term dynamics [7].

In the following, we will focus on the positive coupling strength $\epsilon > 0$. The activation time $\mathcal{T}_{\text{act}}$ is around 2 ms. For convenience, the delay time induced time scale ${\mathcal{T}_+}^1$ is termed $\mathcal{T}_\tau$ and the critical coupling strength for repetitive firing ϵ_c^+ is simplified as ϵ_c. For larger coupling $\epsilon > \epsilon_c(\tau)$, an action potential induces repetitive firing which is named as *suprathreshold delay coupling regime.* For the case of lower coupling strength i.e. $\epsilon < \epsilon_c(\tau)$, the neuron's dynamics is excitable and noise is needed to support the repetition of an action potential addressed as *subthreshold delay coupling regime.* More details of the behaviors in both conditions will be introduced in the following sections. Remarkably, we find an overall similar behavior that differs, however, quantitatively for negative coupling $\epsilon < 0$ (not shown).

Subthreshold delay coupling: $\epsilon < \epsilon_c(\tau)$

In the case of subthreshold coupling strength, the noise-induced spiking results in a broad distribution with exponentially decaying tail. As the non-vanishing delayed

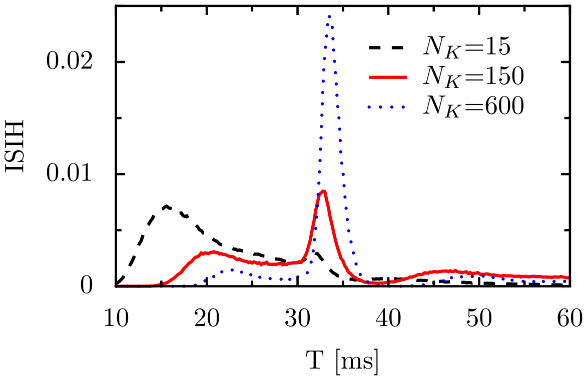

Figure 4.17: Interspike interval histogram (ISIH) against interspike duration T in subthreshold coupling strength for different noise levels corresponding to different number of sodium and potassium channels as indicated. The chosen delay time is $\tau = 30\,\mathrm{ms}$; the coupling strength is set at $\epsilon = 0.03\,\mathrm{mS/cm}^2 < \epsilon_c(\tau)$ and $N_{\mathrm{Na}} = \frac{10}{3} N_{\mathrm{K}}$.

stimulus $I_\tau(t)$ can shift the stable fix-point towards the threshold for excitation, the spikes are more regular. However, the threshold is still kept, and noise is needed to overcome this threshold and to induce the excitation. It means that repetitive oscillatory spiking is supported by noise only. Nevertheless, the subthreshold delayed stimulus determines its own favorite time scale $\mathcal{T}_\tau$ which is the sum of the delay time and the activation time $\mathcal{T}_{\mathrm{act}}$.

In Fig. 4.17, we depict the interspikes interval histogram (ISIH) in the subthreshold regime for different noise levels, i.e. for different numbers of ion channels. Both the intrinsic time scale $\mathcal{T}_{\mathrm{int}}$ and the correspondingly height of the associated peak distinctly depend on the noise level. As noise strength increases, the influence to the generation of spontaneous spikes becomes larger. It results in the change of the intrinsic time scale $\mathcal{T}_{\mathrm{int}}$ and the exponential decay for the larger time intervals. The former sharp maximum peak at $\mathcal{T}_\tau$ tends to a smaller time scale $\mathcal{T}_{\mathrm{int}}$ supported by noise. The intrinsic time scale $\mathcal{T}_{\mathrm{int}}$ becomes broader and towards the minimal time for a interspike interval located at the refractory time. This minimal time which is promoted mainly by the presence of noise, necessarily relates to the delay mechanism. The situation for the time scale $\mathcal{T}_\tau$ induced by the delayed feedback is different. The position of this peak is only slightly affected by the noise level, and the height of the peak drops drastically as the noise increases. It recalls the fact that these spikes require the presence of noise to become activated in the case of an excitable dynamics. The robustness of the positions of the delay induced time scales as well as the susceptible noisy time scale result in the bimodal shape of the ISIH which indicates a noisy synchronization phenomenon [4, 6, 144, 159].

Suprathreshold delay coupling: $\epsilon > \epsilon_c(\tau)$

Next, we consider the situation with coupling strengths above the critical strength, i.e. $\epsilon > \epsilon_c(\tau)$, where the spikes repeat deterministically. The big coupling strength leads a transition from the excitable state to the oscillatory state with repetitive firing. The spikes repeated deterministically lead to sharp peaks in the ISIH, c.f.

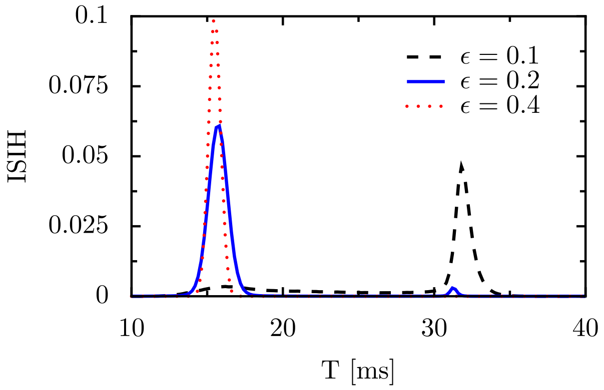

Figure 4.18: Interspike interval histogram (ISIH) *vs.* interspike duration T for different values of the suprathreshold coupling strength $\epsilon > \epsilon_c(\tau)$: The distribution of the interspike intervals is depicted for fixed delay time $\tau = 30\,\mathrm{ms}$, the numbers of ion channels are $N_{\mathrm{K}} = 150$ and $N_{\mathrm{Na}} = 500$. The values of the coupling strengths indicated in the figure are in units of $\mathrm{mS/cm}^2$.

Fig. 4.18.

In Fig. 4.18, the interspike interval histograms (ISIHs) are depicted for fixed noise strength and various suprathreshold coupling strengths. Upon the chosen parameter values for the noise level, i.e. the number of sodium and potassium ion channels, and delay time τ, the ISIH exhibits sharp peaks and more or less pronounced broad background. The broad background diminishes as the coupling increases or noise level decreases. It is clear to find that the height of the peaks sensitively depends on the coupling strength, while the positions are independent. The interesting thing is that as the delayed feedback increases, the system favors $\mathcal{T}_{\mathrm{int}}$, but not the delay-induced time scale $\mathcal{T}_\tau$. To understand this, we look back at Fig. 4.17: The intrinsic time scale $\mathcal{T}_{\mathrm{int}}$ sensitively depends on the noise strength, and exhibits a wide distribution. When the coupling strength is large enough, the intrinsic time scale shifts towards a fraction of the delay-induced time scale $\mathcal{T}_\tau$. As the coupling strength increases, the multimodal structure collapses to a unimodal one, c.f. Fig. 4.18, and all the interspike intervals center at one value. Due to the suprathreshold driving, the spontaneous spikes can be repeated periodically and even the noise dominated scale now collapses towards a narrow peak. The width of the peak gets narrower as the coupling strength increasing, c.f. Fig. 4.18. The delay mechanism is able to stabilize the orbit of the oscillator which is induced by noise.

Next, we study the dependence of the interspike intervals on the delay time τ by considering the mean interspike interval, c.f. Eq. (4.30). In Fig. 4.19 the mean interspike interval $\langle T \rangle$ is depicted with fixed channel noise strength for different coupling strengths. For small suprathreshold coupling strengths, i.e. $\epsilon = 0.1\,\mathrm{mS/cm}^2$, the mean interspike interval exhibits a smooth dependence on the delay time. However, when the suprathreshold coupling strength is big enough, the mean interspike time varies with the delay time τ in an almost piecewise linear fashion, displaying sharp, triangle-like textures, c.f. Fig. 4.19. As the coupling strength increases, the delay coupling mechanism dominates the spiking. That is because for the big coupling strength, the ISIH exhibits a unimodal structure consisting of a sharp peak where

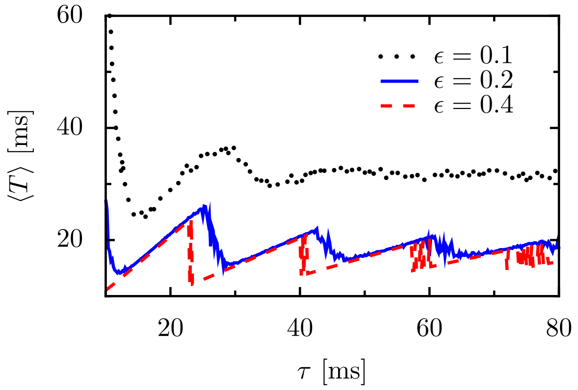

Figure 4.19: Mean interspike interval $\langle T \rangle$ as a function of the delay time τ [115]: The mean interspike interval $\langle T \rangle$ simulated with Eq. (4.30) with the following parameters: the ion channel numbers are $N_{\mathrm{K}} = 150$, $N_{\mathrm{Na}} = 500$ and the coupling strengths are set to $\epsilon = 0.1\mathrm{mS/cm}^2$ (black dashed line), $\epsilon = 0.2\mathrm{mS/cm}^2$ (red dotted line), and $\epsilon = 0.4\mathrm{mS/cm}^2$ (blue solid line).

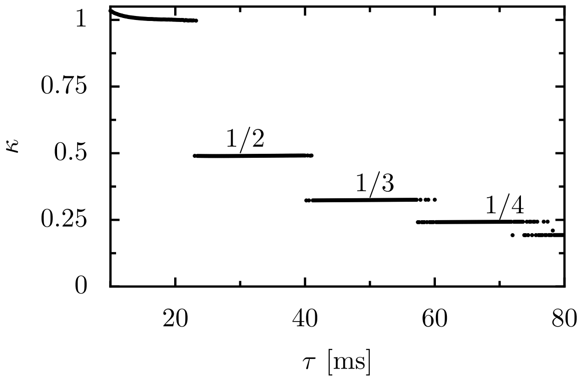

Figure 4.20: The inverse of the number of spikes that fit into the delay-time interval κ is plotted versus the delay time τ with $N_{\mathrm{K}} = 150$, $N_{\mathrm{K}} = 500$ and the delay coupling strength $\epsilon = 0.4\mathrm{mS/cm}^2$ [115].

the intrinsic time scale fits into the delay-induced time scale (shown in Fig. 4.18). Therefore, the mean interspike interval is proportional to the ratio of the delay time τ and the number n of spikes fitting into one delay-induced time interval, reading

$$\langle T \rangle \propto \tau / n \doteq \tau \kappa \,. \tag{4.35}$$

Here, κ is the slope of each piecewise line.

The mean interspike interval inherits the characteristic dependence on τ as the ISIH shape is unimodal. In Fig. 4.19, larger deviations are found during transitions between different synchronized states where the histogram becomes multimodal. Moreover, the slope of each piecewise line versus the delay time τ is depicted in Fig. 4.20. At multiples of the noise-dependent intrinsic time scale, the characteristic steps do occur indeed.

We found that stronger noise strength mimics a decrease of the coupling strength. Nearby the typical steps, noise is able to induce producing new spikes at the end of the intervals. Thus, the ratio κ decreases. Alternatively, noise decreases the number of spikes towards the left boundary of a new synchronized region. Therefore, increasing noise strength attains the similar form as that in the case of lower delay coupling strength.

Several comparable scenarios have been reported in other systems, such as noisy Van der Pol dynamics near the Hopf bifurcation [161–163], semiconductor superlattices [140] and stochastic excitable dynamics [144]. The delayed feedback mechanism serves as a control option for adjusting the peaked distribution of interspike intervals, being of importance for memory storage [160] and stimulus-locked short-term dynamics in neuronal systems [7]. One may therefore speculate whether nature adopted the autapse phenomena for frequencies-filtering in presence of unavoidable intrinsic channel noise.

Phase oscillator modeling

As we have pointed out before, the autaptic feedback leads to a stabilization of the internal rhythmicity, which is determined by the model parameters. This results in synchronized patterns, c.f. Fig. 4.20. The neuron has some common behaviors with the oscillatory system whenever the delay coupling dictates the dynamics. Therefore, it is reasonable to describe the dynamics in terms of a well-known phase oscillator model, the Kuramoto model which was first proposed by Yoshiki Kuramoto to describe the phenomenon of synchronization [164].

Therefore, we compare the observed synchronization in this studied neuronal model with autaptic delayed feedback with a Kuramoto-type model [165] of a phase oscillator including delayed feedback. To simplify the autaptic neuronal system, we neglect the details of the shape of the spike trains, and then the essential information can be reduced to the phase of the oscillatory neuron.

Accordingly, the proposed dynamics for the underlying phase dynamics can be modeled as:

$$\dot{\phi} = \omega - A \sin\left[\phi(t) - \phi(t-\tau)\right] \, , \tag{4.36}$$

where ω denotes the angular intrinsic frequency of the oscillator, i.e. $\omega = 2\pi/\mathcal{T}_{\text{int}}$. Here, A is the delay-coupling strength. Searching for solutions with fixed frequency Ω, we make the ansatz:

$$\phi(t) = \Omega\, t \, . \tag{4.37}$$

Inserting it back into Eq. (4.36), we get the resulting self-consistent equation [166–168]:

$$\Omega = \omega - A \sin\left[\Omega\tau\right] \, , \tag{4.38}$$

which can be solved numerically. In the limit $\tau \to 0$, Eq. (4.38) is approximately given by

$$\Omega = \omega - A\Omega\tau \, . \tag{4.39}$$

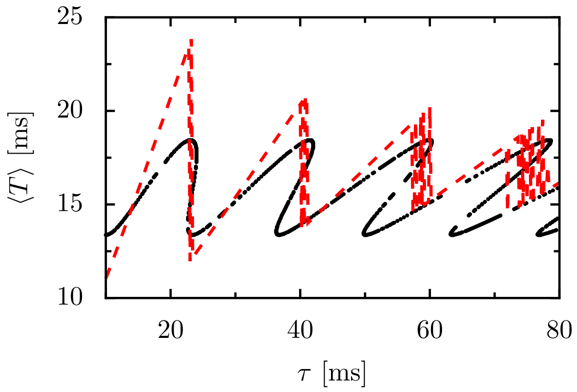

Figure 4.21: Comparison of the stochastic dynamics of the Hodgkin-Huxley model including feedback, Eqs. (4.13), (4.25), (4.26), (4.27), (4.32), (4.33) with the dynamics of the feedback assisted Kuramoto-type phase oscillator model, Eq. (4.36). The mean interspike interval (dashed red lines) is the result of the numerical integration of the stochastic Hodgkin-Huxley model with delayed feedback; there is quantitatively good agreement between period of oscillations as obtained from a phase oscillator dynamics of the Kuramoto-type delayed feedback model (solid black line). Regions with multiple solutions in the phase model correspond to discontinuous jumps between different types of multiplets in the Hodgkin-Huxley model. The parameters for the neuronal modeling are chosen as $N_{\mathrm{K}} = 150$, $N_{\mathrm{Na}} = 500$ and $\epsilon = 0.4\,\mathrm{mS/cm}^2$; those of the phase oscillator are given by oscillator frequency $\omega = 2\pi/15.5\,\mathrm{ms}$ and feedback strength $A = 1/15.5\,\mathrm{ms}$ [115].

Then Ω can be obtained. From our oscillatory stochastic neuron dynamics including an autaptic delayed feedback, we know that the mean oscillator time $T \sim \tau$. Comparing the phase oscillator dynamics with this time, we get

$$T = \frac{2\pi}{\Omega} = \frac{2\pi(1 + A\tau)}{\omega} \sim \tau\,. \tag{4.40}$$

Therefore, we can make the following parameter identification,

$$A = \frac{\omega}{2\pi} = 1/\mathcal{T}_{\mathrm{int}}\,. \tag{4.41}$$

In Fig. 4.21 we present the comparison between the stochastic Hodgin-Huxley model with delayed feedback and the phase oscillator model. Although the quantitative behavior is different, a good qualitative agreement is observed. The positions where the autapse model jumps between bursts of different number of multiplets are nicely reproduced by this simplified phase oscillator model. A further improvement of this model would require a more optimal determination of the τ-dependent parameters of this Kuramoto model with feedback.

In fact, time-delayed coupling as a natural and well-motivated extension of Kuramoto model has been widely studied. It has been found that delayed feedback can substantially change the properties of the dynamics in coupled systems and prompt more interesting behaviors. For example, in 1989, Schuster and Wagner have found the typical fingerprint of delays in two coupled oscillators [166, 169]; Gerstner has proven that delayed couplings may induce rapid phase locking in networks of pulse-coupled oscillators [170]; and evidences have been found that the delayed coupling is

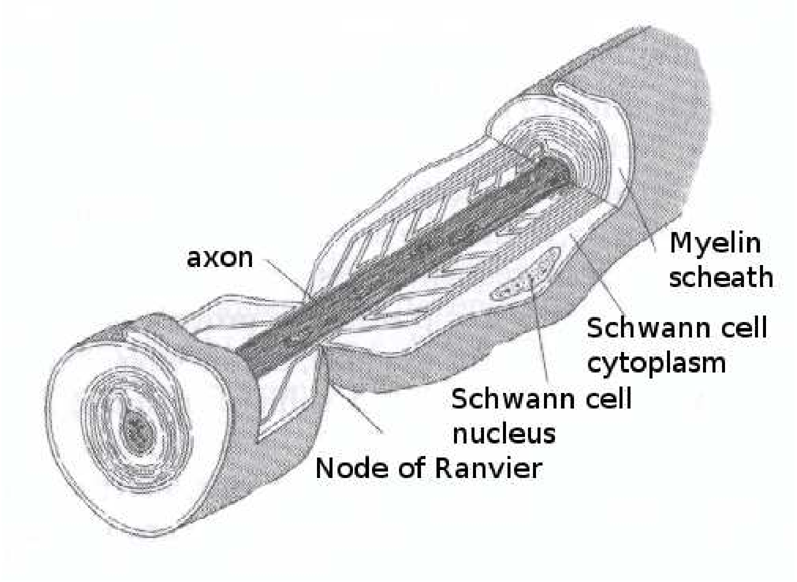

Figure 4.22: Schematic diagram of a typical myelin sheath. [Adapted from J. Keener et al., Mathematical Physiology, Springer (1998)]

the key element for controlling the time evolution of chaotically coupled oscillators by synchronizing their dynamics [5, 171].

4.3 Signal transport in myelinated neurons

In the previous sections, we have studied the generation of action potentials which carry the electrical neuronal signals. In this section we discuss the propagation of these signals in myelinated neurons. We numerically simulated the saltatory spike propagation along the axonal nodes within a multicompartment stochastic Hodgkin-Huxley model. The noise effect must be taken into account since every node of Ranvier is very small [120]. With an external stimulus on the first node of Ranvier, we study the propagation in terms of transmission reliability, i.e. the ratio of the number of spike observed in the terminal node to the number of spikes initiated in the first node. We found that the intrinsic noise plays an important role in the dynamics of the bi-linearly coupled nodes of Ranvier.

4.3.1 Model setup

It has been recognized that the fast propagation of action potentials along the axon plays an very important role in the nervous system, e.g. for the successful evolution to large body sizes of organisms, or the information processing in the brain. Therefore, understanding the propagation mechanisms is of great interest for neuroscientists, physiologists and physicists [172].

There are two kinds of axons: One is covered by layers lipid material called *myelin* and the other one is not. Most nerve fibers are myelinated axons with periodic gaps of exposure called *nodes of Ranvier* where the ion channels are predominantly localized [120]. Typically, the length of the node is very small, around 1 μm while the myelin sheath is as long as $1 \sim 2$ mm [120]. The myelin sheath consists of a single cell named *Schwann cell.* It is wrapped many times (around 100 times) around the axonal membrane (Fig. 4.22) which increases the effective membrane resistance R_m by a factor of about 100 and decreases the membrane capacitance C_m of 100 times. Consequently, the rough date of the membrane resistance R_m is $10^3\ \Omega\,\mathrm{cm}^2$ for cell membrane and $10^5\ \Omega\,\mathrm{cm}^2$ for myelin sheath; the membrane capacitance C_m is $10^{-6}\mu\,\mathrm{F}/\,\mathrm{cm}^2$ for cell membrane and $10^{-8}\mu\,\mathrm{F}/\,\mathrm{cm}^2$ for a myelinated fiber [120].

The propagation along myelinated fiber is much faster than that along unmyelinated fiber [120]. This is presumably caused by the fact that there is little transmembrane ionic current and little capacitive current in the myelinated section. The axon acts like a simple resistor. Therefore, in myelinated axons, the action potential generated only at the small nodes of Ranvier. Instead of propagating continuously along the myelinated fiber, the action potential prefers to jump from node to node. This kind of node-to-node propagation is called *saltatory* (from the Latin word *saltare* that means to leap or dance) which has been demonstrated by Huxley, Stämpfli and Tasaki [173, 174].

Compared with the unmyelinated fibers, the myelinated fibers have a reliable and rapid way to communicate impulses at a much reduced cost, i.e. at the same conduction velocity, a myelinated fiber can be up to 50 times thinner than an unmyelinated fiber [121]. This large factor in packing makes the brain to squeeze more than one million axons into a single nerve which propagates information to the brain. At the same time, myelinated fiber also drastically reduces the metabolic cost of neural computation. For a single neural impulse (in the order of 1 ms), each sodium channel transfers up to 10^4 sodium ions into the cell and then pumped back to restore the appropriate steady-state electrochemical potential. One ATP molecule should be hydrolyzed to transfer three sodium ions [120], i.e. about $3 \cdot 10^3$ ATP molecules per ion channel are needed for every neural spike.

In 1952, Hodgkin and Huxley proposed a realistic description for the space clamped action potential. Since then, they have successfully studied the firing dynamics respecting to spike generation within their deterministic modeling [28]. It turns out that the propagation along the axon should occur with a fixed speed [120]. Recently studies have shown that the intrinsic noise is important not only for the generation of spontaneous spikes, but also for the saltatory spikes propagation [175]. Due to the finite number of ion channels (in the order of 10^4) in the nodes of Ranvier, the intrinsic noise can not be neglected [130, 157].

Here, we consider a compartmental stochastic Hodgkin-Huxley model [175] to model the signal transmission along myelinated axons. It means that each node of Ranvier is described by a stochastic Hodgkin-Huxley equation, and linearly couples to its nearest neighbors. Consequently, the membrane dynamics V_i at the ith node of Ranvier reads,

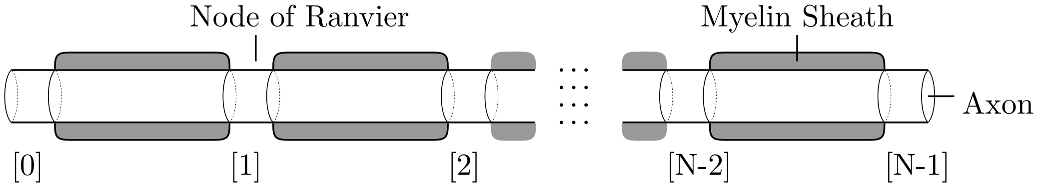

Figure 4.23: Sketch of the myelinated axon [116]: The nodes of Ranvier with the length of λ is depicted in light gray, and the myelin sheath which has a length of L is in dark gray. Each node of Ranvier is treated within a stochastic generalization of the Hodgkin-Huxley model and is bi-linearly coupled with the nearest neighboring nodes of Ranvier.

$$C\frac{\mathrm{d}}{\mathrm{d}t}V_i = I_{i,\mathrm{ionic}}(V_i) + I_{i,\mathrm{inter}}(t) + I_{i,\mathrm{ext}}(t)\,, \tag{4.42}$$

with $i = 0, 1, 2, ..., N-1$, where N corresponds to the total number of axonal nodes of Ranvier. The ionic membrane current (per unit area) $I_{i,\mathrm{ionic}}(V_i)$ within the ith node of Ranvier has the same expression as the original Hodgkin-Huxley model [28], i.e. Eq. (4.7) and Eq. (4.8) written as,

$$I_{i,\mathrm{ionic}}(V_i) = -g_{\mathrm{K}}^{\max}\; n_i^4\; (V_i - E_{\mathrm{K}}) - g_{\mathrm{Na}}^{\max}\; m_i^3 h_i\; (V_i - E_{\mathrm{Na}}) - g_{\mathrm{L}}(V_i - E_{\mathrm{L}})\,. \tag{4.43}$$

The inter-nodal currents $I_{i,\mathrm{inter}}(t)$ in Eq. (4.42) reads,

$$I_{i,\mathrm{inter}}(t) = \begin{cases} \kappa\,(V_{i+1} - V_i) & \text{for} \quad i = 0, \\ \kappa\,(V_{i-1} - V_i) & \text{for} \quad i = N-1, \\ \kappa\,(V_{i-1} - 2V_i + V_{i+1}) & \text{elsewhere}\,. \end{cases} \tag{4.44}$$

Here, κ is the coupling strength between next-neighboring nodes. It depends on the length L of the internodal *passive* segment of the axon as well as on the resistivity of the extracellular and intracellular medium and also depends on the ratio of the node's diameter d and its length λ which is typically two orders of magnitude larger than its diameter [120, 121]. In our study, this coupling strength κ serves as a controllable parameter.

The external current stimuli per unit area at the ith node of Ranvier $I_{i,\mathrm{ext}}(t)$ in Eq. (4.42) is a constant current stimulus only on the first node. It can be written as,

$$I_{i,\mathrm{ext}}(t) = \begin{cases} 12\,\mu\mathrm{A/cm}^2 & \text{for} \quad i = 0, \\ 0 & \text{elsewhere.} \end{cases} \tag{4.45}$$

All parameters, which keep the same values as in the original Hodgkin-Huxley model, are given in Table 4.1.

4.3.2 The signal transmission

Since we are interested in the transmission along the whole chain, the number of spikes arriving at the terminal node is to be analyzed. In order to study the transmission reliability, we exemplary consider a chain consisting of ten nodes of Ranvier,

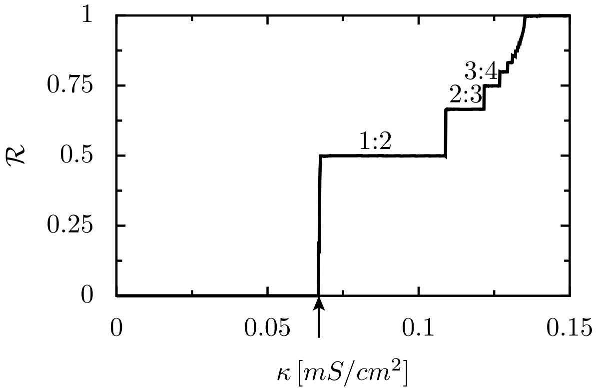

Figure 4.24: Dependence of the transmission reliability coefficient $\mathcal{R}$ on the inter-nodal coupling strength κ depicted for the deterministic spike propagation in a myelinated axon containing $N = 10$ Ranvier nodes. The arrow indicates the threshold value $\kappa_c = 0.067\,\mathrm{mS/cm^2}$. For subthreshold $\kappa \lesssim 0.067\,\mathrm{mS/cm^2}$ there is no spike propagation, i.e. $\mathcal{R} = 0$. Perfect spike transmission, i.e. $\mathcal{R} = 1$, is observed for the suprathreshold case $\kappa \gtrsim 0.136\,\mathrm{mS/cm^2}$. Discrete numbers $k : l$ for the transmission reliability are found in the intermediate range.

i.e. $N = 10$. This particular choice of the number of nodes is somewhat arbitrary, and all those obtained results can be extended to large numbers of nodes as well. From the numerical simulation, we find that the periodical produced spikes on the first node which are generated by the stimuli, propagate along the transmission line. To quantify this propagation, we define the transmission reliability coefficient $\mathcal{R}$ as the ratio of the number of spikes arriving at the terminal node $\mathcal{N}_9$ to those generated in the initial node $\mathcal{N}_0$ in steady state. It has the form,

$$\text{transmission reliability coefficient: } \mathcal{R} = \frac{\mathcal{N}_9}{\mathcal{N}_0}\,. \tag{4.46}$$

The occurrence of a spike is identified as before, and the spike occurrence time is t_i^j, with $j = 1, ..., \mathcal{N}_i$, where $\mathcal{N}_i$ indicates the number of spikes appeared on the specific node i. Thus, the membrane potential $V_i(t)$ can be simplified to a point processes $u_i(t) = \sum_{j=1}^{\mathcal{N}_i} \delta(t - t_i^j)$. In our simulation, more than 2000 spikes are generated on the first node.

Deterministic limit

We start with the deterministic condition, which is formally achieved in the limit $\mathcal{A} \to \infty$, and use the same method to numerically integrate the coupled Hodgkin-Huxley model, Eq. (4.42). In order to achieve equilibration along the whole chain, we use the following protocol: (1) We apply the constant external stimuli $I_{i,\mathrm{ext}}(t)$, i.e. Eq. (4.45) on the first node, and integrate over 100 ms without coupling, i.e. $\kappa = 0$, to get a steady state for individual node; (2)Then, we switch on the coupling κ; (3) We begin to record the spikes after integrating over 200 ms. Due to the suprathreshold stimuli on the first node, the membrane potential of this node V_0 exhibits a limit cycle. Therefore, periodic spikes are generated on the initial node. Initially, all the other nodes are prepared in the rest state in this method.

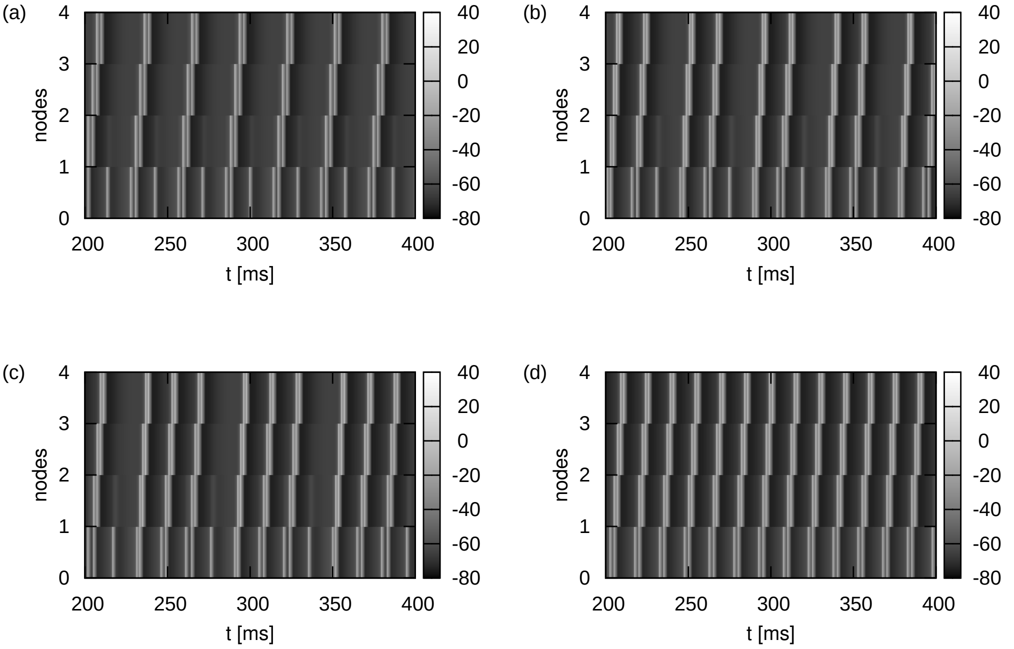

Figure 4.25: Spike propagation in a myelinated neuron for deterministic limit [116]. Different parameters are chosen from different transmission patterns steps in Fig. 4.24 (a) $\kappa = 0.08$ for the transmission reliability coefficient $\mathcal{R} = 1 : 2$, (b) $\kappa = 0.115$ for $\mathcal{R} = 2 : 3$, (c) $\kappa = 0.124$ for $\mathcal{R} = 3 : 4$ (d) $\kappa = 0.14$ for $\mathcal{R} = 1 : 1$.

In Fig. 4.24, we plot the dependence of the transmission reliability $\mathcal{R}$ on the coupling strength. Staircase-like steps are observed, and two important points that should be mentioned are the critical values: $\kappa_{c1} = 0.067\,\mathrm{mS/cm^2}$ and $\kappa_{c2} = 0.136\,\mathrm{mS/cm^2}$. For the coupling $\kappa \lesssim 0.067\,\mathrm{mS/cm^2}$, which is called subthreshold coupling, the transmission reliability $\mathcal{R}$ vanishes. It means that the spike propagation fails for small coupling strength. Obviously, in this case, the action potential can not excite the neighbore node, and no spike arrives at the terminal node. In the opposite limit, for sufficiently large coupling parameter which is named suprathreshold, i.e. $\kappa \gtrsim 0.136\,\mathrm{mS/cm^2}$, $\mathcal{R} = 1$. Every generated spike propagates along the axon and arrives at the final node. 100% signal transmission efficiency is achieved. The most interesting observation is in the intermediate range, i.e. $\kappa_{c1} < \kappa < \kappa_{c2}$, where discrete rational transmission patterns $k : l$ occurred. Here, k is the number of spikes transmitted to the final node, while l is the number of spikes generated on the first node. To understand more about how this discrete transmission works, we give some examples about the propagation patterns in presence of first four nodes in Fig. 4.25. The different transmission patterns [see (a)1:2, (b) 2:3, (c) 3:4, (d) 1:1] are clearly obtained. For example, in the panel (a) which is for the ratio of 1:2, every second spike propagates along the axon chain.

A similar phenomenon has been found when one drives the Hodgkin-Huxley system with an ac-sinusoidal signal, where the spike events and the driving periods exhibits the same rational number ratio [176].

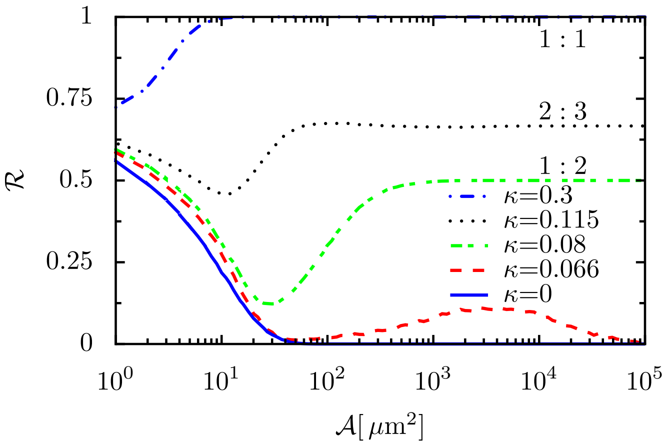

Figure 4.26: Transmission reliability in presence of channel noise [116]: The transmission reliability coefficient $\mathcal{R}$ is plotted against the membrane size of the node of Ranvier for different strengths of the inter-nodal coupling (the coupling strengths are given in units of $\mathrm{mS/cm^2}$). The data confirms the results of noise-assisted spike propagation for subthreshold coupling (see dashed red line) [175]. Moreover, the minimum in $\mathcal{R}$ indicates the cross-over from a stochastic, uncorrelated spiking of the initial and final nodes towards a causal, noisy spike transmission from the initial to the final node.

Noise-assisted spike propagation

Next, we consider the finite size $\mathcal{A}$ of nodes of Ranvier. In this case, the noise intensity has to be taken into account. To study the noise effect on the propagation of spikes along the axons, we numerically integrate the linear coupled stochastic Hodgkin-Huxley model described by Eqs. (4.42). Following the same protocol for the deterministic case, we computed the transmission reliability coefficient $\mathcal{R}$ of the spikes generated in the initial node propagating to the final node. The staircase-like dependence of the transmission reliability coefficient $\mathcal{R}$ which is depicted in Fig. 4.24 for the deterministic case, turns to a continuous dependence (not shown) [175].

The dependence of the transmission reliability coefficient $\mathcal{R}$ on the noise strength is plotted in Fig. 4.26. In the limit of large membrane, the noise approaches zero. Thus, the transmission reliability coefficient tends to the deterministic stair value found in Fig. 4.24. In the opposite limit, i.e. for small sizes of the nodes of Ranvier approaching formally zero (strong noise), the coefficient $\mathcal{R}$ tends to a finite value. This value is independent of coupling strength κ, which implies that there is no causal relationship between the spiking at the initial and the terminal nodes. For the rather strong noise case, noise is in charge of the dynamics of the membrane potential of each node, and determines the number of occurrences of spikes at the final node. The number of occurrences $\mathcal{N}_9$ does not markedly depend on the actual value of the coupling parameter. Hence, the influence of the bi-linear coupling can be negligible. In fact, the firing events at the initial and terminal nodes become completely uncorrelated in the limit of strong noise intensities: There is no signal transmission, but only noise. For the medium noise strength, the transmission depends on both membrane size $\mathcal{A}$ and coupling strength κ. The transmission reliability coefficient $\mathcal{R}$ exhibits much richer phenomena for different coupling strength. We will discuss them in different coupling regime.

First of all, in the limit $\kappa \to 0$, the spikes on the initial and the terminal nodes are independently. Consequently, $\mathcal{R}$ is given by the ratio of the number of spontaneous spikes occurring within the non-stimulated, stochastic Hodgkin-Huxley dynamics and the number of spikes occurring within the stochastic Hodgkin-Huxley dynamics complemented by a constant current stimulus of $I = 12\,\mu\text{A/cm}^2$. The causal relationship is lost in this case. This is an evidence for the cross-correlation between the spikes on the initial and final nodes (see below). As membrane decreases (noise increases), the transmission reliability coefficient $\mathcal{R}$ remains decreasing from the limit value for the suprathreshold coupling, while it firstly decreases and then increases for the other coupling strength. For the suprathreshold case, the noise induces the 100% transmission failure as noise increases. More phenomena are found for the subthreshold coupling strength: A noise-assisted spike propagation phenomenon is found. The transmission reliability coefficient $\mathcal{R}$ exhibits a maximum, indicating an optimal spike propagation from the initial node to the final node c.f. Fig. 4.26 [175]. In this case, the coupling between the nodes does not result in any efficient propagation of the spikes and possibility. The intrinsic noise overcomes the threshold for excitation. However, as the coupling strength increases, the strong coupling reigns the dynamics and the noise-induced propagation fails. Then, the maximum peek disappears for the transmission reliability coefficient $\mathcal{R}$, c.f. Fig. 4.26. $\mathcal{R}$ decreases firstly and then increases as noise decreases. The cross-over from the stochastic non-causal firing regime to the one with stable value occurs.

To give a better understanding, we give cases of spike propagation in the node chain for different noise strength with a fixed coupling strength in Fig. 4.27. Here, we choose the coupling strength $\kappa = 0.08\,\text{mS/cm}^2$ that is in the inter-mediate regime. For rather strong intrinsic noise which is achieved by very small sizes of the nodes of Ranvier, here we give an example as 10 μm^2 in panel (a) of Fig. 4.27. Every node has a high possibility to generate spontaneous spikes, which can stimulate the neighboring nodes via the coupling. Consequently, a transmission to both sides occurs. Tracking the behavior of a given chain, we found that some spikes initiated at the first node collide with a particularly large fluctuation. Thus, the spikes propagation fails. As the nodal membrane of size $\mathcal{A}$ increases, i.e. the noise strength decreases, the failed propagation decreases (c.f. Fig. 4.27 (a) and (b)). And the transmission becomes more regular. When the membrane of the Ranvier size is as large as $3 \cdot 10^4\,\mu\text{m}^2$, the transmission coefficient $\mathcal{R}$ tends to its deterministic limit value, seen Fig. 4.27 (c). The $1:2$ transmission pattern is recovered.

From Fig. 4.27, we can see that the transmission reliability coefficient $\mathcal{R}$ is maintained in different ways. In the case of small noise strength, c.f. panel (c), the spikes on the terminal nodes are propagated from the first node. However, in the case of large noise strength, c.f. panel (a), some spikes on the terminal node are generated by the noise. The spikes in the initial and final nodes have no causal relationship. The cross-over from the stochastic, non-causal firing regime to noisy spike transmission depends on the coupling strength. From Fig. 4.26, we found that for stronger coupling strengths, this cross-over occurs at smaller nodal membrane sizes $\mathcal{A}$.

It is notable that in the limit of large noise strength, the causal relationship

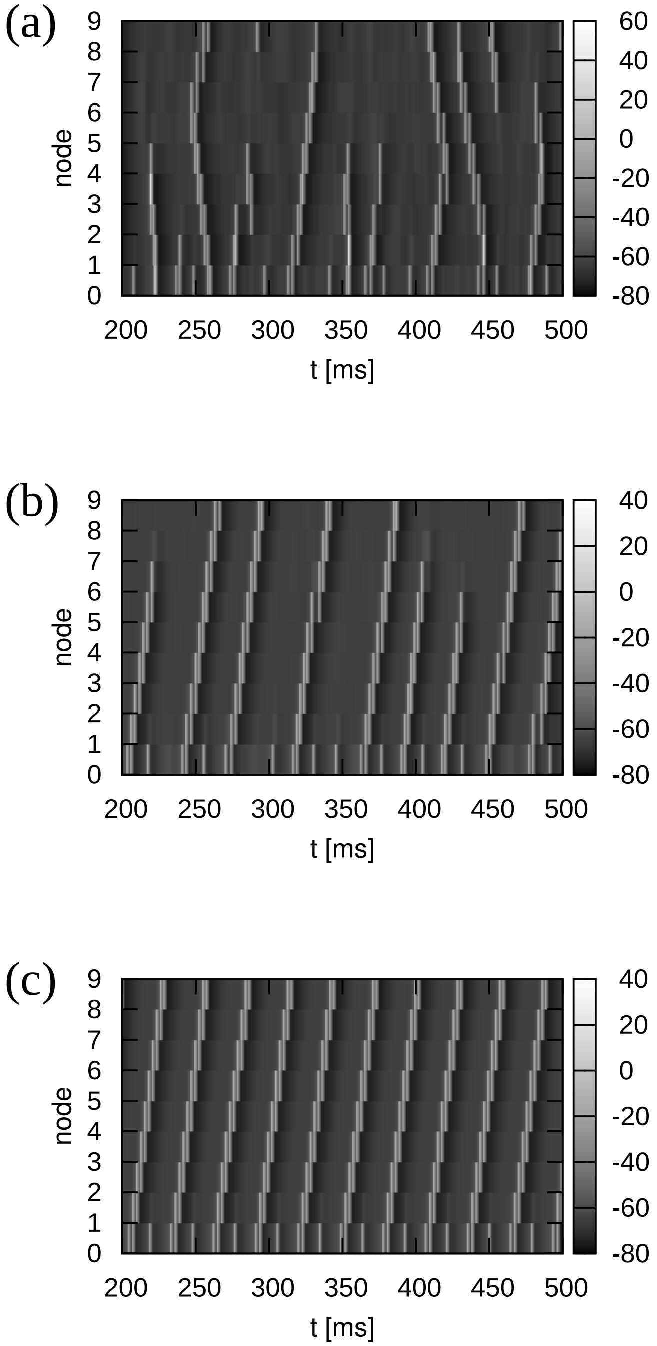

Figure 4.27: Spatial-temporal transmission patterns of spike propagation [116]: The spatial-temporal evolution of the membrane dynamics at different axonal nodes of Ranvier is plotted for an intermediate coupling strength $\kappa = 0.08\,\mathrm{mS/cm^2}$ and various nodal membrane sizes: (a) $\mathcal{A} = 10\,\mu\mathrm{m}^2$ (strong channel noise); (b) $\mathcal{A} = 100\,\mu\mathrm{m}^2$ (intermediate channel noise) and (c) $\mathcal{A} = 3 \cdot 10^4\,\mu\mathrm{m}^2$ (weak channel noise). Next to each panel, there is a color bar indicating the actual value of the membrane potential. The action potentials are created by a current stimulus at the initial node ("0"). In case of low noise level, c.f. panel (c), the deterministic transmission pattern of 2 : 1 is clearly visible. In contrast, in the strong noise limit, due to the dominating spontaneous spiking, irregular transmission is found.

between spiking in the first and that on the terminal node gets lost, which means the spiking correlation gets lost. The transmission reliability coefficient $\mathcal{R}$ which is maintained by the spontaneous spikes, is not enough to describe the propagation from the first node to the final node. Therefore a new parameter, i.e. the spike correlation is studied. We determine it as follows: Firstly, we divide the point processes $u_0(t)$ and $u_9(t+\tau)$ into segments of width Δt. The width Δt must be smaller than the refractory time to make sure that there is either no spike or one spike observable in each segment. In our analysis, we chose $\Delta t = 1.5\,\mathrm{ms}$. Secondly, we count the number of coincidence spikes $\mathcal{N}_{0,9}(\tau)$ between the initial node and the final node in each segment with width Δt, i.e. the spikes occurring at the same time interval between the two point processes $u_0(t)$ and $u_9(t+\tau)$ with an error width Δt. It has the following form:

$$\mathcal{N}_{0,9}(\tau) = \Delta t \int_0^T \mathrm{d}t\, f_0(t) f_9(t+\tau)\,, \tag{4.47}$$

where the spike number in a segment $f_i(t)$ (i=0, 9) is approximated by

$$f_i(t) = \int_t^{t+\Delta t} \mathrm{d}t' u_i(t')/\Delta t \;\; \text{for } i = 0,\, 9\,. \tag{4.48}$$

In Eq. (4.47), T denotes the total integration time. Note that the above definition corresponds to a cross-correlation measurement. Thirdly, we normalize this number $\mathcal{N}_{0,9}(\tau)$ with the number of spikes on the first node "0", i.e. $\mathcal{N}_0$ and the bin-width Δt. Then, the probability density $C_{0,9}(\tau)$ is obtained:

$$C_{0,9}(\tau) = \frac{\mathcal{N}_{0,9}(\tau)}{\Delta t \mathcal{N}_0} = \frac{1}{\mathcal{N}_0} \int_0^T \mathrm{d}t\, f_0(t) f_9(t+\tau)\,. \tag{4.49}$$

Due to the periodic spiking generated on the first node, $C_{0,9}(\tau)$ is also periodic, c.f. Fig. 4.28. To ensure that the integral of $C_{0,9}(\tau)$ over one period results in the transmission coefficient $\mathcal{R}$ defined by Eq. (4.46), the total number of spikes on the first node $\mathcal{N}_0$ is used in the normalization.

$C_{0,9}(\tau)$ determines the number of the coincident spikes between the initial node at time t and the final node at a later time $t+\tau$. Larger $C_{0,9}(\tau)$ indicates a higher correlation. In Fig. 4.28, we present the spike correlation $C_{0,9}(\tau)$ for different noise strength in different coupling regimes. In the situation of intermediate coupling shown in Fig. 4.28 (b), the correlation measurement $C_{0,9}(\tau)$ exhibits a sharp peak for a τ-value for the weak noise strength. This time value corresponds to the propagation time modulo the period of the spiking in the initial node. As the noise strength increases, the width of the peak becomes broader and the height of the peak compared to the background level decreases until the total disappearance of the peak in the background. It means the causal correlation gets lost. The broadening and flattening of the peak with increasing noise can also be observed in the subthreshold regime, shown in Fig. 4.28 (a). More interestingly, there is a shift of the peak towards smaller τ-values showing a speed up of the transmission. It can be explained by the same argument as drawn by the effect of *anticipated synchronization* described in Ref. [156].

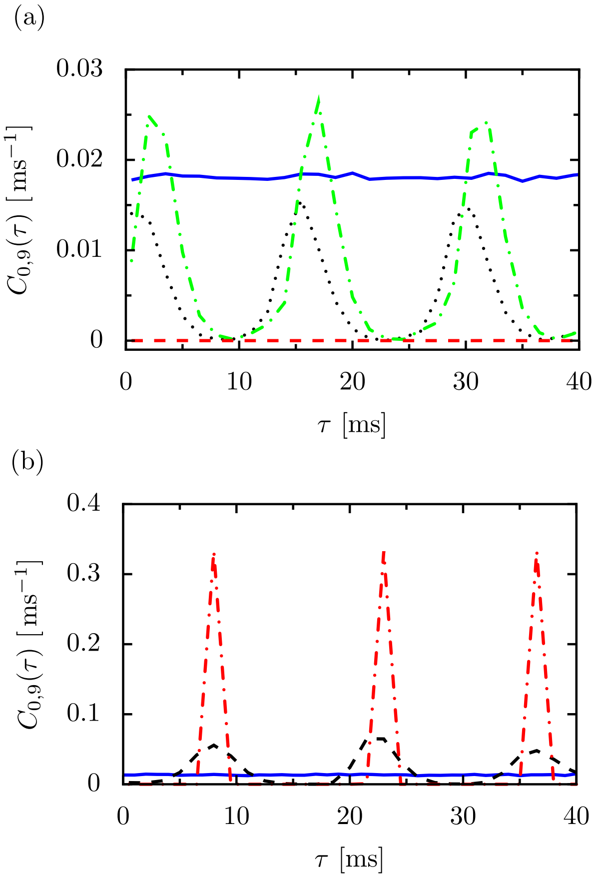

Figure 4.28: Initial-final-node spiking correlation [116]: The spike correlation $C_{0,9}(\tau)$ between the spiking at the initial node and that of the final node, c.f. Eq. (4.49), is plotted for different coupling strengths κ and membrane sizes $\mathcal{A}$: In panel (a) for subthreshold coupling $\kappa = 0.066\,\mathrm{mS/cm^2}$ and membrane sizes $\mathcal{A} = 10\,\mu\mathrm{m}^2$ (blue solid line), $\mathcal{A} = 800\,\mu\mathrm{m}^2$ (black dotted line), $\mathcal{A} = 3 \cdot 10^3\,\mu\mathrm{m}^2$ (green dash-dotted line) and $\mathcal{A} = 5 \cdot 10^5\,\mu\mathrm{m}^2$ (red dashed line); In panel (b) for intermediate coupling $\kappa = 0.08\,\mathrm{mS/cm^2}$ and membrane sizes $\mathcal{A} = 10\,\mu\mathrm{m}^2$ (blue solid line), $\mathcal{A} = 100\,\mu\mathrm{m}^2$ (black dashed line), $\mathcal{A} = 3 \cdot 10^4\,\mu\mathrm{m}^2$ (red dash-dotted line). For weak intrinsic noise the sharp peak indicates a strong correlation. In contrast, in the strong noise limit the causal relationship is lost and the correlation function does not exhibit a peak. Interestingly, for the subthreshold case a shift of the peak towards shorter times is observed, i.e. there is a speed up of the signal transmission with increasing noise level.

4.4 Conclusions

First of all, we present a brief introduction of the cell signaling on the neurophysiology level. The most important model, i.e. the Hodgkin-Huxley model in the study of biophysical mechanisms of generation of action potentials is discussed in detail. Moreover, the stochastic Hodgkin-Huxley model is presented by taking into account of the channel noise. After the introduction, we study the noise-assisted generation and propagation of signals in particular neurons.

We investigated the autapse phenomenon by considering the effect of delayed feedback on the dynamics of a stochastic Hodgkin-Huxley neuron model. Using the original Hodgkin-Huxley parameters, we numerically simulated the stochastic Hodgkin-Huxley model taking into account of the effects of intrinsic channel noise. An additional Pyragas-like delayed feedback mechanism is employed to model the autapse phenomena, in which a neuron's dendrite back-couples to itself. The two basic control parameters investigated in our study are the strength of the autapse-coupling ϵ and the delayed time τ resulting from the finite length of the self-connecting dendrite. We found that the neuron dynamics exhibits intriguing new time scales which stem from the autaptic connection. Since the rest state of the neuron is always stable, noise or an initial spike is necessary for creating an activity, i.e. the spiking dynamics. For a small number of Na and K channels, the noise becomes sizable and the excitatory dynamics remains practically unaffected by the delay feedback. In contrast, smaller noise levels and stronger coupling strengths can induce different synchronization phenomena between the delay time and the intrinsic time scales (also noise dependent). A special frequency-locking mechanism is detected for the mean interspike interval $\langle T \rangle$. We further underline that our exemplary study can be mimicked qualitatively in terms of a reduced description given by the well-known Kuramoto phase model with a built-in feedback.

We have numerically studied the saltatory spike propagation along a myelinated axon within a multi-compartmental, stochastic Hodgkin-Huxley modeling. The channel noise affecting the dynamics of the bi-linearly coupled nodes of Ranvier is originated from the random gating of the ion channel. Upon analyzing the spike propagation in terms of transmission reliability, i.e. the ratio of the number of spikes observed in the final node to the number of spikes initiated in the first node, we found a reduction of the transmission reliability with increasing channel noise level for suprathreshold coupling. This is due to the failure of the noise induced propagation. A further increase of the channel noise level leads to the total loss of the causal correlation between the first and the last nodes of Ranvier of the axonal chain. In case of subthreshold coupling and not so high channel noise level, the channel noise can constructively contribute to the spike propagation and hence the effect of noise-assisted spike propagation is recovered. Both the transmission reliability as well as the propagation speed can be increased with increasing channel noise level. This behavior is quite in spirit of the stochastic resonance phenomenon [3, 177] with an intrinsic noise source [134, 178] where the inter-nodal coupling plays the role of a nodal stimulus.

5 Outlook

In the present thesis, we have investigated the noise effect on transport in artificial channels and nervous systems. We have found many interesting phenomena. Here, we list some potential further works.

Entropic transport

We have studied the entropic transport which arises from the geometric confinement and found that the transport properties sensitively depend on the geometrical structures. Although the boundary confinement has been taken into account, our model is too ideal to fully explain the experimental data from the transport in nano-scaled channels or pores.

Recently, Ulrich Rant and his group have proposed a new device to investigate DNA molecules with nanopores [179]: Namely the so-called "pore-cavity-pore" (PCP) device. It is a nanofluidic silicon device which consists of two stacked nanopores forming in/outlets to a pyramidal cavity of micrometer dimensions. They have experiments with single fluorescent nanoparticles and particle-ensembles to pass through the PCP device. In Ulrich Rant's group, the escape of particles initially localized within the cavity through one of the nanopores was considered. The trajectories and residence times have been recorded and analyzed. It turns out that the single particle transport can be understood by analysis of escape problem. However, the behavior for ensemble of particles has not been fully studied. We aim to extend our previous single-particle studies towards a more realistic modeling of these experiments.

In the experiments the translocation of DNA through a nanopore is utilized for sequencing the DNA molecule. In doing so, the ionic current through the pore is measured. Twisting and turning of the DNA strand generates a lot of noise into the ionic current signal. To reduce the structural fluctuations, an electric field is used to drive the translocation of the DNA [26]. In the experiments done by Aksimentiev and his co-workers, they found that the interactions between the DNA bases and the nanopore surface slow down the translocation of the DNA [26]. As DNA is a highly charged polymer, there are interactions, including the particle-particle interactions (DNA-ions, ions-ions) and particle-wall interactions (DNA-wall, ions-wall). Therefore, in our further studies the interactions should be taken into account.

Neuron signaling

For the neuron signaling, we have studied a neuron exhibiting autapse phenomena. In our model, the auto-delayed feedback mechanism is described by a current which is simply proportional to the difference of the actual membrane potential and the membrane potential at an earlier time. This is too simple to describe the behavior of autapses which appeared to be chemical synapses [32]. Typically, a synapse consists of a *presynaptic* axonal terminal and a *postsynaptic* process. For a chemical synapse, the presynaptic electrical signal is converted into a chemical signal and then back into a postsynaptic electrical signal. This process involves a complex temporal evolution. How the presynaptic signal affects the postsynaptic electrical signal is under investigation for an autapse. As more and more experimental data are recorded, we can have a better understanding of this process.

Synchronization phenomena can be further studied on the propagation of signals in the neuronal systems. In the study of spiking synchronization of two ion channel clusters coupled linearly, Zeng and Jung proposed a new method to describe the synchronization strength [180]. In their method, they considered the synchronization which is achieved when the spiking time difference between the spikes from two different nodes is less than 3 ms. The synchronized spiking number is a good tool to study the coincidence of the spiking time. It can also be used to study the synchronization in the propagation along long axon chains.

Besides the research at cell level, another interesting research topic is to study the collective behavior at the level of neural networks. Neurons never work isolatedly and their functions are often modulated by other neurons and the environment. Therefore, it is crucial to study neural mechanisms at networks and ultimately link the findings to natural behavior, such as learning, memory storage, decisions and cognition.

A Appendix

A.1 Mean First Passage Time

We give a detailed derivation of the first passage time to determine the transport quantities such as the average particle current and the mobility.

The first passage time is the first time of a stochastic process $x(t)$ to reach the boundary or leave a given domain Ω. We start with the realizations initiated at x_s in the domain Ω (Fig. A.1). Here, $x(t)$ is a one-dimensional stochastic process and Ω is a interval with one absorbing boundary at x_1 and one reflecting one at $x_0 < x_1$. The first passage time T is the time to reach the boundary x_1 for the first time. To study the first passage time, we first calculate the probability density $P_\Omega(x,t)$ for $x(t)$ starting from $x(0) = x_s$ at $t = 0$ to reach x in the given domain at time t. It satisfies the Fokker-Planck equation,

$$\frac{\partial P_\Omega(x,t)}{\partial t} = \mathcal{L} P_\Omega(x,t), \tag{A.1}$$

where $\mathcal{L}$ is the Fokker-Planck operator. The probability function $W(T)$ of the realizations that start from x_s and have not reached the absorbing boundary x_1 at time T is,

$$W(T) = \int_{x_0}^{x_1} P_\Omega(x,T)\mathrm{d}x. \tag{A.2}$$

The distribution function $w(T)$ for the first passage time T is given by

$$w(T) = -\frac{\mathrm{d}W(T)}{\mathrm{d}T} = -\int_{x_0}^{x_1} \dot{P}_\Omega(x,T)\mathrm{d}x. \tag{A.3}$$

The average first passage time T_1 is,

$$T_1 = \int_0^\infty T w(T)\mathrm{d}T = -\int_{x_0}^{x_1} \mathrm{d}x \int_0^\infty T\dot{P}_\Omega(x,T)\mathrm{d}T\,. \tag{A.4}$$

With partial integration, we can get,

$$T_1 = \int_{x_0}^{x_1} \mathrm{d}x \int_0^\infty P_\Omega(x,T)\mathrm{d}T\,. \tag{A.5}$$

By applying the backward operator $\mathcal{L}^+$ which is the adjoint operator of $\mathcal{L}$ to Eq. (A.5), the following equation is obtained [46, 181],

$$\mathcal{L}^+ T_1 = -1\,. \tag{A.6}$$

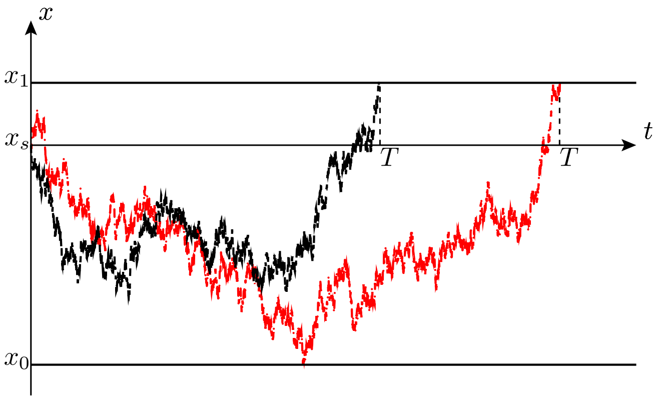

Figure A.1: First passage times T to leave the domain $[x_0, x_1]$ from x_s.

The Fokker-Planck operator for the dimensionless Langevin equation Eq. (3.9) has the form,

$$\mathcal{L} = \frac{\partial}{\partial x}\left[D_0 e^{-\beta V(x)} \frac{\partial}{\partial x} e^{\beta V(x)}\right]. \tag{A.7}$$

The corresponding backward Kolmogorov operator for the Markov process is,

$$\mathcal{L}^{+} = e^{\beta V(x)} \frac{\partial}{\partial x}\left[D_0 e^{-\beta V(x)} \frac{\partial}{\partial x}\right]. \tag{A.8}$$

Thus,

$$\mathcal{L}^{+} T_1 = e^{\beta V(x)} \frac{\partial}{\partial x}\left[D_0 e^{-\beta V(x)} \frac{\partial}{\partial x}\right] T_1 = -1. \tag{A.9}$$

By integration, we get

$$\frac{\partial}{\partial x} T_1 = \frac{e^{\beta V(x)}}{D_0}\left[-\int_a^x e^{-\beta V(z)} \mathrm{d}z + K_1\right], \tag{A.10}$$

where, a is an arbitrary point in the given domain Ω, and K_1 is an integration constant. For the reflecting boundary conditions at $x = x_0$,

$$\frac{\partial T_1}{\partial x}|_{x=x_0} = 0. \tag{A.11}$$

With Eq. (A.10), one obtains

$$K_1 = \int_a^{x_0} e^{-\beta V(z)} \mathrm{d}z. \tag{A.12}$$

Substituting Eq. (A.12) back into Eq. (A.10), for $x > x_0$, one obtains

$$\frac{\partial}{\partial x} T_1 = -\frac{e^{\beta V(x)}}{D_0} \int_{x_0}^x e^{-\beta V(z)} \mathrm{d}z. \tag{A.13}$$

Integrating once more, the following equation is obtained

$$T_1 = -\int_b^x \frac{e^{\beta V(y)}}{D_0} \mathrm{d}y \int_{x_0}^y e^{-\beta V(z)} \mathrm{d}z + K_2\,, \tag{A.14}$$

where b is an arbitrary point in the given domain Ω, and K_2 is second integration constant. For the absorbing boundary condition at $x = x_1$, $T_1(x_1) = 0$, thus,

$$K_2 = \int_b^{x_1} \frac{e^{\beta V(y)}}{D_0} \mathrm{d}y \int_{x_0}^y e^{-\beta V(z)} \mathrm{d}z. \tag{A.15}$$

Then, we substitute Eq. (A.15) back in Eq. (A.14) and get,

$$T_1 = \int_x^{x_1} \frac{e^{\beta V(y)}}{D_0} \mathrm{d}y \int_{x_0}^y e^{-\beta V(z)} \mathrm{d}z\,. \tag{A.16}$$

In the dimensionless Langevin equation (Eq. (3.9)), the effective potential is in the form $V(x) = U(x) - fx$ with $U(x + 1) = U(x)$. We consider the domain $(-\infty\ ,\ x_s + 1)$ with the starting point x_s (i.e. $x_0 \to -\infty$ and $x_1 = x_s + 1$).

$$T_1(x_s) = \int_{x_s}^{x_s+1} \frac{e^{\beta V(y)}}{D_0} \mathrm{d}y \int_{-\infty}^y e^{-\beta V(z)} \mathrm{d}z\,. \tag{A.17}$$

As $U(z)$ is periodic function, we can simplify the above expression with geometrical expansion, which is

$$\int_{-\infty}^y e^{-\beta V(z)} \mathrm{d}z = \int_{-\infty}^y e^{-\beta (U(z) - fz)} \mathrm{d}z \tag{A.18}$$

$$= \sum_{m=0}^{\infty} \int_{y-1}^y e^{-\beta V(z)} e^{-\beta f m} \mathrm{d}z \tag{A.19}$$

$$= \frac{1}{1 - e^{-\beta f}} \int_{y-1}^y e^{-\beta V(z)} \mathrm{d}z. \tag{A.20}$$

Therefore, T_1 has the form as,

$$T_1 = \frac{1}{1 - e^{-\beta f}} \int_{x_s}^{x_s+1} \mathrm{d}x I(x), \tag{A.21}$$

with

$$I(x) = \frac{e^{\beta V(x)}}{D_0} \int_{x-1}^x \mathrm{d}z e^{-\beta V(z)}\,. \tag{A.22}$$

Accordingly, the nonlinear mobility is,

$$\mu = \frac{\langle \dot{x} \rangle}{f} = \frac{1}{f T_1} = \frac{1 - e^{-\beta f}}{f \int_{x_0}^{x_0+1} \mathrm{d}x I(x)}\,. \tag{A.23}$$

A.2 Numerical simulations

In this thesis, many results are obtained numerically. Here, we present the details of the numerical simulations.

Integration of the stochastic differential equation

Our works are done with the stochastic differential equations. The dynamics for the transport is described by Eq. (3.9). The neuron signaling is studied by the stochastic Hodgkin-Huxley equation with delayed feedback, i.e. Eq. (4.33), and a compartmental stochastic Hodgkin-Huxley equation, i.e. Eq. (4.42), both of which include the stochastic gating variables dynamics equations: Eq. (4.25) and Eq. (4.26). For convenience, we use a general description equation to denote all of them. It has the form as,

$$\dot{x} = f(x) + \sqrt{D}\xi(t)\,. \tag{A.24}$$

Here, D is noise strength, $\xi(t)$ is Gaussian white noise with zero mean and autocorrelation function as,

$$\langle \xi(t)\xi(t')\rangle = 2\delta(t-t'). \tag{A.25}$$

The stochastic differential equation can be numerically integrated by an Euler-type algorithm with the noise generated by the Box-Muller algorithm [133]. Each step of integration has the form as

$$x(t+\Delta t) = x(t) + f(x)\Delta t + g_1\,, \tag{A.26}$$

where g_1 is a Gaussian distributed random number. According to the Box-Muller algorithm, the Gaussian white noise is generated by two uniformly distributed random numbers r_1 and r_2 within the unit interval [0, 1]. Then, the Gaussian distributed number reads,

$$g_1 = \sqrt{-2D\Delta t \log r_1}\cos(2\pi r_2)\,. \tag{A.27}$$

In our simulation, the integration step is $\Delta t = 0.002$. The initial values we picked are zeros.

Note that, the Hodgkin-Huxley gating variables n, m and h are confined to the interval from zero to one. In our simulations, these boundary condition for the gating variables is achieved by skipping each integration step to check whether its value is outside of [0,1]. It is realized by the following method. When the new value of x is generated by Eq. (A.26), we check whether it belongs to the range [0,1]. If not, one has to minus g_1 to go back to the old value. Then, we reproduce Gaussian distributed random number with new random numbers until the gating variables n, m and h within [0,1].

For the transport problem, the mean current $\langle \dot{x}\rangle$ can be obtained, i.e.

$$\langle \dot{x}\rangle = \lim_{t\to\infty}\frac{x(t)-x_0}{t}, \tag{A.28}$$

where, $x(t)$ is the particle position at time t, x_0 is the initial position.

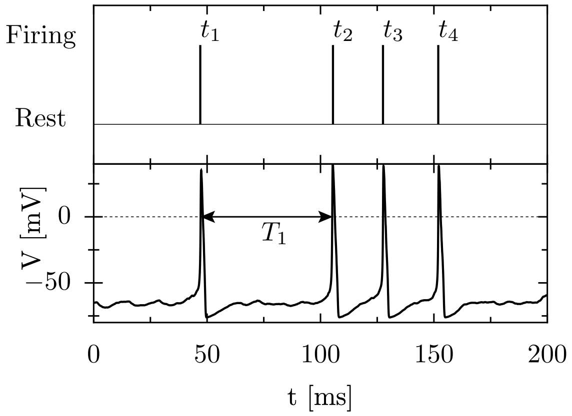

Figure A.2: Spike trains versus time. Downward is a stochastic voltage signal $V(t)$ with a detection barrier $V_0 = 0\,\mathrm{mV}$. Upward is the corresponding point process.

Extraction of the point process

The neuronal encoding is carried by electrical signals, i.e. spikes. The stochastic signal of the membrane potentials can be analyzed by the occurrences of the spikes (action potentials). Therefore, a point process is extracted from each simulated spike train. To achieve this, we firstly define a certain detection barrier to determine the occurrences of spikes. In our simulations, we choose $V_0 = 0\,\mathrm{mV}$ as the threshold value. A spike is detected when the potential $V(t)$ exceeds V_0, c.f. Fig. A.2. In fact, the threshold can change in a wide range with almost no effect on the spike detection. The spike occurrence time t_i is recorded. Therefore, a point process is obtained:

$$u(t) := \sum_{i=1}^{N} \delta(t - t_i)\,, \tag{A.29}$$

where N is the total number of spikes that occur in the elapsed time interval.

One problem has to be addressed. Due to the noise, more than one upward-crossing of the action potentials may occur. To avoid this, a more elaborated decision scheme for the occurrence of spike is applied in our simulations. As there is no spike occurring during the refractory period which has been introduced in the thesis, we define a artificial death time. During this time, there is no spike. It begins at the occurrence time and lasts about 5 ms. We point out that this artificial death time should be smaller than the refractory time.

Based on the point process, the interspike interval histograms (ISIH) and the mean interspike interval $\langle T \rangle$ can be obtained.

Computation of interspike interval histograms (ISIH)

The interspike interval histograms (ISIH) are computed by the following procedures:
(1) Extraction of the point process from the simulated membrane potential.
(2) The interspike interval T_i is obtained from the definition Eq. (4.29).
(3) To calculate the ISIH within time range [0, T], firstly, we divided this range into

N bins of width $\Delta := T/N$. In our simulations, it is fixed at 0.2 ms. Secondly, N_j (with $j = 1, ..., N$) is introduced to count the number of T_i that enters the i'th bin, i.e. the time interval $[(j-1)\Delta \ , \ j\Delta]$. If T_i belongs to the time interval $[(j-1)\Delta \ , \ j\Delta]$, then N_j plus one. As there may be some interspike interval T_i out of the range [0 , T], we also count the total interspike interval numbers $\mathcal{N}$ within this range [0, T]. At last step, we normalized the interspike interval histograms (ISIH) by divided the total interspike interval numbers $\mathcal{N}$.

References

[1] S. A. Arrhenius, *Über die Reaktionsgeschwindigkeit bei der Inversion von Rohrzucker durch Säuren*, Z. Phys. Chem. (Leipzig) **4**, 226–248 (1889).

[2] H. A. Kramers, *Brownian motion in a field of force and the diffusion Model of chemical reactions*, Physica **7**(4), 284–304 (1940).

[3] L. Gammaitoni, P. Hänggi, P. Jung, and F. Marchesoni, *Stochastic resonance*, Rev. Mod. Phys. **70**(1), 223–287 (1998).

[4] L. Callenbach, P. Hänggi, S. J. Linz, J. A. Freund, and L. Schimansky-Geier, *Oscillatory systems driven by noise: Frequency and phase synchronization*, Phys. Rev. E **65**(5), 051110 (2002).

[5] A. Pikovsky, M. Rosenblum, and J. Kurths, *Synchronization: A Universal Concept in Nonlinear Sciences* (Cambridge University Press, Cambridge, 2003).

[6] J. A. Freund, L. Schimansky-Geier, and P. Hänggi, *Frequency and phase synchronization in stochastic systems*, Chaos **13**, 225–238 (2003).

[7] P. A. Tass, *Stimulus-locked transient phase dynamics, synchronization and desynchronization of two oscillators*, EPL **59**(2), 199–205 (2002).

[8] P. Hänggi and F. Marchesoni, *Artificial Brownian motors: Controlling transport on the nanoscale*, Rev. Mod. Phys. **81**(1), 387–442 (2009).

[9] M. Nishiyama, H. Higuchi, and T. Yanagida, *Chemomechanical coupling of the forward and backward steps of single kinesin molecules*, Nat. Cell Biol. **4**, 790–797 (2002).

[10] E. S. Morse, *Fireflies flashing in unison*, Science **4**, 169–170 (1916).

[11] C. Schäfer, M. G. Rosenblum, H.-H. Abel, and J. Kurths, *Synchronization in the human cardiorespiratory system*, Phys. Rev. E **60**(1), 857–870 (1999).

[12] A. Neiman, X. Pei, D. Russell, W. Wojtenek, L. Wilkens, F. Moss, H. A. Braun, M. T. Huber, and K. Voigt, *Synchronization of the noisy electrosensitive cells in the paddlefish*, Phys. Rev. Lett. **82**(3), 660–663 (1999).

[13] A. Longtin, A. Bulsara, and F. Moss, *Time-interval sequences in bistable systems and the noise-induced transmission of information by sensory neurons*, Phys. Rev. Lett. **67**(5), 656–659 (1991).

[14] D. R. Chialvo and A. V. Apkarian, *Modulated noisy biological dynamics: Three examples*, J. Stat. Phys. **70**(1-2), 375–391 (1993).

[15] J. K. Douglass, L. Wilkens, E. Pantazelou, and F. Moss, *Noise enhancement of information transfer in crayfish mechanoreceptors by stochastic resonance*, Nature **365**, 337–340 (1993).

[16] K. Wiesenfeld, D. Pierson, E. Pantazelou, C. Dames, and F. Moss, *Stochastic resonance on a circle*, Phys. Rev. Lett. **72**(14), 2125–2129 (1994).

[17] S. M. Bezrukov and I. Vodyanoy, *Noise-induced enhancement of signal transduction across voltage-dependent ion channels*, Nature **378**, 362–364 (1995).

[18] D. Reguera, G. Schmid, P. S. Burada, J. M. Rubí, R. P., and P. Hänggi, *Entropic transport: Kinetics, scaling, and control mechanisms*, Phys. Rev. Lett. **96**(13), 130603 (2006).

[19] W. D. Volkmuth and R. H. Austin, *DNA electrophoresis in microlithographic arrays*, Nature **358**, 600–602 (1992).

[20] G. I. Nixon and G. W. Slater, *Saturation and entropic trapping of monodisperse polymers in porous media*, J. Chem. Phys. **117**, 4042–4046 (2002).

[21] R. Chang and A. Yethiraj, *Dynamics of chain molecules in disordered materials*, Phys. Rev. Lett. **96**(10), 107802 (2006).

[22] U. Gerland, R. Bundschuh, and T. Hwa, *Translocation of structured polynucleotides through nanopores*, Phys. Bio. **1**, 19–26 (2004).

[23] J. B. Heng, C. Ho, T. Kim, R. Timp, A. Aksimentiev, Y. V. Grinkova, S. Sligar, K. Schulten, and G. Timp, *Sizing DNA using a nanometer-diameter pore*, Biophys. J. **87**, 2905–2911 (2004).

[24] J. B. Heng, A. Aksimentiev, P. M. C. Ho, Y. Grinkova, S. Sligar, K. Schulten, and G. Timp, *The electromechanics of DNA in a synthetic nanopore*, Biophys. J. **90**, 1098–1106 (2006).

[25] J. Lagerqvist, M. Zwolak, and M. D. Ventra, *Fast DNA sequencing via transverse electronic transport*, Nano Lett. **6**(4), 779–782 (2006).

[26] A. Aksimentiev, J. B. Heng, G. Timp, and K. Schulten, *Microscopic kinetics of DNA translocation through synthetic nanopores*, Biophys. J. **87**, 2086–2097 (2004).

[27] H. Lodish, A. Berk, L. Zipursky, P. Matsudaira, D. Baltimore, and J. Darnell, *Molecular cell biology* (W. H. Freeman and company, New York, 1999).

[28] A. L. Hodgkin and A. F. Huxley, *A quantitative description of membrane current and its application to conduction and excitation in nerve*, J. Physiol. (London) **117**, 500–544 (1952).

[29] H. Lecar and R. Nossal, *Theory of threshold fluctuations in nerves I. relationships between electrical noise and fluctuations in axon firing*, Biophys. J. **11**, 1048–1067 (1971).

[30] H. Lecar and R. Nossal, *Theory of threshold fluctuations in nerves II. analysis of various sources of membrane noise*, Biophys. J. **11**, 1068–1084 (1971).

[31] H. V. D. Loos and E. M. Glaser, *Autapses in neocortex cerebri: synapses between a pyramidal cell's axon and its own dendrites*, Brain Res. **48**, 355–360 (1972).

[32] C. Koch, *Biophysics of computation information processing in single neurons* (Oxford University Press, New York, 1999).

[33] B. Hille, *Ion Channels of Excitable Membranes* (Sinauer Associates, Sunderland, 2001).

[34] L. Liu, P. Li, and S. A. Asher, *Entropic trapping of macromolecules by mesoscopic periodic voids in a polymer hydrogel*, Nature **397**, 141–144 (1999).

[35] Z. Siwy, I. D. Kosińska, A. Fuliński, and C. R. Martin, *Asymmetric diffusion through synthetic nanopores*, Phys. Rev. Lett. **94**(4), 048102 (2005).

[36] A. M. Berezhkovskii and S. M. Bezrukov, *Optimizing transport of metabolites through large channels: Molecular sieves with and without binding*, Biophys. J. **88**(3), L17–L19 (2005).

[37] R. M. Barrer, *Zeolites and clay minerals as sorbents and molecular sieves* (Academic Press, illustrated edition edition, London, 1978).

[38] T. Chou and D. Lohse, *Entropy-driven pumping in zeolites and biological channels*, Phys. Rev. Lett. **82**(17), 3552–3555 (1999).

[39] C. Kettner, P. Reimann, P. Hänggi, and F. Müller, *Drift ratchet*, Phys. Rev. E **61**(1), 312–323 (2000).

[40] S. Matthias and F. Müller, *Asymmetric pores in a silicon membrane acting as massively parallel Brownian ratchets*, Nature **424**, 53–57 (2003).

[41] I. D. Kosińska, I. Goychuk, M. Kostur, G. Schmid, and P. Hänggi, *Rectification in synthetic conical nanopores: A one-dimensional Poisson-Nernst-Planck model*, Phys. Rev. E **77**(3), 031131 (2008).

[42] P. S. Burada, P. Hänggi, F. Marchesoni, G. Schmid, and P. Talkner, *Diffusion in confined geometries*, ChemPhysChem **10**, 45–54 (2009).

[43] P. Burada, G. Schmid, Y. Li, and P. Hänggi, *Controlling diffusive transport in confined geometries*, Acta Phys. Pol. B **41**(5), 935–946 (2010).

[44] J. Kärger and D. M. Ruthven, *Diffusion in Zeolites and Other Microporous Solids* (John Wiley and Sons, New York, 1992).

[45] P. Burada, Y. Li, W. Riefler, and G. Schmid, *Entropic transport in energetic potentials*, Chem. Phys. **375**, 514–517 (2010).

[46] H. Risken, *The Fokker-Planck Equation: Methods of Solutions and Applications* (Springer-Verlag, Springer, 1989).

[47] N. V. Kampen, *Stochastic Processes in Physics and Chemistry* (North Holland, 2007).

[48] H. Peter, T. Peter, and B. Michal, *Reaction-rate theory: fifty years after Kramers*, Rev. Mod. Phys. **62**(2), 251–341 (1990).

[49] A. Einstein, *Über die von der molekularkinetischen Theorie der Wärme geforderte Bewegung von in ruhenden Flüssigkeiten suspendierten Teilchen*, Annalen der Physik **17**, 549–560 (1905).

[50] W. Sutherland, *A dynamical theory of diffusion for non-electrolytes and the molecular mass of albumin*, Phil. Mag. **9**, 781–785 (1905).

[51] M. V. Smoluchowski, *Zur kinetischen theorie der brownschen molekularbewegung und der suspensionen*, Ann. Phys. **326**, 757–780 (1906).

[52] P. Langevin, *Sur la théorie du mouvement brownien*, C. R. Acad. Sci. (Paris) **146**, 530–533 (1908).

[53] A. Einstein, *Investigations on the Theory of Brownian Movement* (New York: Dover, 1956).

[54] E. M. Purcell, *Life at low Reynolds number*, Am. J. Phys. **45**(1), 3–11 (1977).

[55] J. D. Cresser, W. H. Louisell, P. Meystre, W. Schleich, and M. O. Scully, *Quantum noise in ring-laser gyros. I. theoretical formulation of problem*, Phys. Rev. A **25**(4), 2214–2225 (1982).

[56] J. D. Cresser, D. Hammonds, W. H. Louisell, P. Meystre, and H. Risken, *Quantum noise in ring-laser gyros. II. numerical results*, Phys. Rev. A **25**(4), 2226–2234 (1982).

[57] R. Stratonovich, *Topics in the theory of random noise*, number v. 2 in Mathematics and its applications (Gordon and Breach, 1967).

[58] A. J. Viterbi, *Principles of coherent communication* (McGraw-Hill, New York, 1966).

[59] V. Ambegaokar and B. I. Halperin, *Voltage due to thermal noise in the dc Josephson effect*, Phys. Rev. Lett. **22**(25), 1364–1366 (1969).

[60] A. Barone and G. Paterno, *Physics and Applications of the Josephson Effect* (Wiley-VCH, 1982).

[61] B. D. Josephson, *Possible new effects in superconductive tunnelling*, Phys. Lett. **1**, 251–253 (1962).

[62] G. Wyllie, *Random motion and Brownian rotation*, Phys. Reps. **61**, 327–376 (1980).

[63] D. Reguera, J. M. Rubí, and A. Pérez-Madrid, *Controlling anomalous stresses in soft field-responsive systems*, Phys. Rev. E **62**(4), 5313–5317 (2000).

[64] J. W. M. Frenken and J. F. v. d. Veen, *Observation of surface melting*, Phys. Rev. Lett. **54**(2), 134–137 (1985).

[65] F. C. Hoppensteadt and E. M. Izhikevich, *Weakly Connected Neural Networks* (Springer, 1997).

[66] P. S. Burada, G. Schmid, P. Talkner, P. Hänggi, D. Reguera, and J. M. Rubb́, *Entropic particle transport in periodic channels*, Biosystems **93**, 16–22 (2008).

[67] G. R. Fleming and P. Hänggi, *Activated Barrier Crossing: Applications in Physics, Chemistry and Biology* (World Scientific, 1994).

[68] P. K. Ghosh, B. C. Bag, and D. S. Ray, *Interference of stochastic resonances: Splitting of Kramers' rate*, Phys. Rev. E **75**(3), 032101 (2007).

[69] C. F. Lee, *Predicting rare events in chemical reactions: Application to skin cell proliferation*, Phys. Rev. E **82**(2), 021103 (2010).

[70] D. Esteve, M. H. Devoret, and J. M. Martinis, *Effect of an arbitrary dissipative circuit on the quantum energy levels and tunneling of a Josephson junction*, Phys. Rev. B **34**(1), 158–163 (1986).

[71] D. Esteve, J. M. Martinis, C. Urbina, E. Turlot, M. H. Devoret, H. Grabert, and S. Linkwitz, *Observation of the temporal decoupling effect on the macroscopic quantum tunneling of a Josephson Junction*, Phys. Scr. **T29**, 121–124 (1989).

[72] T. Christen, *Heterogeneous versus homogeneous nucleation of kink-antikink pairs*, Phys. Rev. E **51**(1), 604–612 (1995).

[73] T. Monnai, A. Sugita, and K. Nakamura, *Role of an intermediate state in homogeneous nucleation*, Phys. Rev. E **74**(6), 061116 (2006).

[74] W. T. Coffey, Y. P. Kalmykov, S. V. Titov, and B. P. Mulligan, *Semiclassical master equation in wigners phase space applied to Brownian motion in a periodic potential*, Phys. Rev. E **75**(4), 041117 (2007).

[75] D. Goulding, S. Melnik, D. Curtin, T. Piwonski, J. Houlihan, J. P. Gleeson, and G. Huyet, *Kramers' law for a bistable system with time-delayed noise*, Phys. Rev. E **76**(3), 031128 (2007).

[76] T. Kampfrath, D. O. Gericke, L. Perfetti, P. Tegeder, M. Wolf, and C. Frischkorn, *Long- and short-lived electrons with anomalously high collision rates in laser-ionized gases*, Phys. Rev. E **76**(6), 066401 (2007).

[77] P. Reimann, G. J. Schmid, and P. Hänggi, *Universal equivalence of mean first-passage time and Kramers rate*, Phys. Rev. E **60**(1), R1–R4 (1999).

[78] M. Khantha and V. Balakrishnan, *First passage time distributions for finite one-dimensional random walks*, Pramana **21**, 111–122 (1983).

[79] P. Reimann, C. Van den Broeck, H. Linke, P. Hänggi, J. M. Rubi, and A. Pérez-Madrid, *Giant acceleration of free diffusion by use of tilted periodic potentials*, Phys. Rev. Lett. **87**(1), 010602 (2001).

[80] P. Reimann, C. Van den Broeck, H. Linke, P. Hänggi, J. M. Rubi, and A. Pérez-Madrid, *Diffusion in tilted periodic potentials: Enhancement, universality, and scaling*, Phys. Rev. E **65**(3), 031104 (2002).

[81] F. Marchesoni, P. Hänggi, and F. Nori, *Brownian motors*, Ann. Phys. (Leipzig) **14**(1-3), 51–70 (2005).

[82] R. D. Astumian and P. Hänggi, *Brownian motors*, Physics Today **55**(11), 33–39 (2002).

[83] P. Reimann and P. Hänggi, *Introduction to the physics of Brownian motors*, Appl. Phys. A-Mater. **75**, 169–178 (2002).

[84] Z. Siwy and A. Fuliński, *Fabrication of a synthetic nanopore ion pump*, Phys. Rev. Lett. **89**(19), 198103 (2002).

[85] U. F. Keyser, J. van der Does, C. Dekker, and N. H. Dekker, *Optical tweezers for force measurements on DNA in nanopores*, Rev. Sci. Instr. **77**(10), 105105 (2006).

[86] U. F. Keyser, B. N. Koeleman, S. van Dorp, D. Krapf, R. M. M. Smeets, S. G. Lemay, N. H. Dekker, and C. Dekker, *Direct force measurements on DNA in a solid-state nanopore*, Nature Phys. **2**, 473–477 (2006).

[87] Y. Rabin and M. Tanaka, *DNA in nanopores: Counterion condensation and coion depletion*, Phys. Rev. Lett. **94**(14), 148103 (2005).

[88] J. Zhang, A. Kamenev, and B. I. Shklovskii, *Conductance of ion channels and nanopores with charged walls: A toy model*, Phys. Rev. Lett. **95**(14), 148101 (2005).

[89] W. Sung and P. J. Park, *Polymer translocation through a pore in a membrane*, Phys. Rev. Lett. **77**(4), 783–786 (1996).

[90] H. Yim, M. S. Kent, D. Y. Sasaki, B. D. Polizzotti, K. L. Kiick, J. Majewski, and S. Satija, *Rearrangement of lipid ordered phases upon protein adsorption due to multiple site binding*, Phys. Rev. Lett. **96**(19), 198101 (2006).

[91] S. Schacht, Q. Huo, I. G. Voigt-Martin, G. D. Stucky, and F. Schüth, *Oil-water interface templating of mesoporous macroscale structures*, Science **273**(5276), 768–771 (1996).

[92] L. Kullman, P. A. Gurnev, M. Winterhalter, and S. M. Bezrukov, *Functional subconformations in protein folding: Evidence from single-channel experiments*, Phys. Rev. Lett. **96**(3), 038101 (2006).

[93] C. M. Spillmann, A. V. Kapur, F. W. Bentrem, J. Naciri, and B. R. Ratna, *Critical field strength in an electroclinic liquid crystal elastomer*, Phys. Rev. Lett. **104**(22), 227802 (2010).

[94] Y. Hatwalne and M. Muthukumar, *Chiral symmetry breaking in crystals of achiral polymers*, Phys. Rev. Lett. **105**(10), 107801 (2010).

[95] J. Han and H. G. Craighead, *Separation of long DNA molecules in a microfabricated entropic trap array*, Science **288**(5468), 1026–1029 (2000).

[96] J. Rousseau, G. Drouin, and G. W. Slater, *Entropic trapping of DNA during gel electrophoresis: Effect of field intensity and gel concentration*, Phys. Rev. Lett. **79**(10), 1945–1948 (1997).

[97] E. B. Kalman, O. Sudre, I. Vlassiouk, and Z. S. Siwy, *Control of ionic transport through gated single conical nanopores*, Anal. Bioanal. Chem. **394**, 413–419 (2009).

[98] J. Kasianowicz, E. Brandin, D. Branton, and D. Deamer, *Characterization of individual polynucleotide molecules using a membranechannel*, Proc. Natl. Acad. Sci. USA **93**, 13770–13773 (1996).

[99] C. Baerlocher, L. B. McCusker, and D. Olson, *Atlas of Zeolite Framework Types* (Elsevier Science, Amsterdam, 2007).

[100] T. A. J. Duke and R. H. Austin, *Microfabricated sieve for the continuous sorting of macromolecules*, Phys. Rev. Lett. **80**(7), 1552–1555 (1998).

[101] J. Kärger, *Single-file diffusion in zeolites*, Mol. Sieves **7**, 329–366 (2008).

[102] J. Fu, J. Yoo, and J. Han, *Molecular sieving in periodic free-energy landscapes created by patterned nanofilter arrays*, Phys. Rev. Lett. **97**(1), 018103 (2006).

[103] M. E. Franke, U. Simon, R. Moos, A. Knezevic, R. Müller, and C. Plog, *Development and working principle of an ammonia gas sensor based on a refined model for solvate supported proton transport in zeolites*, Phys. Chem. Chem. Phys. **5**, 5195–5198 (2003).

[104] M. Boronat, P. Concepción, A. Corma, M. T. Navarro, M. Renz, and S. Valencia, *Reactivity in the confined spaces of zeolites: the interplay between spectroscopy and theory to develop structure-activity relationships for catalysis*, Phys. Chem. Chem. Phys. **11**, 2876–2884 (2009).

[105] C. C. Freyhardt, M. Tsapatsis, R. F. Lobo, K. J. Balkus, and M. E. Davis, *A high-silica zeolite with a 14-tetrahedral-atom pore opening*, Nature **381**, 295–298 (1996).

[106] M. H. Jacobs, *Diffusion processes* (Springer-Verlag, New York, 1967).

[107] A. Fick, *Über diffusion*, A. Poggendorff's Ann. **94**, 59–86 (1855).

[108] D. Reguera and J. M. Rubí, *Kinetic equations for diffusion in the presence of entropic barriers*, Phys. Rev. E **64**(6), 061106 (2001).

[109] P. S. Burada, G. Schmid, D. Reguera, J. M. Rubí, and P. Hänggi, *Biased diffusion in confined media: Test of the Fick-Jacobs approximation and validity criteria*, Phys. Rev. E **75**(5), 051111 (2007).

[110] P. Kalinay and J. K. Percus, *Corrections to the Fick-Jacobs equation*, Phys. Rev. E **74**(4), 041203 (2006).

[111] P. Kalinay, *Mapping of forced diffusion in quasi-one-dimensional systems*, Phys. Rev. E **80**(3), 031106 (2009).

[112] S. Lifson and J. L. Jackson, *On the self-diffusion of Ions in a polyelectrolyte solution*, J. Chem. Phys. **36**, 2410–2414 (1962).

[113] P. Hänggi and H. Thomas, *Stochastic Processes: Time-Evolution, Symmetries and Linear Response*, Phys. Rep. **88**, 207–319 (1982).

[114] Y. Liu and B.-Q. Ai, *Diffusion in a tilted periodic potential with entropic barriers*, J. Phys. Cond. Mat. **21**(46), 465102 (2009).

[115] Y. Li, G. Schmid, P. Hänggi, and L. Schimansky-Geier, *Spontaneous spiking in an autaptic Hodgkin-Huxley setup*, Phys. Rev. E **82**(6), 061907 (2010).

[116] Y. Li, G. Schmid, and P. Hänggi, *Noisy saltatory spike propagation: The breakdown of signal transmission due to channel noise*, Eur. Phys. J. Special Topics **187**, 171–177 (2010).

[117] D. Johnston and S. M. Wu, *Foundations of Cellular Neurophysiology* (The MIT Press, Cambridge, 1994).

[118] D. E. Goldman, *Potential, impedance, and rectification in membranes*, J. Gen. Physiol. **27**(1), 37–60 (1943).

[119] A. L. Hodgkin and B. Katz, *The effect of sodium ions on the electrical activity of the giant axon of the squid*, J. Physiol. **108**(1), 37–77 (1949).

[120] J. Keener and J. Sneyd, *Mathematical Physiology* (Springer, 1998).

[121] C. Koch, *Biophysics of Computation: Information Processing in Single Neurons* (Oxford University Press, USA, 1998).

[122] R. MacKinnon, S. L. Cohen, A. Kuo, A. Lee, and B. T. Chait, *Structural conservation in prokaryotic and eukaryotic potassium channels*, Science **280**, 106–109 (1998).

[123] D. A. Doyle, J. M. Cabral, R. A. Pfuetzner, A. Kuo, J. M. Gulbis, S. L. Cohen, B. T. Chait, and R. MacKinnon, *The structure of the potassium channel: Molecular basis of* K^+ *conduction and selectivity*, Science **280**, 69–77 (1998).

[124] J. Borg, *Refractory period of single motor nerve fibres in man*, J. Neurol. Neurosurg. Psychiatry. **47**, 344–348 (1984).

[125] D. Hansel, G. Mato, and C. Meunier, *Phase dynamics for weakly coupled Hodgkin-Huxley neurons*, EPL **23**(5), 367–372 (1993).

[126] C. Meunier and I. Segev, *Playing the Devil's advocate: is the Hodgkin-Huxley model useful?*, Trends Neurosci. **25**, 558–563 (2002).

[127] E. Neher and B. Sakmann, *Single-channel currents recorded from membrane of denervated frog muscle fibres*, Nature (London) **260**, 779–802 (1976).

[128] B. Sakmann and E. N. (editors), *Single-Channel Recording* (Springer, New York, 1995), 2nd edition.

[129] L. L. S. and T. A. T., *Using fractals and nonlinear dynamics to determine the physical properties of ion channel proteins*, Crit. Rev. Neurosci. **10**, 169–187 (1996).

[130] J. A. White, J. T. Rubinstein, and A. R. Kay, *Channel noise in neurons*, Trends Neurosci. **23**, 131–137 (2000).

[131] R. F. Fox and Y.-N. Lu, *Emergent collective behavior in large numbers of globally coupled independently stochastic ion channels*, Phys. Rev. E **49**(4), 3421–3431 (1994).

[132] H. C. Tuckwell, *Diffusion approximations to channel noise*, J. Theoret. Biology **127**, 427–438 (1987).

[133] G. E. P. Box and M. E. Muller, *A note on the generation of random normal deviates*, Ann. Math. Stat. **29**(2), 610–611 (1958).

[134] G. Schmid, I. Goychuk, and P. Hänggi, *Stochastic resonance as a collective property of ion channel assemblies*, EPL **56**, 22–28 (2001).

[135] C. C. Chow and J. White, *Spontaneous action potentials due to channel fluctuations*, Biophys. J. **71**, 3013–3021 (1996).

[136] T. Schwalger and L. Schimansky-Geier, *Interspike interval statistics of a leaky integrate-and-fire neuron driven by Gaussian noise with large correlation times*, Phys. Rev. E **77**(3), 031914 (2008).

[137] T. Verechtchaguina, L. Schimansky-Geier, and I. M. Sokolov, *Spectra and waiting-time densities in firing resonant and nonresonant neurons*, Phys. Rev. E **70**(3), 031916 (2004).

[138] G. M. Süel, J. García-Ojalvo, L. M. Liberman, and M. B. Elowitz, *An excitable gene regulatory circuit induces transient cellular differentiation*, Nature **440**, 545–550 (2006).

[139] J. L. Cabrera and J. G. Milton, *On-Off intermittency in a human balancing task*, Phys. Rev. Lett. **89**(15), 158702 (2002).

[140] J. Hizanidis and E. Schöll, *Control of coherence resonance in semiconductor superlattices*, Phys. Rev. E **78**(6), 066205 (2008).

[141] T. Erneux and J. Grasman, *Limit-cycle oscillators subject to a delayed feedback*, Phys. Rev. E **78**(2), 026209 (2008).

[142] W. Bao, Z. Li, L.-Q. Zhou, and Z. Gao, *Robust entrainment phenomena of oscillations by delay time in the photosensitive Oregonator model*, Phys. Rev. E **79**(1), 016214 (2009).

[143] C. Beta, M. Bertram, A. S. Mikhailov, H. H. Rotermund, and G. Ertl, *Controlling turbulence in a surface chemical reaction by time-delay autosynchronization*, Phys. Rev. E **67**(4), 046224 (2003).

[144] T. Prager, H.-P. Lerch, L. Schimansky-Geier, and E. Schöll, *Increase of coherence in excitable systems by delayed feedback*, J. Phys. A: Math. Theor. **40**(36), 11045–11055 (2007).

[145] G. C. Sethia, J. Kurths, and A. Sen, *Coherence resonance in an excitable system with time delay*, Phys. Lett. A **364**(3-4), 227–230 (2007).

[146] A. B. Karabelas and D. P. Purrura, *Evidence for autapses in the substantia nigra*, Brain Res. **200**, 467–473 (1980).

[147] G. Tamás, E. H. Buhl, and P. Somogyi, *Massive Autaptic self-innervation of GABAergic neurons in cat visual cortex*, J. Neurosci. **17**, 6352–6364 (1997).

[148] J. M. Bekkers, *Neurophysiology: Are autapses prodigal synapses?*, Curr. Biol. **8**, R52–R55 (1998).

[149] K. Ikeda and J. M. Bekkers, *Autapses*, Curr. Biol. **16**, R308–R308 (2006).

[150] R. Preston, G. Bishop, and S. Kitai, *Medium spiny neuron projection from the rat striatum: An intracellular horseradish peroxidase study*, Brain Res. **183**, 253–263 (1980).

[151] D. P. Kuffler, J. Nicholls, and P. Drapeau, *Transmitter localization and vesicle turnover at a serotoninergic synapse between identified leech neurons in culture*, J. Comp. Neurol. **256**, 516–526 (1987).

[152] W. Shi and S. Rayport, *GABA synapses formed in vitro by local axon collaterals of nucleus accumbens neurons*, J. Neurosci. **14**, 4548–4560 (1994).

[153] J. Lübke, H. Markram, M. Frotscher, and B. Sakmann, *Frequency and dendritic distribution of Autapses established by layer 5 Pyramidal neurons in the developing rat neocortex: Comparison with synaptic innervation of adjacent neurons of the same class*, J. Neurosci. **16**, 3209–3218 (1996).

[154] C. Masoller, M. C. Torrent, and J. García-Ojalvo, *Interplay of subthreshold activity, time-delayed feedback, and noise on neuronal firing patterns*, Phys. Rev. E **78**(4), 041907 (2008).

[155] K. Pyragas, *Continuous control of chaos by self-controlling feedback*, Phys. Lett. A **170**, 421–428 (1992).

[156] G. Schmid, I. Goychuk, and P. Hänggi, *Channel noise and synchronization in excitable membranes*, Physica A **325**, 165–175 (2003).

[157] B. Lindner, J. García-Ojalvo, A. Neiman, and L. Schimansky-Geier, *Effects of noise in excitable systems*, Phys. Rep. **392**, 321–424 (2004).

[158] A. M. Lacasta, F. Sagués, and J. M. Sancho, *Coherence and anticoherence resonance tuned by noise*, Phys. Rev. E **66**(4), 045105 (2002).

[159] C. Zhou and J. Kurths, *Noise-induced synchronization and coherence resonance of a Hodgkin-Huxley model of thermally sensitive neurons*, Chaos **13**, 401–409 (2003).

[160] H. S. Seung, D. D. Lee, B. Y. Reis, and D. W. Tank, *The Autapse: A simple illustration of short-term analog memory storage by tuned synaptic feedback*, J. Comput. Neurosci. **9**(2), 171–185 (2000).

[161] P. Hänggi and P. Riseborough, *Dynamics of nonlinear dissipative oscillators*, Am. J. Phys. **51**, 347–352 (1983).

[162] N. B. Janson, A. G. Balanov, and E. Schöll, *Delayed feedback as a means of control of noise-induced motion*, Phys. Rev. Lett. **93**(1), 010601 (2004).

[163] A. Pototsky and N. Janson, *Correlation theory of delayed feedback in stochastic systems below Andronov-Hopf bifurcation*, Phys. Rev. E **76**(5), 056208 (2007).

[164] Y. Kuramoto, *Chemical Oscillations, Waves, and Turbulence* (Springer-Verlag, Berlin, 1984).

[165] J. A. Acebrón, L. L. Bonilla, C. J. Pérez Vicente, F. Ritort, and R. Spigler, *The Kuramoto model: A simple paradigm for synchronization phenomena*, Rev. Mod. Phys. **77**(1), 137–185 (2005).

[166] H. G. Schuster and P. Wagner, *A model for neuronal oscillations in the visual cortex*, Biol. Cybern. **64**, 77–82 (1990).

[167] E. Niebur, H. G. Schuster, and D. M. Kammen, *Collective frequencies and metastability in networks of limit-cycle oscillators with time delay*, Phys. Rev. Lett. **67**(20), 2753–2756 (1991).

[168] L. G. Morelli, S. Ares, L. Herrgen, C. Schröter, F. Jülicher, and A. C. Oates, *Delayed coupling theory of vertebrate segmentation*, HFSP Journal **3**, 55–66 (2009).

[169] H. Schuster and P. Wagner, *A model for neuronal oscillations in the visual cortex*, Biol. Cybern. **64**, 83–85 (1990).

[170] W. Gerstner, *Rapid phase locking in systems of pulse-coupled oscillators with delays*, Phys. Rev. Lett. **76**(10), 1755–1758 (1996).

[171] H. U. Voss, *Anticipating chaotic synchronization*, Phys. Rev. E **61**(5), 5115–5119 (2000).

[172] B. B. Averbeck and D. Lee, *Coding and transmission of information by neural ensembles*, Trends Neurosci. **27**, 225–230 (2004).

[173] A. F. Huxley and R. Stämpeli, *Evidence for saltatory conduction in peripheral myelinated nerve fibres*, J. Physiol. **108**(3), 315–339 (1949).

[174] J. Hodler, R. Stämpfli, and I. Tasaki, *Role of potential wave spreading along myelinated nerve fiber in excitation and conduction*, Am. J. Physiol. **170**(2), 375–389 (1952).

[175] A. Ochab-Marcinek, G. Schmid, I. Goychuk, and P. Hänggi, *Noise-assisted spike propagation in myelinated neurons*, Phys. Rev. E **79**(1), 011904 (2009).

[176] K. Aihara, G. Matsumoto, and Y. Ikegaya, *Periodic and non-periodic responses of a periodically forced Hodgkin-Huxley oscillator*, J. Theor. Biol. **109**, 249–269 (1984).

[177] P. Hänggi, *Stochastic resonance in biology*, ChemPhysChem **3**, 285–290 (2002).

[178] P. Jung and J. W. Shuai, *Optimal sizes of ion channel clusters*, EPL **56**, 29–35 (2001).

[179] D. Pedone, M. Langecker, G. Abstreiter, and U. Rant, *A porecavitypore device to trap and investigate single nanoparticles and DNA molecules in a femtoliter compartment: Confined diffusion and narrow escape*, Nano Lett. **11**(4), 1561–1567 (2011).

[180] S. Zeng, Y. Tang, and P. Jung, *Spiking synchronization of ion channel clusters on an axon*, Phys. Rev. E **76**(1), 011905 (2007).

[181] G. H. Weiss, *First passage time problems in chemical physics*, Adv. Chem. Phys. **13**, 1–18 (1967).

Acknowledgement

First and foremost, I would like to thank Prof. Dr. Peter Hänggi for giving me this opportunity to work in his group and financial support. Thanks a lot for introducing me into the field of biophysics. I benefited a lot from his encouragement and support.

It is a great pleasure for me to thank Dr. Gerhard Schmid for being patient discussion with me. During last three years, Gerhard was always willing to teach and offer advice to lots of my problems. Thanks for dedicated support, guidance, discussions and encouragement all the times during my PhD study.

I would like to thank Prof. Dr. Lutz Schimansky-Geier from Humboldt University for his guidance and discussion. I also thank Dr. Sergey Savel'ev from Loughborough University for the collaboration.

I thank Dr. Eric Lutz for being my second referee of my thesis. I am also so grateful to Prof. Dr. Achim Wixforth and PD. Dr. Peter Schwab for joining the examination board.

I gratefully acknowledge financial support by Nanosystems Initiative Munich (NIM) and the China Scholarship Council (CSC).

I would like to express my appreciation to Dr. Nianbei Li for his suggestions and useful discussion. I wish to thank the members in groups of theoretical physics I and II, Prof. Dr. Peter Talkner, PD. Dr. Igor Goychuk, Dr. Michele Campisi, Dr. Alexey Ponomarev, Dr. Georg Reuther, Dr. Andreas Sinner, Dr. Sebastian Deffner, Stefanie Hilt, Fei Zhan and Armin Seibert for all the assistance and advice. You brought me lots of fun in my workdays. I will really miss our lunchtime intellectual discussions and the beer session. I want to thank our secretary Ms. Eva Seehuber for her kind helps.

I also would like to thank the former members in groups of theoretical physics I and II, especially Dr. Sekhar Burada, Dr. David Zueco, Dr. Franz J. Kaiser.

I owe special thanks to my family and friends for their support and understanding.

Curriculum Vitae

Personal Data

Name: Yunyun Li

Date of birth: 10 September 1983

Nationality: China

Parents: Mingfu Li and Zhiju Luo

Education

Sep. 2001- Jul. 2005: Bachelor degree in science
Beijing Normal University, Physics department

Sep. 2005- Jul. 2008: Master degree in science
Beijing Normal University, Physics department

Sep. 2008- Present: PhD student
Augsburg University, Physics department